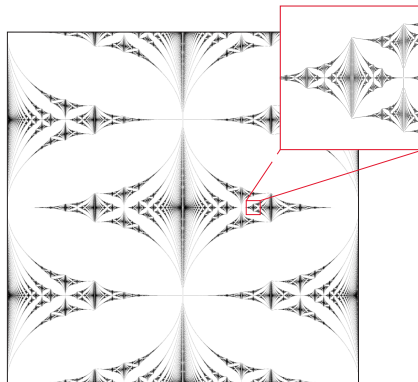# Magnetic Quantum Walks of Neutral Atoms in Optical Lattices

Dissertation
zur
Erlangung des Doktorgrades (Dr. rer. nat.)
der
Mathematisch-Naturwissenschaftlichen Fakultät
der
Rheinischen Friedrich-Wilhelms-Universität Bonn

von
Muhammad Sajid
aus
Charsadda, Pakistan

Bonn, 29.08.2018

Dedicated to my parents,
for their unconditional love and support.

Abstract

This thesis focuses on the simulation of the physics of a charged particle under an external magnetic field by using discrete-time quantum walks of a spin-1/2 particle in a two-dimensional lattice. By Floquet-engineering the quantum-walk protocol, an Aharonov–Bohm geometric phase is imprinted onto closed-loop paths in the lattice, thus realizing an abelian gauge field —the analog of a magnetic flux threading a two-dimensional electron gas. I show that in the strong-field regime, i.e. when the flux per plaquette of the lattice is a sizable fraction of the flux quantum, *magnetic quantum walks* give rise to nearly flat energy bands. I demonstrate that the system behaves like a Chern insulator by computing the Chern numbers of the energy bands and studying the excitation of the midgap topologically protected edge modes. These modes are extended all along the boundaries of the magnetic domains and remain robust against perturbations that respect the gap closing conditions.

Furthermore, I discuss a possible experimental implementation of this scheme using neutral atoms trapped in two dimensional spin-dependent optical lattices. The proposed scheme has a number of unique features, e.g. it allows one to generate arbitrary magnetic-field landscapes, including those with sharp boundaries along which topologically protected edge states can be localized and probed.

Additionally, I introduce the scattering matrix approach in discrete-time quantum walks to probe the Hofstadter spectrum and compute its topological invariants. By opening up a discrete-time quantum walk system and connecting it to metallic leads, I demonstrate that the reflection/transmission probabilities of a particle from the scattering region give information on the energy spectrum and topological invariants of the system. Although the work presented here focuses on the physics of a single particle in a clean system, it sets the stage for studies of many-body topological states in the presence of interactions and disorder.

Parts of this thesis will be published in the following article:

[1] M. Sajid, J. K. Asbóth, P. Arnault, D. Meschede, R. Werner, A. Alberti,
   Realizing Floquet Chern insulators with discrete-time quantum walks, (2018), in preparation

Contents

Introduction

A two-dimensional (2D) system of electrons subjected to a strong perpendicular magnetic field manifests the integer quantum Hall effect (IQHE) [2, 3]: a universal phenomenon where the quantization of the Hall conductance is independent of geometric effects, the host material, and the concentration of impurities. Due its universality, the quantization has a very high precision, typically $\sim 10^{-9}$, which is, nowadays, used as the resistance standard [4]. Quantum Hall systems are the first physical systems where a topological phenomenon was observed. A quantum Hall state, for example, is characterized by a *non-local* integer physical invariant (giving the quantized value of the Hall conductance) and the number of extended current-carrying edge states, known as *topologically-protected* (TP) edge states [5]. These properties remain robust against gentle perturbations and can change only when the system undergoes a quantum phase transition [6, 7].

A lattice version of the quantum Hall system features much richer physics even at a single-particle level. This is sometimes known as a Chern insulator, which behaves as an ordinary band insulator in the bulk, yet exhibits exotic chiral transport in the proximity of its boundaries. Along these edges, particles can propagate unidirectionally without suffering from backscattering nor dissipation into the bulk. Such a robust transport behavior has its origin in TP edge modes, which extend along the length of the insulator. The existence of such states is guaranteed by the non-trivial topological structure of the bulk states forming topological bands. This connection between TP edge modes and the topological structure of the bulk states is the essence of the *bulk–boundary correspondence* [8]. In a 2D band insulator, an energy band with a topologically non-trivial structure is characterized by a non-vanishing Chern number —an invariant that counts the number of topological obstructions to defining a global gauge for the Bloch states constituting the band [9]. Quantum Hall systems, in this class, are thus the first Chern insulators, where the Chern numbers of the bulk bands determine the quantization integer of the Hall conductance. However, as shown by Haldane in his seminal work [10], the robust chiral transport is neither specific to homogeneous magnetic fields nor to the properties of the underlying Landau levels, provided that the time-reversal symmetry is broken. This insight has triggered the quest for topological materials that forego the strong magnetic field of quantum Hall systems, and yet can conduct charges without dissipation. The first demonstrations of this concept have been shown in condensed matter systems [11] and with ultracold atoms trapped in optical lattices [12–14] in the regime of weakly or non-interacting particles.

Tight binding lattices offer an attractive setting to realize Chern insulators, as the strong confinement provided by the lattice can be exploited to enhance particle-particle interactions. This allows for the realization of interaction-induced topological phases such as fractional quantum Hall states for partially filled Chern bands [15–17]. Protected by a large energy gap, these states are expected to survive at high

temperatures and even at room temperature in electronic solid-state systems [18]. Nearly flat bands with non-vanishing Chern numbers and large gap separations have been identified as favorable conditions to realize these strongly correlated states, since in these circumstances interactions among particles are the dominating physical mechanism [19–21]. One promising route to realize topological flat bands while preserving the underlying structure of the lattice is through tight-binding lattices pierced by a strong magnetic field, i.e. when the flux Φ of the magnetic field threaded through a single plaquette of the 2D lattice is a sizable fraction of the flux quantum $\Phi_0 = h/Q$ (Q is the electric charge, h is the Planck constant) [22, 23]. In this regime of strong field, the lattice constant (a) and the magnetic length scale ($\ell_B = a\sqrt{\Phi_0/(2\pi\Phi)}$) become comparable with each other, and the regular structure of the highly degenerate Landau levels (which describe the single-particle states in the limit of weak fields) transforms into a fractal-like spectrum of energy bands —the so-called Hofstadter butterfly [24]. For commensurate values of the flux ratio $\phi = \Phi/\Phi_0$, these energy bands are nearly flat and characterized by non-vanishing Chern numbers C, which, in general, are not restricted to $|C| = 1$ as is the case with Landau levels. Such topological flat bands are expected to give rise to a topological gapped many-body state [22, 23], much the same as an incompressible quantum liquid appears in the weak field (long wavelength) limit of the Hofstadter Hamiltonian for partially filled Landau levels [25]. The leading candidates to realize a fractional Chern insulator are ultracold-atom systems, for they provide the required level of controllability to implement flat-band models [26, 27]; however, no experimental realization has been reported yet.

The study of such interesting physics with conventional solids requires extraordinarily strong magnetic field, typically of the order 10^5 T. This condition is out of reach for existing experimental setups, where fields are of the order of 10 T. More favorable conditions are achieved by tailoring synthetic superlattices with considerably larger lattice constants [28] and moiré superlattices made of graphene on top of a semiconductor substrate [29]. To avoid dealing with such high fields, a number of proposals have been put forward [30–32] aiming at recreating the effect of magnetic fields synthetically through the engineering Aharonov–Bohm geometric phases. In the case of neutral atoms trapped in optical lattices, the standard approach to create such a synthetic gauge fields relies on photon-assisted tunneling, which can be realized either using an additional dressing field [33–35] or by shaking the lattice itself [36–38]. Based on these approaches, strong synthetic magnetic fields in 2D optical lattices have been demonstrated [12, 13, 39, 40]. However, because the kinetic energy in a shallow lattice is of the order of $\hbar^2/(ma^2)$ (m is the atomic mass), ultracold-atom experiments in optical lattices must be conducted at very low energy scales, corresponding to few nK, which are generally difficult to reach. In addition, low energies signify small hopping terms ($< h \times 1$ kHz) and, correspondingly, long evolution times, during which heating and other decoherence mechanisms can be very detrimental to the coherent evolution of the system [39–42]. Increasing the kinetic energy by using light atomic species (e.g., lithium) and, possibly, subwavelength lattice constants [43, 44] has been identified as one way to curb the challenge of experimental realizations.

The work in this thesis maps out a different route to explore the physics in the strong-field regime. I make use of the quantum-walk protocol to simulate the effects of a strong abelian gauge field, and then implement scattering matrix formalism to probe its spectrum. I will start with an introduction to my work in Chapter 2 and Chapter 3. In Chapter 2, I will shortly report on the 2D tight binding model for a single spin-polarized electron in the presence of an external magnetic field. This model is an effective tool for describing the dynamics of tightly bound electrons in solids. The dynamics of the system is described by the famous single-particle Haper's Hamiltonian [45]. I will present the topological properties of the magnetic Bloch bands of the Harper's Hamiltonian by computing the bulk topological invariants, i.e. the Chern numbers, edge spectrum in the presence of a boundary, and the bulk–boundary correspondence principle.

In Chapter 3, I will introduce discrete-time quantum walks (QWs) for a spin-1/2 particle in 1D and 2D, and their topological properties. The evolution of a QW at integer time steps can be described by a

time-independent effective Hamiltonian (associated with the walk protocol). This effective Hamiltonian, like a real static lattice Hamiltonian, can have interesting non-trivial topological properties. In 1D, the existence of a non-trivial topological phase is conditioned with the existence of certain symmetries. Three important discrete symmetries will be introduced, and topological properties, i.e. bulk topological invariants and edges states in the presence of a boundary, will be demonstrated both for 1D and 2D QWs. Being *periodically driven quantum systems*, QWs manifest even rich topological features (with a new set of topological invariants) than those given by their effective Hamiltonians. To capture the complete topological structure of a walk, information beyond that contained in the effective Hamiltonian is required. This will be demonstrated along with the topological features specific to periodically driven quantum systems (QWs).

The main results of my work will be presented in Chapter 4 and Chapter 5. In Chapter 4, I will present the extension of a simple 2D Hadamard-like QW of a spin-1/2 particle to simulate the effect of artificial magnetic fields. This is accomplished by Floquet-engineering the walk protocol, which imprints an Aharonov–Bohm geometric phase on the closed-loop paths in the lattice, thus realizing an abelian gauge field. This is an analog of a magnetic flux threading a 2D electron gas. In the regime of a strong magnetic field, i.e. $\Phi \sim \Phi_0$, the energy bands of magnetic QWs are nearly flat and have large Chern numbers. A possible experimental implementation of this scheme will be presented, which is based on neutral atoms trapped in 2D spin-dependent optical lattices. The proposed scheme has a number of unique advantages, e.g. it allows one to generate arbitrary magnetic-field landscapes (including those with sharp boundaries). I will demonstrate (with my numerical results) the robust atom transport along boundaries separating regions of different field strength revealing the topological character of the Chern bands.

In Chapter 5, I will report on the scattering matrix approach in QWs to probe the Hofstadter spectrum and to compute its topological invariants. The scattering matrix formalism is one of the central tools for describing transport phenomena in mesoscopic devices. I will introduce a similar approach in QWs and will demonstrate that the reflection/transmission probabilities of a particle from the scattering region give information on the energy spectrum and topological invariants of the walk.

The schemes presented in this thesis provide a platform to investigate many-body topological states in the presence of interactions and disorder [19–21].

Magnetic Fields on the Square Lattice

I N the continuum, a 2D system of electrons subjected to a strong perpendicular magnetic field manifests the universal phenomenon of IQHE [2, 3]. A striking feature of such system is the manifestation of topological phenomena; this system exhibits localized states in the bulk, forming a band insulator that exhibits extended states carrying quantized current at the sample boundary. The lattice version of this problem exhibits rich physics even at a single-particle level. In the regime of strong magnetic fields, the competition between the two length scales in the system (lattice constant and magnetic length scale) leads to a fractal-like spectrum of energy bands, known as Hofstadter spectrum [24, 46]. This is in contrast to the regular structure of the highly degenerate Landau levels, which describe the single-particle states in the limit of weak fields. For commensurate values of the flux ratio ϕ, the energy bands are nearly flat with non-trivial topology, i.e. they are characterized by non-vanishing Chern numbers C, which, in general, are not restricted to $|C| = 1$. The exploration of this physics with conventional materials requires an extraordinarily strong magnetic field, which is beyond the reach of current experimental setups. To explore this physics, synthetic superlattices with considerably larger lattice constants [28] and moiré superlattices [29] can be used to relax the magnetic field requirements by several orders of magnitudes. As an alternative route, the effects of a strong magnetic field can be recreated synthetically in systems of neutral atoms trapped in tight-binding optical lattices, thus allowing for the exploration of the strong field regime [12, 13, 39, 40].

In this chapter, I introduce the physics of a spin-polarized charged particle in the presence of a strong magnetic field using a 2D tight-binding model. The main goal is to present the energy spectrum and the corresponding topological properties of the time-independent Hamiltonian underlying this problem. I start with a simple 2D tight-binding model and introduce the effects of an external magnetic field. A 2D tight-binding system has discrete translation symmetry given by lattice translation operators. The corresponding energy spectrum consists of discrete Bloch bands, which are topologically trivial (section 2.1). The presence of an external magnetic field breaks the original translation symmetry of the problem and can be restored by defining the so called *magnetic translation operators*. The new symmetry of the problem has an enlarged unit cell (known as a *magnetic unit cell*), the area of which depends on the strength of the flux ratio ϕ. The magnetic translation operators translate a particle in the lattice and imprints the so called *Peierls phases*, which, when integrated around a unit cell of the lattice, are analogous to the Aharonov–Bohm phases (section 2.1.1) [47]. I demonstrate with examples that for rational values of ϕ, the lowest Bloch band splits into a number of subbands, which are sometimes known as "magnetic Bloch bands" (section 2.2) [24]. These are relatively flat, separated by large gaps, and have non-trivial topology. I show the non-trivial topological character of these bands by computing their Chern numbers, which are usually $|C| \geq 1$. The Chern numbers determine the quantization integer

of the Hall conductance (section 2.3.2). I then demonstrate that the system exhibits TP edge states in presence of a boundary. These are extended along the whole length of the boundary and carry quantized current. The number of TP edge states is related to the Chern numbers of the bands via the bulk–boundary correspondence principle, which I demonstrate with examples (section 2.3.3) [8].

2.1 Tight Binding Model on a 2D Squared Lattice

Tight binding models are effective tools for describing the properties of electrons that are tightly bounded to their parent atoms in solids and has limited interactions with other atoms in its surrounding. The wavefunction of an electron is assumed to be similar to that of the standard orbitals of its parent atom and its overlap with the wavefunctions of other atoms is small. For a single tightly-bound electron with negligible on-site interactions, the single-particle Hamiltonian consists only of nearest-neighbor hopping terms. From the 2D lattice perspective, a particle remains localized on a single site of the lattice and hops in the lattice via tunneling from one site to another.

Let us consider a single-band tight-binding model on an infinitely extended 2D square lattice for a spin-polarized particle. Throughout the chapter, coordinates on the discrete lattice are labelled by $\boldsymbol{x} = (j, l) \in \mathbb{Z}^2$ with basis states $|j, l\rangle$ and the lattice constant in both x and y direction is equal to 1. For simplicity, we assume that the particle can tunnel only to its nearest neighbor lattice sites with tunneling amplitude $\mathcal{J}$ in both directions. The tight binding Hamiltonian in terms of the lattice translation operators (or simply "shift operators") $\hat{\mathcal{S}}_x^0$ and $\hat{\mathcal{S}}_y^0$ can be written as

$$\hat{H}_{\mathrm{TB}} = -\mathcal{J}(\hat{\mathcal{S}}_x^0 + \hat{\mathcal{S}}_y^0 + \text{h.c.}). \tag{2.1}$$

The shift operator $\hat{\mathcal{S}}_x^0$ shifts a particle by one lattice site along the positive x direction and $\hat{\mathcal{S}}_y^0$ by one lattice site in the positive y direction. The term denoted by h.c. is the Hermitian conjugate of the first two terms. The shift operators can also be written in terms of creation (annihilation) operator $\hat{c}_{j,l}^\dagger$ ($\hat{c}_{j,l}$), creating (annihilating) a particle on a lattice site with coordinates (j, l), in the following way:

$$\hat{\mathcal{S}}_x^0 = \sum_{j,l} \hat{c}_{j+1,l}^\dagger \hat{c}_{j,l}\,, \qquad \hat{\mathcal{S}}_y^0 = \sum_{j,l} \hat{c}_{j,l+1}^\dagger \hat{c}_{j,l}. \tag{2.2}$$

The second quantized representation of the Hamiltonian eq. (2.1) is,

$$\hat{H}_{\mathrm{TB}} = -\mathcal{J} \sum_{j,l} (\hat{c}_{j+1,l}^\dagger \hat{c}_{j,l} + \hat{c}_{j,l+1}^\dagger \hat{c}_{j,l} + \text{h.c.}). \tag{2.3}$$

In the absence of a magnetic field, the system has translational symmetry, i.e. translation by an arbitrary lattice vector is an allowed symmetry operation, and it is favorable for the theoretical understanding of the problem to make use of this symmetry. The generator of the lattice translation is known as lattice momentum or quasi momentum[1] $k = (k_x, k_y)$ and due to the discreteness of the lattice translations, only values inside the first Brillouin zone (BZ), i.e. $k \in [-\pi, \pi[^2$, are physical. Both lattice translation operators commute with the Hamiltonian (eq. (2.3)), i.e. $[\hat{\mathcal{S}}_x^0, \hat{H}_{\mathrm{TB}}] = [\hat{\mathcal{S}}_y^0, \hat{H}_{\mathrm{TB}}] = 0$, and also with each other, i.e. $[\hat{\mathcal{S}}_x^0, \hat{\mathcal{S}}_y^0] = 0$. These three operators form a set of good quantum numbers for the considered system, i.e. we can find common eigenstates for all these operators which in this case are Bloch functions. In

---

[1] Since the system has discrete spatial translational invariance, we speak of "quasimomentum" instead of "momentum".

quasimomentum representation, the Hamiltonian (eq. (2.3)) takes the form,

$$\hat{H}_{\text{TB}}(k_x, k_y) = -2\mathcal{J} \int_{BZ} dk (\cos(k_x) + \cos(k_y)) \hat{c}_k^\dagger \hat{c}_k. \tag{2.4}$$

Here the following transformation is used,

$$\hat{c}_{j,l} = \frac{1}{(2\pi)^2} \int_{BZ} dk_x dk_y \hat{c}_k e^{ik_x j} e^{ik_y l}, \tag{2.5}$$

with the inverse transformation

$$\hat{c}_k = \sum_{j,l} \hat{c}_{j,l} e^{-ik_x j} e^{-ik_y l}. \tag{2.6}$$

In the last three equations, k_x and k_y are quasimomentum operators that act on quasimomentum basis states $|k_x\rangle$ and $|k_y\rangle$, respectively. The Hamiltonian is diagonal in quasimomentum representation and the eigenstates are of the Bloch form. The corresponding energy is given by,

$$E(k_x, k_y) = -2\mathcal{J}(\cos(k_x) + \cos(k_y)), \tag{2.7}$$

which is a single Bloch band of width $8\mathcal{J}$.

2.1.1 Peierls Substitution and Magnetic Translation Operators

In continuum, the Schrödinger equation for a charged particle (say an electron) in a magnetic field is derived from a canonical formalism, which is expressed in terms of vector potentials [47]. The corresponding Hamiltonian can also be simply obtained through minimal substitution, i.e. by replacing the momentum $\vec{p}$ of the free particle by its gauge-invariant form $\vec{\Pi}$, i.e.

$$\vec{p} \rightarrow \vec{\Pi} = \vec{p} + e\vec{A}(\vec{r}), \tag{2.8}$$

with the electronic charge $Q = -e$. The Hamiltonian, for a particle of mass m_o, takes the following form:

$$\hat{H} = \frac{(\vec{p}(\vec{r}) + e\vec{A}(\vec{r}))^2}{2m_o}, \tag{2.9}$$

here $\vec{\Pi}$ is known as the kinetic momentum and $\vec{p}$ as canonical momentum. The kinetic momentum, proportional to the particle velocity, is gauge-invariant and hence is a physical quantity [4]. The vector potential $\vec{A}(\vec{r})$, generating the static magnetic field ($\vec{B}(\vec{r}) = \nabla \times \vec{A}(\vec{r})$) and the canonical momentum $\vec{p}$ are gauge-dependent quantities. There are infinite number of ways of writing the vector potential $\vec{A}(\vec{r})$ for a single magnetic field $\vec{B}(\vec{r})$ without changing the physics of the problem. For example adding the gradient of an arbitrary differentiable function $f(\vec{r})$ to the vector potential $\vec{A}(\vec{r})$, i.e. $\vec{A'}(\vec{r}) = \vec{A}(\vec{r}) + \nabla f(\vec{r})$ gives the same magnetic field $\vec{B}(\vec{r}) = \nabla \times \vec{A'}(\vec{r})$ since the curl of a gradient is zero, i.e. $\nabla \times \nabla f(\vec{r}) = 0$. The canonical momentum $\vec{p}$, being a gauge dependent quantity, transfroms to $\vec{p} - e\nabla f(\vec{r})$ in order to leave the kinetic momentum ($\vec{\Pi}$) unchanged. Another important fact is that a wavefunction $\psi(r,t)$, which is a solution of the Schrödinger equation for the gauge choice $\vec{A}(\vec{r})$, will generally not be its solution for the other gauge choice $\vec{A'}(\vec{r})$ [46, 48]. The wavefunction transforms with the gauge transformation in the following way:

$$\psi(r,t) \rightarrow \psi'(r,t) = e^{-ief(\vec{r})/\hbar} \psi(r,t). \tag{2.10}$$
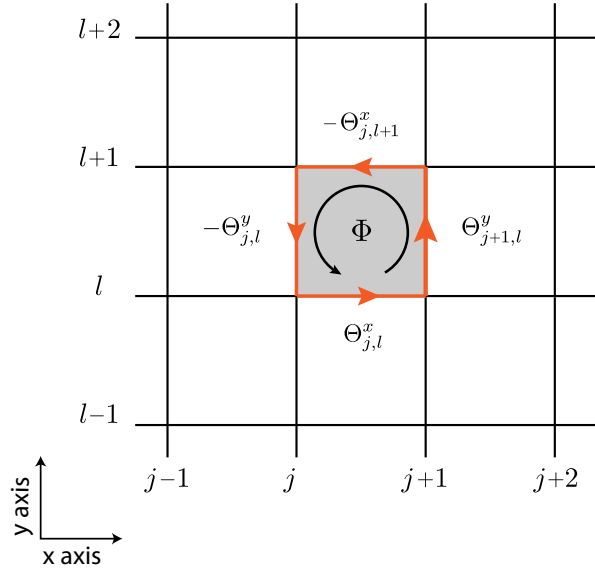
Figure 2.1: Schematic of Peierls phases around a unit cell of a 2D lattice. In the presence of a vector potential $\vec{A}(\vec{r})$, the tunnel amplitudes are accompanied by phase factors and hence are complex quantities. A particle accumulates a phase $\Theta_{j,l}^{x}$ or $\Theta_{j,l}^{y}$ while shifting from one lattice site to its neighboring site along the sides of a unit cell in the positive x or y direction respectively. The integrated phase around a unit cell of the lattice is equal to the flux (Φ, equivalent to Aharonov–Bohm phase) of the magnetic field passing through the cell.

For a particle on a tight-binding lattice, the presence of a magnetic field is taken into account through the so called Peierls substitution[2] [50]. This is accomplished by assigning complex values to the tunneling amplitudes of eq. (2.3). In the presence of a magnetic field $\vec{B}(\vec{r}) = \nabla \times \vec{A}(\vec{r})$, the Peierls substitution is equivalent to approximate the Hamiltonian (eq. (2.3)) in the following way:

$$\hat{H}_{\text{TB,Peierls}} = -\mathcal{J} \sum_{j,l} \left(e^{i\Theta_{j,l}^{x}} \, \hat{c}_{j+1,l}^{\dagger} \hat{c}_{j,l} + e^{i\Theta_{j,l}^{y}} \, \hat{c}_{j,l+1}^{\dagger} \hat{c}_{j,l} + \text{h.c.} \right), \qquad (2.11)$$

with phases $\Theta_{j,l}^{x}$ and $\Theta_{j,l}^{y}$ are known as Peierls phases and can be computed as the integral of the vector potential $\vec{A}(\vec{r})$ over the path joining the nearest neighboring lattice sites, i.e.

$$\Theta_{j,l}^{x} = \frac{e}{\hbar} \int_{j,l}^{j+1,l} \vec{A}(\vec{r}) \cdot d\vec{r},$$

$$\Theta_{j,l}^{y} = \frac{e}{\hbar} \int_{j,l}^{j,l+1} \vec{A}(\vec{r}) \cdot d\vec{r}, \qquad (2.12)$$

---

[2] In case of electrons on a lattice, the justification of Peierls substitution is not straightforward as there are a number of energy bands involved. However, for the lattice constant much smaller than the magnetic length scale $\left(\ell_B = \sqrt{\hbar/(eB(\vec{r}))} \right)$, this substitution is valid. In other words, this substitution is valid as long as the energy scale set by magnetic field is much smaller than the energy gap between the two lowest Bloch bands, so that contributions from the higher bands can be neglected. In the case of simulating this physics in experiments with cold neutral atoms, the effect of magnetic fields is recreated synthetically by direct engineering of Aharonov–Bohm geometric phases and justifications for the validity of the Peierls substitution are not relevant. These experiments are performed in the tight-binding regime where neutral atoms are confined to the lowest Bloch band that is separated form other bands by a larger gap [4, 30, 46, 49].

where the sign of the charge is included in "e". Due to the gauge freedom of the vector potential $\vec{A}(\vec{r})$, for a given physical problem the choice of the Peierls phases $(\Theta^x_{j,l}, \Theta^y_{j,l})$ is not unique. However, the sum of the Peierls phases around a closed path in the lattice is a gauge invariant quantity. For a particle hopping counterclockwise around a unit cell of the lattice (fig. 2.1), the sum of the Peierls phases is equal to the Aharonov–Bohm phase accumulated by the particle,

$$\Theta^x_{j,l} + \Theta^y_{j+1,l} - \Theta^x_{j,l+1} - \Theta^y_{j,l} = \frac{e}{\hbar} \oint_{unitcell} \vec{A}(\vec{r}) \cdot d\vec{r}$$
$$= 2\pi \frac{\Phi}{\Phi_0}, \tag{2.13}$$

where (j, l) are the coordinates of the lower left corner of the unit cell. The flux ratio $\phi = \Phi/\Phi_0$ is an important parameter of the problem. Equation (2.13) can be written in terms of discrete lattice derivatives, i.e.

$$(\Theta^y_{j+1,l} - \Theta^y_{j,l}) - (\Theta^x_{j,l+1} - \Theta^x_{j,l}) = \Delta_x \Theta^y_{j,l} - \Delta_y \Theta^x_{j,l}$$
$$= 2\pi \phi_{j,l}. \tag{2.14}$$

For convenience, we introduce shift operators $\hat{S}_x$ and $\hat{S}_y$ for translating a particle in the x and the y direction by one lattice site in the presence of a magnetic field $\vec{B}(\vec{r})$. These operators can be expressed in terms of kinetic momentum $\vec{\Pi}$ in the following way:

$$\hat{S}_x = e^{-i\vec{\Pi}\hat{j}/\hbar} = e^{(-i(\vec{p}+e\vec{A}(\vec{r}))\hat{j}/\hbar)} \quad \rightarrow \sum_{j,l} e^{i\Theta^x_{j,l}} \hat{c}^\dagger_{j+1,l} \hat{c}_{j,l}$$

$$\hat{S}_y = e^{-i\vec{\Pi}\hat{l}/\hbar} = e^{(-i(\vec{p}+e\vec{A}(\vec{r}))\hat{l}/\hbar)} \quad \rightarrow \sum_{j,l} e^{i\Theta^y_{j,l}} \hat{c}^\dagger_{j,l+1} \hat{c}_{j,l} \tag{2.15}$$

These operators acts on the single-particle states ($|\psi_{j,l}\rangle = \hat{c}^\dagger_{j,l}|0\rangle = |j,l\rangle$) resulting in the translation of the particle in the lattice and implement the Peierls phases,

$$\hat{S}_x |j,l\rangle = e^{i\Theta^x_{j,l}} |j+1,l\rangle,$$
$$\hat{S}_y |j,l\rangle = e^{i\Theta^y_{j,l}} |j,l+1\rangle. \tag{2.16}$$

The Hamiltonian (eq. (2.11)) can be written in terms of these translation operators,

$$\hat{H}_{\text{TB,Peierls}} = -\mathcal{J}(\hat{S}_x + \hat{S}_y + \hat{S}^\dagger_x + \hat{S}^\dagger_y). \tag{2.17}$$

The tight-binding Hamiltonian in this form has the merit to make clear the action of the Peierls substitution.

In the presence of a magnetic field, the translation symmetry of the problem is broken and quasimomentum is not a conserved quantity. The Hamiltonian (eq. (2.17)) is not translational invariant with translation operators $\hat{S}_x$ and $\hat{S}_y$. These operators neither commute with each other nor with the Hamiltonian, as it can be shown that

$$\hat{S}_y \hat{S}_x = e^{(i2\pi\phi)} \hat{S}_x \hat{S}_y, \tag{2.18}$$

which differs by a multiplicative factor. The reason is that the vector potential $\vec{A}(\vec{r})$ is not translation invariant even for a constant magnetic field B. The symmetry of the Hamiltonian can be restored by defining the so called magnetic translation operators (MTOs) $\{\hat{T}_x, \hat{T}_y\}$ [51–53]. These operators differ by a

phase factor from the shift operators $\{\hat{S}_x, \hat{S}_y\}$ and can be obtained by making a gauge transformation [54],

$$
\begin{aligned}
\hat{T}_x &\equiv \sum_{j,l} \hat{c}^{\dagger}_{j+1,l} \hat{c}_{j,l} e^{i\mathcal{X}^x_{j,l}}, \\
\hat{T}_y &\equiv \sum_{j,l} \hat{c}^{\dagger}_{j,l+1} \hat{c}_{j,l} e^{i\mathcal{X}^y_{j,l}}.
\end{aligned}
\tag{2.19}
$$

The phases $\mathcal{X}^x_{j,l}$ and $\mathcal{X}^y_{j,l}$ are different from the Peierls phases given in eq. (2.12) and can be determined from the requirement that the MTOs should commute with the Hamiltonian. The required conditions can be obtained by applying the commutator of MTOs with the shift operators eq. (2.15) on a single-particle state, i.e. $[\hat{S}_i, \hat{T}_{i'}] |j, l\rangle$ for $i, i' \in \{x, y\}$, and setting them equal to zero. Details on deriving the constraints on Θ and $\mathcal{X}$ can be found in [54, 55]; however, for completeness of this chapter, these are presented in Appendix A. The values of $\mathcal{X}^{x,y}$, for which the MTOs commute with the Hamiltonian eq. (2.17), are given by

$$
\begin{aligned}
\mathcal{X}^x_{j,l} &= \Theta^x_{j,l} + 2\pi l \phi_{j,l}, \\
\mathcal{X}^y_{j,l} &= \Theta^y_{j,l} - 2\pi j \phi_{j,l}.
\end{aligned}
\tag{2.20}
$$

The MTOs with these phases commute with the Hamiltonian but they still do not commute with each other, i.e. $[\hat{T}_x, \hat{T}_y] \neq 0$. Their commutators can be obtained by applying these operators on a single-particle states on a lattice site (j, l),

$$
\begin{aligned}
\hat{T}_x \hat{T}_y \, \hat{c}^{\dagger}_{j,l} |0\rangle &= \hat{T}_x \, e^{i\mathcal{X}^y_{j,l}} \hat{c}^{\dagger}_{j,l+1} |0\rangle = e^{i\left(\mathcal{X}^x_{j,l+1} + \mathcal{X}^y_{j,l}\right)} \hat{c}^{\dagger}_{j+1,l+1} |0\rangle, \\
\hat{T}_y \hat{T}_x \, \hat{c}^{\dagger}_{j,l} |0\rangle &= \hat{T}_y \, e^{i\mathcal{X}^x_{j,l}} \hat{c}^{\dagger}_{j+1,l} |0\rangle = e^{i\left(\mathcal{X}^y_{j+1,l} + \mathcal{X}^x_{j,l}\right)} \hat{c}^{\dagger}_{j+1,l+1} |0\rangle,
\end{aligned}
\tag{2.21}
$$

which show that the two operators do not commute. It is, however, possible to find a combination of these operators which do commute with each other [54]. Before finding this combination, it is important to fix a gauge for the vector potential $\vec{A}(\vec{r})$ as it is required to write the specific form of the MTOs.

Let us consider the case of uniform magnetic field $\vec{B}$ with the Landau gauge $\vec{A}(\vec{r}) = (0, Bx, 0)$. In this case the flux ratio through each cell of the lattice is uniform, i.e. ϕ. By using the values of the phases given in eq. (2.20), eq. (2.21) can be written as

$$
\hat{T}_x \, \hat{T}_y = e^{i2\pi\phi} \hat{T}_y \, \hat{T}_x,
\tag{2.22}
$$

or equivalently,

$$
\hat{T}^{\dagger}_x \, \hat{T}^{\dagger}_y \, \hat{T}_x \, \hat{T}_y = e^{i2\pi\phi}.
\tag{2.23}
$$

This shows that a particle hopping clockwise around a unit cell of the lattice accumulates a phase $2\pi\phi$. If this phase is an integer multiple of 2π, i.e. ϕ is equal to an integer number, then the MTOs commute with each other. However, this is gauge-equivalent to zero magnetic flux through a unit cell of the lattice and hence do not result in the desired interesting physics [55]. The interesting physics emerges when the values of ϕ are not integer numbers. In this case combinations of MTOs do not generally commute. As an example we can take the following combination of MTOs,

$$
\hat{T}^q_x \, \hat{T}_y = e^{i2q\pi\phi} \hat{T}_y \, \hat{T}^q_x,
\tag{2.24}
$$

which shows that for any integer value of q, the MTOs do not commute. However, for this combination
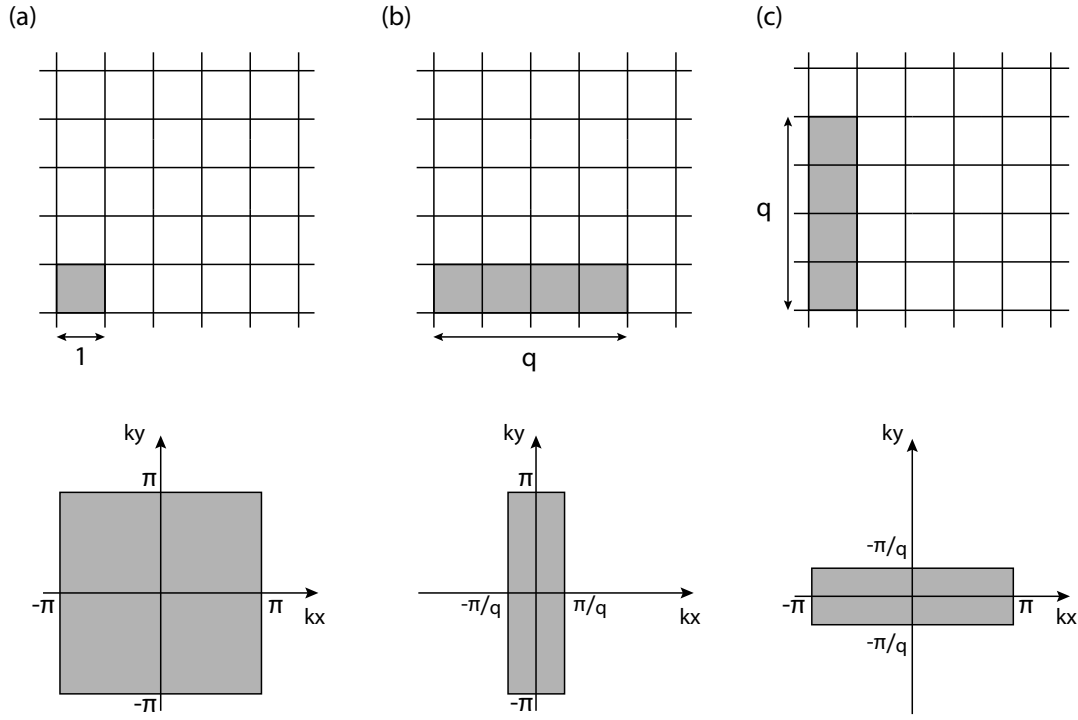
Figure 2.2: Schematic illustration of a magnetic unit cell and the corresponding MBZ. In each (a, b, c) case, real space unit cell is accompanied by the corresponding BZ directly below it in the same column. (a) For a normal unit cell of the 2D square lattice with lattice constant 1 in both directions, the BZ is a square with $-\pi \leq k_x < \pi$ and $-\pi \leq k_y < \pi$. (b) In the presence of a magnetic field with flux ratio $\phi = p/q$, the magnetic unit cell of the problem is q-times larger in the x direction than the normal unit cell of the lattice. The corresponding MBZ is q-times smaller along k_x with $-\pi/q \leq k_x < \pi/q$ and $-\pi \leq k_y < \pi$. (c) For the same problem, one can equally choose the magnetic unit cell to be oriented along the y axis of the lattice. In this case, the MBZ is q-times smaller along k_y with $-\pi \leq k_x < \pi$ and $-\pi/q \leq k_y < \pi/q$. In both (b,c) cases, the area of the magnetic unit cell is important, which is constant ($q \times 1 = 1 \times q$) irrespective of its orientation.

of MTOs, if one considers only rational values of the flux ratio, i.e. $\phi = p/q \in \mathbb{Q}$ with p and q relatively prime integers, then they commute with each other,

$$\hat{T}_x^q \, \hat{T}_y = \hat{T}_y \, \hat{T}_x^q. \tag{2.25}$$

For this specific case of flux ratio, the new MTOs $\{\hat{T}_x^q, \hat{T}_y\}$ along with the Hamiltonian (eq. (2.17)) define a set of good quantum numbers, as the new MTOs also commute with the Hamiltonian. The simultaneous eigenstates of $\{\hat{H}_{\mathrm{TB,Peierls}}, \hat{T}_x^q, \hat{T}_y\}$ are known as magnetic Bloch states, i.e. $\psi_{j,l,k} = e^{-ijk_x}e^{-ilk_y}\,|j,l,k\rangle$, satisfying the generalized form of Bloch theorem,

$$\hat{H}_{\mathrm{TB,Peierls}}\psi_{j,l,k} = E_{k_x,k_y}\psi_{j,l,k},$$
$$\hat{T}_x^q\psi_{j,l,k} = e^{-iqk_x}\psi_{j,l,k},$$
$$\hat{T}_y\psi_{j,l,k} = e^{-ik_y}\psi_{j,l,k}, \tag{2.26}$$

with lattice constant of unit length in both directions. An important fact is that for an eigenstate $\psi_{j,l,k}$ of the Hamiltonian $\hat{H}_{\mathrm{TB,Peierls}}$, the spatially translated states $\{\hat{T}_x^{j'}\psi_{j,l,k};\ j' = 1, 2, \dots, q-1\}$ have different

eigenvalues under $\hat{T}_y$, i.e. $\hat{T}_y \left(\hat{T}_x^{j'} \psi_{j,l,k} \right) = e^{i(k_y - 2\pi j' \phi)} \left(\hat{T}_x^{j'} \psi_{j,l,k} \right)$. All these spatially translated states are different, but have the same energy as that of $\psi_{j,l,k}$. The reason is that the operator $\hat{T}_x^{j'}$ commutes with the Hamiltonian $\hat{H}_{\text{TB,Peierls}}$ for all integer values of j'. This results in q-fold degeneracy of the energy along k_y.

The MTO $\hat{T}_x^q$ shifts a particle by q lattice sites along the x and $\hat{T}_y$ by one lattice site along the y axis of the lattice. In the new symmetry of the problem, the dimension of the unit cell is $q \times 1$, which is q-times larger in the x direction[3] than that of the normal unit cell of the 2D lattice. The *magnetic unit cell* is the only one, which is composed of q plaquettes of the lattice. The corresponding magnetic Brillouin zone (MBZ) is q-times smaller than the normal BZ in the k_x direction, i.e. $-\pi/q \le k_x < \pi/q$ and $-\pi \le k_y < \pi$, as schematically illustrated in fig. 2.2.

2.2 Harper's Equation and the Hofstadter Spectrum

Let us compute the spectrum of the single-particle system in the presence of a uniform external magnetic field. As for a given magnetic field, the physical observable of the system is independent of the gauge choice, I continue with the choice of Landau gauge $\vec{A}(\vec{r}) = (0, Bx, 0)$ for computational simplicity. In this gauge, the tunneling amplitude along the x axis of the lattice is real and is complex along the y axis, i.e. $\Theta_{j,l} = (0, 2\pi j \phi)$. The tight binding Hamiltonian has the following form,

$$\hat{H} = -\mathcal{J} \sum_{j,l} \left(\hat{c}_{j+1,l}^\dagger \hat{c}_{j,l} + e^{i2\pi j\phi} \hat{c}_{j,l+1}^\dagger \hat{c}_{j,l} + \text{h.c.} \right), \tag{2.27}$$

where the phases (eq. (2.20)) of the MTOs reduce to

$$\begin{aligned} \mathcal{X}_{j,l}^x &= 2\pi l \phi_{j,l}, \\ \mathcal{X}_{j,l}^y &= 0. \end{aligned} \tag{2.28}$$

We consider only rational values of the flux ratio $\phi = p/q$. In this case, the system has translational invariance with a magnetic unit cell of dimensions $q \times 1$. This is q-times larger than the normal unit cell of the lattice and is oriented along the x-axis of the lattice. For convenience, I regroup the 2D lattice into magnetic unit cells. There are q different sites in each unit cell. The position basis on this spatially regrouped lattice can be written as

$$|j, l\rangle \quad \rightarrow \quad |jq + j', l\rangle = |jq\rangle \otimes |j', l\rangle, \tag{2.29}$$

here $j \in \mathbb{Z}$ is the index of the jth magnetic unit cell and $j' = 1, 2, \ldots, q$ represents different sites within each magnetic unit cell. By modifying the creation and annihilation operators $(\hat{c}_{j,l}^\dagger, \hat{c}_{j,l})$ according to this spatial regrouping, the Hamiltonian eq. (2.27) can be written as

$$\hat{H} = -\mathcal{J} \sum_{j,j',l} \left(\hat{c}_{jq+j'+1,l}^\dagger \hat{c}_{jq+j',l} + e^{i2\pi(jq+j')\phi} \hat{c}_{jq+j',l+1}^\dagger \hat{c}_{jq+j',l} + \text{h.c.} \right). \tag{2.30}$$

Due to the new translational symmetry in the x direction and the normal translational symmetry in the y direction, the Hamiltonian eq. (2.30) can be transformed into quasimomentum space. Using the

---

[3] The area of the magnetic unit cell is fixed by the strength of the magnetic flux. For a flux ratio p/q, the area of the magnetic unit cell is q-times larger than the normal unit cell of the lattice. However, its dimension can be arbitrarily chosen, where, depending on the gauge choice, the MTOs take different form [55]. see fig. 2.2 for schematic illustration.

transformation given in Appendix B, the Hamiltonian takes the following form,

$$\hat{H} = \frac{q}{(2\pi)^2} \int_{-\pi/q,-\pi}^{+\pi/q,+\pi} dk_x \, dk_y \otimes \left[-\mathcal{J} \sum_{j'} \left(e^{-ik_x} \, \hat{c}^{\dagger}_{k_x,ky,j'+1} \, \hat{c}_{k_x,ky,j'} \right. \right.$$

$$\left. \left. + \, e^{ik_x} \, \hat{c}^{\dagger}_{k_x,ky,j'-1} \, \hat{c}_{k_x,ky,j'} + 2\cos(2\pi\phi j' - k_y) \, \hat{c}^{\dagger}_{k_x,ky,j'} \, \hat{c}_{k_x,ky,j'} \right) \right]$$

$$= \frac{q}{(2\pi)^2} \int_{-\pi/q,-\pi}^{+\pi/q,+\pi} dk_x \, dk_y \otimes \hat{\mathcal{H}}(k_x, k_y). \tag{2.31}$$

This Hamiltonian is diagonal inside the MBZ. The kernel $\hat{\mathcal{H}}(k_x, k_y)$, that contains all the information of the Hamilton, is a $q \times q$ Hermitian matrix (there are q states per magnetic unit cell). It is important to mention that $\hat{\mathcal{H}}(k_x, k_y)$ is normally known as the Hamiltonian, however, it is only part of the Hamiltonian ($\hat{H}$) and is a gauge-dependent quantity. For different gauge choices, $\hat{\mathcal{H}}(k_x, k_y)$ takes different forms, but the Hamiltonian $\hat{H}$ remains invariant. The energy eigenvalues are obtained by solving the Schrödinger equation,

$$\hat{\mathcal{H}}(k_x, k_y) \, \psi_k = E_{k_x,k_y} \, \psi_k. \tag{2.32}$$

This is similar to the eigenvalue problem of a particle hopping on a 1D cyclic chain of q sites with tunneling amplitude $-\mathcal{J}e^{ik_x}$ in one direction, $-\mathcal{J}e^{-ik_x}$ in the other direction, and with the onsite energy term $-2\mathcal{J}\cos(2\pi\phi j' - k_y)$. In the tight-binding single-band approximation, the eigenstates of the matrix $\hat{\mathcal{H}}(k_x, k_y)$ can be expressed in terms of single-particle states, which are localized on the single sites of the magnetic unit cell,

$$\psi_k = \sum_{i=1}^{q} a_i \, \hat{c}^{\dagger}_{k_x,k_y,i} \, |0\rangle . \tag{2.33}$$

Inserting this ansatz for the wavefunction in eq. (2.32) results in the following equation,

$$- \mathcal{J}(2 \cos(2\pi\phi j' - k_y) \, a'_j + e^{-ik_x} \, a_{j'-1} + e^{ik_x} \, a_{j'+1}) = E_{k_x,k_y} \, a_{j'}, \tag{2.34}$$

with the boundary condition $j' + q = j'$. This equation is the well-known Harper equation, whose energy eigenvalues form the well-known Hofstadter spectrum and has been extensively studied [24, 45]. In matrix form, this equation can be written as

$$-\mathcal{J} \begin{pmatrix} h_1 & e^{ik_x} & 0 & \cdots & 0 & e^{-ik_x} \\ e^{-ik_x} & h_2 & e^{ik_x} & \cdots & 0 & 0 \\ 0 & e^{-ik_x} & h_3 & \cdots & 0 & 0 \\ \vdots & \vdots & \vdots & \ddots & \vdots & \vdots \\ 0 & 0 & 0 & \cdots & h_{q-1} & e^{ik_x} \\ e^{ik_x} & 0 & 0 & \cdots & e^{-ik_x} & h_q \end{pmatrix} \begin{pmatrix} a_1 \\ a_2 \\ a_3 \\ \vdots \\ a_{q-1} \\ a_q \end{pmatrix} = E_{k_x,k_y} \begin{pmatrix} a_1 \\ a_2 \\ a_3 \\ \vdots \\ a_{q-1} \\ a_q \end{pmatrix}, \tag{2.35}$$

with onsite energy term

$$- \mathcal{J} \, h_{j'} = -2\mathcal{J} \cos(2\pi\phi j' - k_y); \quad \text{for } j' = 1, 2, \ldots, q. \tag{2.36}$$

By diagonalizing the matrix, one obtains q energy eigenvalues, i.e. $E^{(1)}_{k_x,k_y}, E^{(2)}_{k_x,k_y}, \ldots, E^{(q)}_{k_x,k_y}$ along with q eigenstates $\psi^{(1)}_k, \psi^{(2)}_k, \ldots, \psi^{(q)}_k$. The energy eigenvalues as a function of the quasimomentum k_x and k_y inside the first MBZ form q subbands that are known as magnetic-Bloch bands. For the chosen Landau
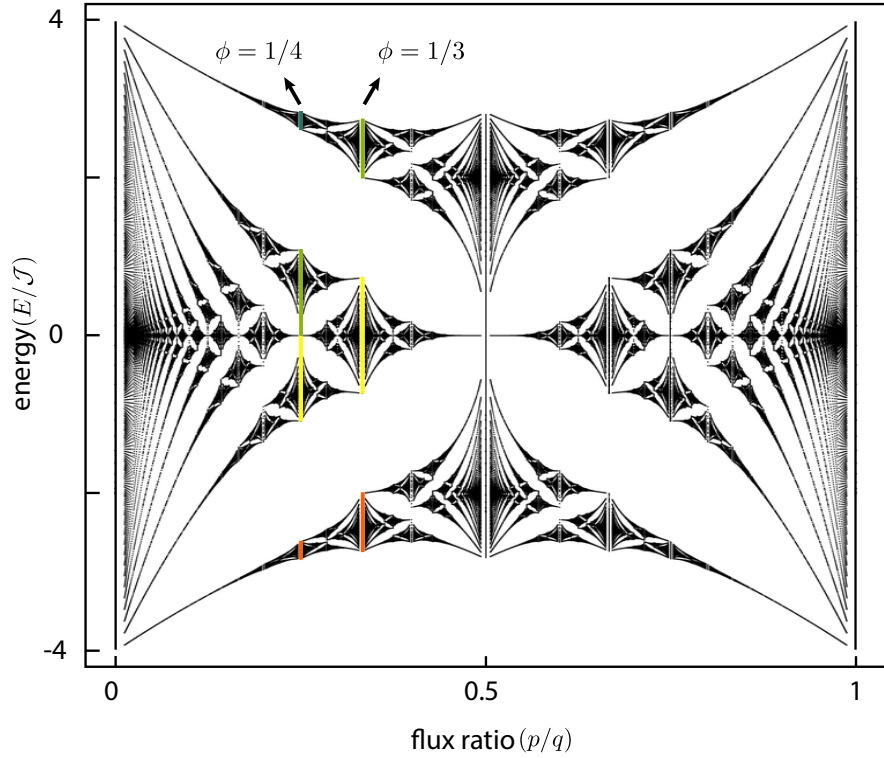
Figure 2.3: Hofstadter butterfly: Energy spectrum of the Harper's equation plotted against rational values of flux ratio ϕ. For $\phi = p/q$, the lowest Bloch band splits into q number of magnetic Bloch bands. The energy spectrum has fractal structure and was first computed by D. Hofstadter [24]. Here, it is computed for q up to 80 and (k_x, k_y) within the first MBZ. The color line-segments represent the magnetic Bloch bands for $\phi = 1/4$ and $\phi = 1/3$, for which the energy dispersion is shown in fig. 2.5.

gauge, a given energy value is q-fold degenerate along the k_y direction, i.e. $E_{k_x, k_y} = E_{k_x, k_y + 2\pi j' p/q}$ for $j' = 1, 2, \ldots, q$. Another important fact is that for odd values of q, the magnetic Bloch bands are gapless, however for even values of q, the energy dispersion consist of q number of isolated zeros around which the particle behaves like a Dirac fermion [56].

In the weak field regime, the role of magnetic field is perturbative and the structure of the Bloch state is marginally affected. However, in the limit of strong magnetic fields, a single Bloch band splits into q number of magnetic-Bloch bands. When the energy spectrum is plotted as a function of rational values of the flux ratio $\phi = p/q$; $p/q : 0 \rightarrow 1$, one obtains the famous Hofstadter spectrum, also known as Hofstadter butterfly [24]. Figure 2.3 shows this spectrum, which is computed for q up to 80 and (k_x, k_y) in the first MBZ.

2.3 Topological Properties of the Hofstadter Spectrum

2.3.1 A Brief Introduction to Topology

Topology is a discipline of mathematics that studies the geometrical properties of objects that are invariant under continuous deformations. A simple mathematical example for explaining this concept is that of a cylinder and a Möbius strip. On local inspection the two surfaces look exactly equivalent to one another.

However, when inspected in their entirety, one realises that a Möbius strip is different from a cylinder due to the presence of a twist. By smooth changes to the surface of the Möbius strip, one can deform its surface locally but the twist can cannot be removed unless the ribbon itself is dissected. In other words, a Möbius strip cannot be continuously transformed to a cylinder and hence the two are topologically distinct objects with distinct topological invariants. The topological invariant in this case is the number of twists in the surface.

Another simple example is that of a sphere and a doughnut. Both are 2D closed surfaces in 3D, but are topologically distinct as one cannot be continuously transformed to the other. The topological invariant in this case is the genus g of the surface, which counts the number of holes in it. A sphere has a genus $g = 0$ and a doughnut has a genus $g = 1$. As the topological invariants take only discrete values, they cannot be changed by making smooth changes to the surface. For geometrical surfaces, the associated topological invariants can be obtained using the famous Gauss-Bonnet theorem [7, 57]. According to this theorem, an integer topological invariant, i.e. Euler characteristic χ (a global quantity describing the shape of the topological space) of an orientable[4] closed surface, is defined as

$$\chi = \frac{1}{2\pi} \int_{\text{surface}} \mathcal{K} dA, \tag{2.37}$$

with $\mathcal{K}$ being the Gaussian curvature of the surface (local quantity). For a sphere of radius $\mathcal{R}$, the Gaussian curvature is $\mathcal{K} = 1/\mathcal{R}^2$ which gives $\chi = 2$. The Euler characteristic of the surface is related to its genus via the relation $\chi = 2 - 2g$. This relation shows that Euler characteristic is quantized. In this example, the curvature of the surface is a local (geometrical) quantity and can be changed by smooth deformations. However, the integral of the curvature is a global (topological) quantity, which remains robust against smooth deformations.

In physics, the concepts of topology were first introduced for describing IQHE [5] and since then have been used for understanding and classifying new phases of quantum matter, i.e. topological insulators. The universality of IQHE and the extreme precision of the quantization were natural indications of its topological origin. It was shown that the fundamental origin of this phenomenon is due to the topological nature of the bulk states, which can be characterized by a topological invariant. The invariant (which is the Chern number here) encodes the global structure of the wavefunctions and represent discret physical quantities, e.g. quantized Hall conductance. In contrast to the twist and hole taking place in Euclidian space (fig. 2.4), in condensed matter physics a topological invariant, e.g. a winding number or a Chern number, characterizes the global structure in a more abstract space (Hilbert space). This space is formed by the eigenstates belonging to certain energy bands (see for example fig. 3.6 in Chapter 3, where topological invariant of the system is equal to the winding of the eigenvector in the equatorial plane of a Bloch sphere). Topological invariants remain robust against smooth changes in the system's parameters, as long as the gap closing conditions and relevant symmetries, if exist, are respected.

Topological order in a topological insulating material is hidden in its bulk, but its physical consequence is apparent in the form of highly non-trivial edge phenomena. These phenomena, in general, depends on the dimensionality of a system and are protected by certain symmetries. For example, in a quantum Hall system underlying a lattice, the non-trivial topological structure of the bulk bands is characterized by Chern numbers, and unidirectionally propagating edge states exist along its boundary, carrying a quantized current. These states are hallmark of the non-trivial topology in the bulk and are known as TP

---

[4] A sphere, a plane and a torus are examples of orientable surfaces having well-defined sides. The Möbius strip, being a single side surface due to the fact that one side of the strip is joined to the other side, is an example of a non-orientable surface. The orientation of a surface is specified by a normal at each point of the surface. For an orientable surface there are two possible orientation and hence two normals which are opposite to one another.
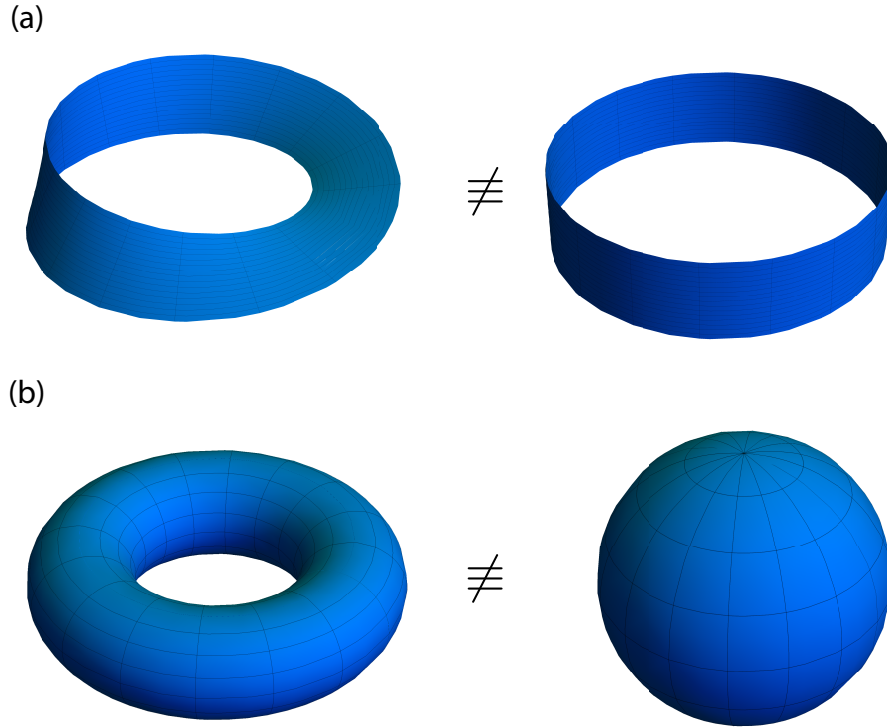
Figure 2.4: Examples of topologically non-equivalent surfaces in an Euclidian space. (a) A Möbius strip has distinct topology than a cylinder due to the presence of a twist in its surface. The twist cannot be removed by smooth deformations to the surface unless the ribbon is dissected. The number of twists constitute the topological invariant of the surface which is 1 for the Möbius strip and 0 for the cylinder. (b) Similarly, a doughnut has distinct topology than a sphere and cannot be transformed to one another by smooth deformations. The topological invariant is the genus (g) of the surface which is $g = 1$ for a doughnut and $g = 0$ for a sphere.

edge states. These states are protected by gaps in the bulk spectrum and remain robust against impurities and smooth changes.

2.3.2 Topological Order in the Bulk: Chern Numbers of the Magnetic Bloch Bands

The topological character of the bulk states, associated with a quantum Hall system underlying a 2D periodic potential, was first established by D. J. Thouless et al. [5]. The system, they considered, was a Landau quantized system subjected to a weak periodic potential. Due to the weak potential, each Landau level broadens to a Landau band and splits into a number of subbands. For this system, they showed that the Hall conductance is not only quantized for the Fermi level in a gap between two Landau levels, but is also quantized for the Fermi level in the mini gaps within subbands of a Landau level. The conductance of each isolated Landau subband is an integer multiple of the conductance of the entire Landau level. For a flux ratio $\phi = p/q$, the integer of the conductance can be determined from the Diophantine equation,

$$r = qs_r + pt_r, \tag{2.38}$$

with r is the gap index which can take values $0 \leq r \leq q$, s_r and t_r (where $|t_r| \leq q/2$) are integer numbers with subscript r showing the fact that the two take different values for different gaps. It was shown that t_r is the quantization integer of the Hall conductance in the rth gap [58]. For the Fermi level lying in a gap,
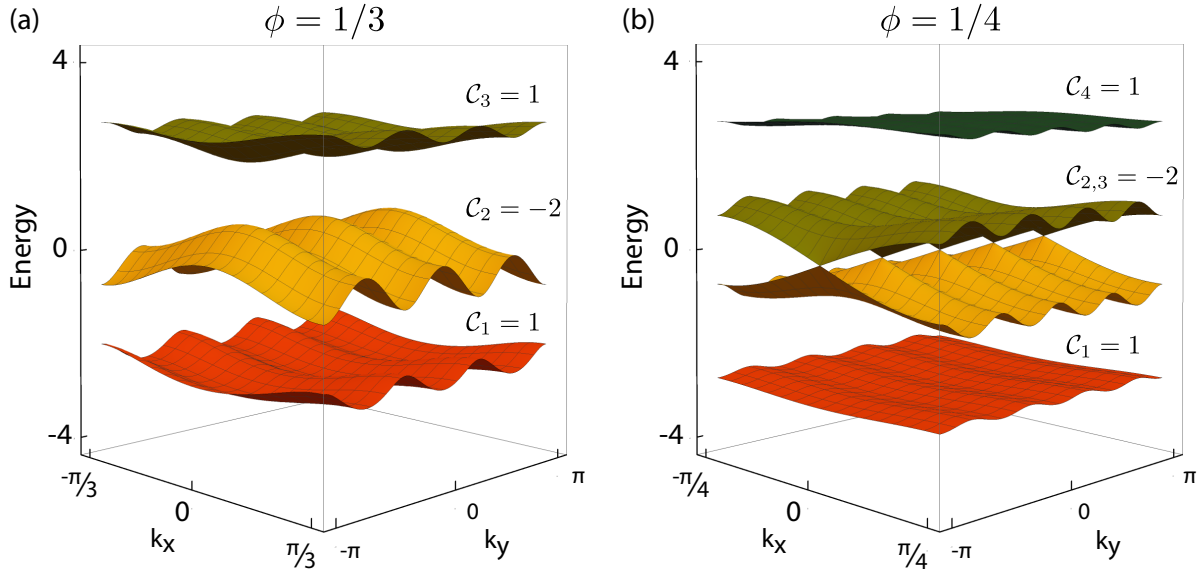
Figure 2.5: Energy dispersion of magnetic-Bloch bands inside the first magnetic BZ. (a) For $\phi = 1/3$, a single Bloch band splits into three magnetic-Bloch bands. The resultant bands have non-trivial topological structure which is shown by their non-zero values of Chern numbers. The sum of the Chern numbers of all magnetic-Bloch bands is zero. (b) Energy spectrum for the case of $\phi = 1/4$ consists of four magnetic-Bloch bands with the inner most two bands touching each other. The dispersion closed to the touching points is similar to dispersion of Dirac fermions. These two bands are separated by a gap from the uppermost and lowermost bands and hence are characterized by single Chern number. This spectrum is numerically computed for isotropic tunneling amplitude $\mathcal{J} = 1$.

the same integer can be determined by evaluating the first Chern number of the bulk states over the MBZ. The Hall conductance of a band is directly related to its Chern number. For the Fermi level in the rth gap of the energy spectrum, the Hall conductance (σ_H) of the system, in terms of the Chern numbers of the bulk bands, is

$$\sigma_H = \left(\frac{Q^2}{h}\right) \sum_{i=1}^{r} C_i, \tag{2.39}$$

here Q is the electronic charge and C_i is the Chern number of the ith band. The summation is carried over all filled bands. The non-zero values of the Chern numbers reflect the non-trivial topological nature of the bulk states of the quantum Hall system.

The configuration introduced in sec. 2.2, is complementary but mathematically equivalent to the problem of Landau levels. Here the magnetic field is treated as a perturbation on a tightly bonded system, which results in the splitting of a Bloch band into the so called magnetic Bloch bands. These bands have translational symmetry and topological properties different than the normal Bloch bands[5]. In contrast to normal Bloch bands, magnetic Bloch bands are topologically non-trivial, i.e. they are characterized

---

[5] For normal Bloch states, phases at different points in the BZ are generally not related to each other and can be defined independently. The requirements on these phases are that they should be continous and differentiable so that the wavefunctions are well behaved. However, in the presence of a magnetic field, it is not possible to define a unique and smooth global phase for the wavefunction over the whole MBZ unless the magnetic Bloch band carries no current. For a zero in the wavefunction in the MBZ, the phase is ill-defined, which introduces a singularity in the Berry's connection. The zero in the wavefunction is regarded as a vortex with vorticity +1 or −1. The Chern number is equal to the total vorticity of the wavefunction in the MBZ.

by non-vanishing Chern numbers. As an example, the dispersion of the bulk spectrum[6] of the Harper's Hamiltonian (eq. (2.34)), for the case of $q = 3$ and $q = 4$, is shown in fig. 2.5. The Chern number of each magnetic Bloch band is indicated, which reflects the non-trivial topological structure of the bulk states constituting these bands.

I compute the Chern number of a band using the method proposed by Fukui et al. [59]. The procedure of the numerical computation of the Chern number is summarized in Appendix C. The Chern number is computed for a band or a set of bands (in case of touching bands) separated by energy gaps from other bands. In fig. 2.5 (a), there are three bands which are separated by gaps and hence Chern number is computed for each isolated band. In fig. 2.5 (b), there are four bands, however, the middle two bands are touching each other. They are separated by gaps from the lowermost and uppermost bands, and are characterized by a single Chern number. Due to the presence of particle-hole symmetry in the Harper Hamiltonian (see Appendix D for details) the distribution of Chern numbers around zero energy is symmetric.

2.3.3 Edge Spectrum and the Bulk–Boundary Correspondence Principle

Quantum Hall system is an insulating system in its bulk, however, at the same time there are states localized at the edges of the 2D sample that are carrying quantized current. The importance of the edge states in quantum Hall system was first pointed out by B. I. Halperin [60] and a topological meaning to these states was given by Y. Hatsugai [8, 61, 62]. Edge states appear in a geometry where the bulk is confined to a finite spatial area and therefore has a boundary. These are eigenstates of the system that have energy in a bulk gap and their wavefunction is extended along the entire spatial boundary. They are immune to backscattering and remain propagating even in the presence of arbitrary amount of disorder at the edge. This robustness is due to the topological nature of the insulating bulk: edge states persist as long as the bulk remain insulating. Their number is related to the Chern numbers of the bulk bands via the so called bulk–boundary correspondence principle.

To demonstrate the existence of edge states in the Harper problem, I consider a 2D lattice with periodic boundary conditions along the y axis and absorbing boundary condition along the x axis. The lattice in the x direction consists of $N \in \mathbb{Z}^+$ magnetic unit cells with total Nq lattice sites (so that the lattice size is commensurate with the flux ratio $\phi = p/q$). The sites of the lattice are labelled by j, i.e $j = 1, 2, \cdots, Nq$. At the two boundaries along the x direction, the tunneling amplitude is set to zero i.e $-\mathcal{J}\,\hat{c}^{\dagger}_{j-1,k_y}\,\hat{c}_{j,k_y} \rightarrow 0$ for $j = 1$ and $-\mathcal{J}\,\hat{c}^{\dagger}_{j+1,k_y}\,\hat{c}_{j,k_y} \rightarrow 0$ for $j = Nq$. In this configuration, the tight-binding Hamiltonian ($\hat{H}_{\text{edge}}$) can be written as

$$\hat{H}_{\text{edge}} = \frac{1}{(2\pi)} \int_{-\pi}^{+\pi} dk_y \otimes -\mathcal{J}\Bigg[\sum_{j=1}^{Nq-1} \hat{c}^{\dagger}_{j+1,ky}\,\hat{c}_{j,ky} + \sum_{j=2}^{Nq} \hat{c}^{\dagger}_{j-1,ky}\,\hat{c}_{j,ky} $$

$$+ 2\sum_{j=1}^{Nq} \cos(2\pi\phi j - k_y)\,\hat{c}^{\dagger}_{j,ky}\,\hat{c}_{j,ky} \Bigg] $$

$$= \frac{1}{(2\pi)} \int_{-\pi}^{+\pi} dk_y \otimes \hat{\mathcal{H}}_{\text{edge}}(k_y). \tag{2.40}$$

To compute the eigenspectrum of the matrix $\hat{\mathcal{H}}_{\text{edge}}(k_y)$, the procedure given in equations (2.32), (2.33)

---

[6] The bulk spectrum can be obtained either by considering an infinitely extended 2D lattice or a finite lattice with periodic boundary conditions in both x and y direction.
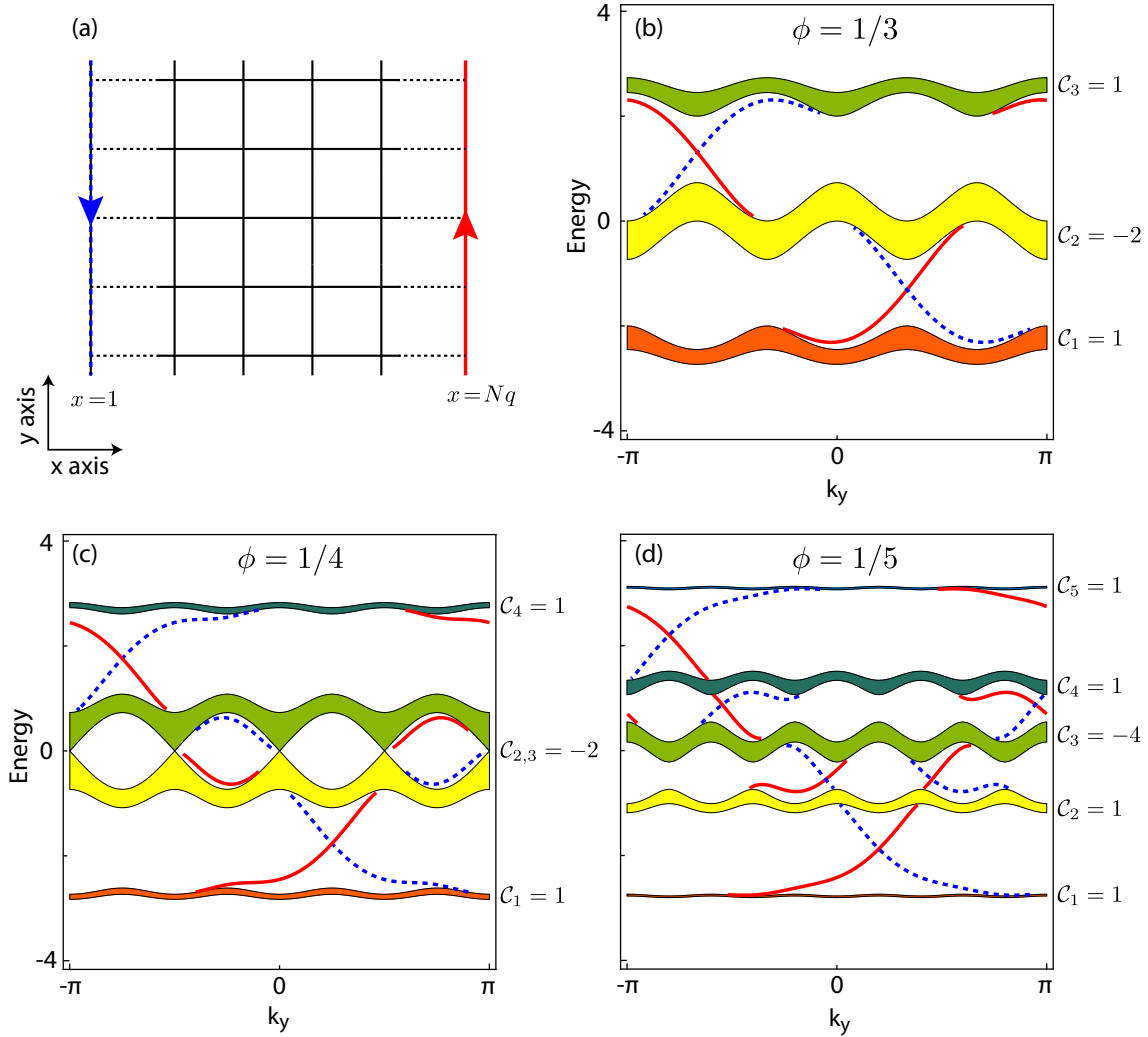
Figure 2.6: Energy spectrum of the 2D tight-binding model in the presence of a magnetic field on a 2D lattice with edges. (a) Schematic of the lattice geometry for the problem with periodic boundary condition along the y direction and two edges in the x direction (one at $x = 1$ and other at $x = Nq$). The configuration maintains translation invariance in the y direction and hence k_y is still a good quantum number. The energy spectrum for three different values of the flux ratio, i.e. (b) $\phi = 1/3$, (c) $\phi = 1/4$, and (d) $\phi = 1/5$ is shown. In each case, the regions filled with colors represent the bulk bands of the energy spectrum and the states propagating in the bulk gaps represent the edge spectrum. In each gap, there are two types of edge states, one is colored red (solid lines) and the other is blue (dashed lines). The states represented by red color (solid lines), are spatially localized on the right edge ($x = Nq$) and the blue (dashed lines) are on the left ($x = 1$) edge of the lattice. The net number of edge states (localized at a given edge and with counter propagating edge states counted with opposite sign) in a bulk gap is equal to the sum of the Chern numbers of all the bands below that gap which here is in agreement with the bulk–boundary correspondence principle. For each configuration (a), (b) and (c), the spectrum is numerically computed using $N = 30$ magnetic unit cells and $\mathcal{J} = 1$.

can be used. The eigenvalue problem reduces to a 1D problem similar to eq. (2.34) on an open chain,

$$ -\mathcal{J}\left(2\cos(2\pi\phi j - k_y)\, a_j + a_{j-1} + a_{j+1}\right) \;=\; E_{\text{edge}}(k_y)\, a_j. \tag{2.41} $$

In the presence of an edge along the x axis, the translation invariance in this direction is lost. However, the configuration maintains the translational invariance along the y axis and, hence, k_y is still a good quantum number. The eigenspectrum of this problem is numerically computed for three different values of the flux ratio, i.e. $\phi = 1/3, 1/4$ and $1/5$. The energy dispersion in these three configurations is shown in fig. 2.6. On top of the bulk bands (regions filled with colors), there are states with energies in the bulk gaps (solid and dashed colored lines). These are TP edge states, which are protected by the bulk gaps. These are branches of the dispersion relation consisting of eigenstates whose wavefunction is spatially concentrated near the boundary. The states, which are indicated by red color (solid lines), are those localized on the right boundary and the blue ones (dashed lines) are on left boundary of the lattice.

The Chern numbers of the bands are indicated at the right side of each configuration. According to the bulk–boundary correspondence principle, the net number of edge states in a bulk gap (localized at a given edge and with counter-propagating states counted with opposite sign) is equal to the sum of the Chern numbers of all the bands below that gap. The Chern number of a band is equal to the difference of the number of edge states (at a given edge) entering the band from below and leaving it above. The results (shown in fig. 2.6) are in accordance with the bulk–boundary correspondence principle.

Quantum Walks in 1D and 2D, and their Topological Properties

T HE notion of quantum walks was first introduced by Y. Aharonov et al. [63] as the quantum mechanical counterpart of a classical random walk (CRW). In a 1D CRW, a particle moves in discrete steps to either left or right depending on the outcome of a coin-toss with two mutually exclusive results. Mathematically, it is described in terms of transition probabilities. When the sequence of a coin-toss and subsequent position shifts are iterated for a large number of times, the probability distribution of a particle having equal probability of moving left or right results in a binomial distribution. The quantum mechanical analogue, i.e. QW, describes the motion of a quantum particle in space and time, where the quantum interference plays a major role. A QW is described by probability amplitudes and is a unitary process, i.e. the sum of amplitudes squared must be equal to 1. In general, this is accomplished by extending the Hilbert space by internal states which act as a coin degree of freedom. In contrast to tossing a real coin in a CRW, in a QW, a quantum particle is put in a coherent superposition of internal states at each step of the walk, which corresponds to a *coin operation*. Subsequently, the particle is shifted depending on its internal state, forming a *state-dependent shift operator*. Iterations of the coin and the state-dependent shift operation delocalize a quantum particle over multiple paths, where quantum interference between different paths leads to a radically different behavior than their classical analogue.

Since their first introduction, QWs have seen immense growth in interests due to their applications in quantum information science and in physics. In the field of quantum information, the interest in understanding QWs is to exploit their quantum mechanical behavior and develop efficient quantum algorithms on quantum computers [64, 65]. By exploiting the interference effects, the algorithms based on QWs can outperform their classical counterparts at some computational tasks [66, 67]. In physics, QWs are used as a dynamical tool for controlling the motion of quantum particles. Besides their applications in simulating and modeling a number of other physical phenomena, e.g. localization effects [68–70] and molecular states formation due to interactions between particles [71], they have been identified as a versatile platform for simulating topological phenomena. It was first shown by Kitagawa et al. that QWs can simulate all symmetry classes of the non-trivial topological phases in 1D and 2D for the case of non-interacting particles [72]. Being periodically driven quantum systems, however, QWs exhibit *Floquet topological phases* with much richer structure than those known for the static Hamiltonians. For instance, QWs allow the formation of new TP edge states, which cannot be explained with the invariants developed for the time-independent systems. A set of new topological invariants, both in 1D and 2D, are developed for their characterization [73–76].

In this chapter, I briefly introduce QWs and their topological properties, both in 1D and 2D. The objective is to highlight the TP edge states specific to periodically driven systems (QWs here) and the new topological invariants controlling their appearance and number. To introduce the notations and basic definitions in the next section, I start with the simple 1D QW in real space. Based on its temporal evolution in space, its difference from a CRW is demonstrated. I then introduce the momentum space representation and associated energy spectrum of QWs to study their topological properties.

3.1 Quantum Walks

3.1.1 Quantum Walks in Position Space

Let us consider a quantum particle (will be equally called a "walker") with two internal states (or spin states). These states are labelled by s with basis vectors $\{|s\rangle : s \in \{\uparrow, \downarrow\}\}$ spanning a 2D Hilbert space $\mathcal{H}^s$ ("coin space"). A particle in spin-up state is represented by $|\uparrow\rangle$ and in spin-down state by $|\downarrow\rangle$. In order to perform matrix operations, these basis states can be written as column vectors,

$$|\uparrow\rangle = \begin{pmatrix} 1 \\ 0 \end{pmatrix}, \quad |\downarrow\rangle = \begin{pmatrix} 0 \\ 1 \end{pmatrix}, \tag{3.1}$$

having orthonormality property $\langle s'|s \rangle = \delta_{s',s}$. The particle's spatial position is given by a 1D lattice with lattice constant of unit length. The coordinates of the lattice are labelled by integer numbers, i.e. $\boldsymbol{x} = x \in \mathbb{Z}$, with corresponding basis vectors $|x\rangle$ spanning a 1D Hilbert space $\mathcal{H}^x$. The position basis vectors are also orthonormal, i.e. $\langle x'|x \rangle = \delta_{x',x}$, where $|x\rangle$ represents a particle that is localized at position x. I start with a particle that is initially localized around $x = 0$ having internal state $|s\rangle$ which, in general, can be spin-up, spin-down or any superposition of these two states. The initial state ($\psi_{\text{init.}}$) of the walker can be written as

$$|\psi_{\text{init.}}\rangle = |0\rangle \otimes |s\rangle = |0, s\rangle\,^1, \tag{3.2}$$

which resides in the combined Hilbert space $\mathcal{H} = \mathcal{H}^x \otimes \mathcal{H}^s$. The tensor product ($\otimes$) combines the internal degrees of freedom and the spatial ones. Mathematically, a single step of the walk is given by the application of a unitary "walk operator" to the initial state. The simplest 1D walk operator can be written as the product of two unitary operators. One of them acts on the spin states only (I will henceforth call it a "coin operator") and the other acts on both (spin and position) states, which is known as a state-dependent shift operator (or simply a "shift operator").

Coin Operator: The coin operator $\hat{C}$ introduces a rotation of the spin state in the coin space $\mathcal{H}^s$. A spin state can be geometrically represented by a point on a Bloch sphere with a corresponding Bloch vector locates the position of this point. The coin operator results in a rotation of this vector. In general, a coin operator can depend on several parameters resulting in different QWs protocols [77, 78]. However, here and throughout this thesis, I will use a coin operator depending only on a single parameter [79], i.e.

$$\hat{C}(\theta) = \sum_x |x\rangle \langle x| \otimes e^{-i\frac{\theta\, \sigma_y}{2}} = \sum_x |x\rangle \langle x| \otimes \begin{pmatrix} \cos(\theta/2) & -\sin(\theta/2) \\ \sin(\theta/2) & \cos(\theta/2) \end{pmatrix}, \tag{3.3}$$

with σ_y being the 2nd Pauli matrix. The rotation angle $\theta \in [-2\pi, 2\pi[$ determines the amount of rotation of the spin state and couples the spatial degrees of freedom with the internal degrees of freedom[2] (this

---

[1] The second equation is used in favor of notational simplicity

[2] Due to our definition, $\hat{C}(\theta)$ has 4π periodicity in the rotation angle θ.
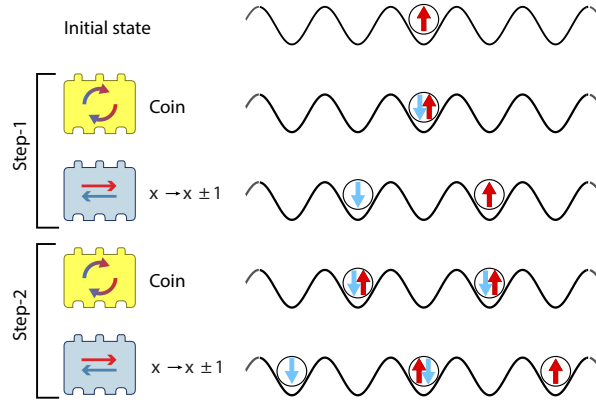
Figure 3.1: Schematic illustration of the simplest 1D QW with a particle initially prepared in a spin-up state. A coin operator with $\theta = \pi/2$ (Hadamard-like coin) transforms spin-up state into an equal superposition of the two spin states. The shift operator then shifts the spin-up state to the right and spin-down to the left by one lattice site. After two steps of the walk, the spin-up part of the wave function is shifted by two lattice sites to the right and the spin-down to the left. The information regarding the probability of a given spin state at a given lattice site is not schematized in this illustration.

coupling will become clear in the next section when the walk operator is transformed to Fourier space). In this definition of $\hat{C}(\theta)$, the rotation axis is chosen along the y axis of the Bloch sphere. However, any other choice of the rotation axis, that is lying in the equatorial plane of the Bloch sphere, is equivalent to this choice up to a unitary transformation of the spin basis. The coin angle is generally (as defined here) independent of the spatial coordinates, which makes the QW homogenous. However, for inhomogeneous QWs, the rotation angle can be position-dependent (this case will be shown later in this chapter). Here we consider a balanced coin by setting $\theta = \pi/2$, also called the Hadamard coin [80, 81],

$$\hat{C}(\pi/2) = \sum_x |x\rangle \langle x| \otimes e^{-i\frac{\pi}{2}\sigma_y} = \sum_x |x\rangle \langle x| \otimes \frac{1}{\sqrt{2}} \begin{pmatrix} 1 & -1 \\ 1 & 1 \end{pmatrix}. \tag{3.4}$$

This coin operator transforms each of the spin state into an equal superposition of the two spin states and therefore maximally mixes the two states, i.e.

$$\hat{C}(\pi/2) |0, \uparrow\rangle = \frac{1}{\sqrt{2}} (|0, \uparrow\rangle + |0, \downarrow\rangle),$$

$$\hat{C}(\pi/2) |0, \downarrow\rangle = \frac{1}{\sqrt{2}} (|0, \downarrow\rangle - |0, \uparrow\rangle). \tag{3.5}$$

This operator has close similarity with the classical balanced coin, which has equal probability of getting "heads" and "tails".

Shift Operator: The coin operator is followed by a shift operator $\hat{S}_x$. The shift operator acts on the combined Hilbert space $\mathcal{H}$ and coherently shifts a particle in $|\uparrow\rangle$ by one lattice site to the right and a

particle in $|\downarrow\rangle$ to the left. For the 1D QW, this shift operator is defined as

$$\hat{S}_x = \sum_x \left(|x+1\rangle\langle x| \otimes |\uparrow\rangle\langle\uparrow| + |x-1\rangle\langle x| \otimes |\downarrow\rangle\langle\downarrow| \right). \tag{3.6}$$

Walk Operator: A sequence of unitary operators constituting the walk operator is referred to the walk protocol. Here the coin operator and the shift operator combine to give the walk operator for a 1D Hadamard like-QW,

$$\hat{W}_{1D} = \hat{S}_x \hat{C}(\pi/2). \tag{3.7}$$

In QWs' literature, this walk operator is sometimes referred to as the 1D-standard protocol. The evolution of the walk results from the periodic application of the walk operator to the initial state of the walker. A schematic of the first two steps of this walk, for a particle initially prepared in a spin-up state, is shown in fig. 3.1. In the absence of decoherence, the final state $|\psi_n\rangle$ of a particle (after applying the walk operator n-times to the initial state eq. (3.2)) is a pure state, which can be written as a superposition of the spin and position basis states,

$$\begin{aligned}|\psi_n\rangle &= (\hat{W}_{1D})^n |\psi_{\text{init.}}\rangle = (\hat{S}_x \hat{C}(\pi/2))^n |\psi_{\text{init.}}\rangle \\ &= \sum_{x,s} c_{x,s} |x,s\rangle.\end{aligned} \tag{3.8}$$

The coefficients $c_{x,s} \in \mathbb{C}$ represent the complex amplitudes of the wavefunction for the particle at position x with spin state s. At each step of the walk, the wave function is evolved with the identical walk operator resulting in an identical evolution at each step. This makes the evolution of the wavefunction under a QW deterministic.

The probability (pr) of finding the particle at position x, after n steps of the walk, is obtained by projecting the state $|\psi_n\rangle$ to a state at position x and summing over both spin states, i.e.

$$\text{pr}_n(x) = \sum_s |\langle x, s|\psi_n\rangle|^2 = \sum_s |c_{x,s}|^2. \tag{3.9}$$

Projecting the final state to a state at a given position physically corresponds to performing measurement on the final state at that position. As a result the wave function collapses and the particle is found at position x with probability $\text{pr}_n(x)$.

The evolution of this walk for a large number of steps, i.e. $n = 100$, is shown in fig. 3.2. The walker starts at the origin ($x = 0$) of the 1D lattice, which we restrict to $2N + 1$ (with $N \in \mathbb{N}$) number of sites. I have plotted only non-zero probabilities, as after an even number of steps of the walk, the probability of the particle at lattice sites represented by odd integers is zero. For comparison, the evolution of a CRW (with a balanced coin) for the same number of walk steps is also shown. A striking difference is the nearly uniform spreading of the QW in the position interval $\left[-n/\sqrt{2},\ n/\sqrt{2}\right]$. Quantum interference suppress the arrival probabilities at the initial position and enhances the probabilities of moving away from it. In CRW, the probability distribution is binomial around the initial position, i.e. the probability of a particle around its initial position is maximal and decreases away from it [64, 80]. The shape of the probability distribution for a QW depends on the choice of the coin angle and on the initial state of the particle. Figure 3.2(a) shows that, for the Hadamard-like coin the probability distribution of a particle starting in an initial symmetric superposition of the two spin states is symmetric with respect to the initial position. On the other hand, fig. 3.2(b) shows that a particle initially prepared in a spin-up or spin-down state leads to asymmetric probability distribution.

The variance of the QW is proportional to the square of the number of steps, i.e. n^2, while the variance
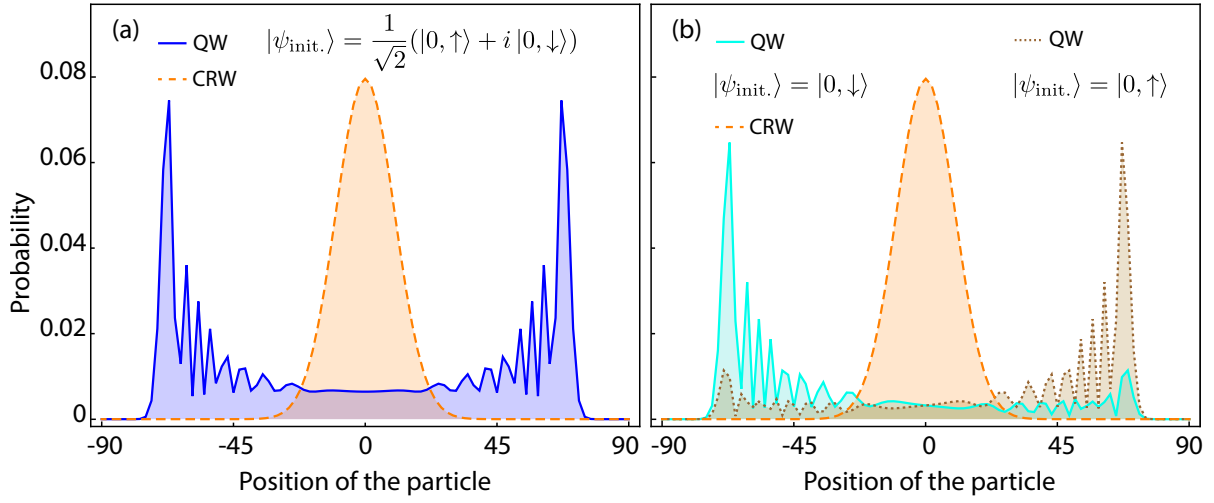
Figure 3.2: Probability distribution of a 1D Hadamard-like QW for $n = 100$. For comparison, the probability distribution of a CRW (with a balanced coin) is also shown. In both cases, a walker is initialized at the origin of a 1D lattice with N = 90. (a) The solid line represents the probability distribution of a Hadamard-like QW. Only non-zero probabilities of the particle are plotted, i.e. at the points represented by even integer numbers. The initial internal state of the particle is a symmetric superposition of the two spin states. The distribution given by the dashed line represents the probabilities of a classical particle after 100 steps of the CRW (only the non-zero probabilities are plotted). The limiting distribution of the CRW approaches a Gaussian distribution. A striking difference of the QW from the classical one is its nearly uniform spreading in the position interval $\left[-n/\sqrt{2}, n/\sqrt{2}\right]$. (b) The same comparison for a quantum particle starting in a spin-up (with the resulting probability distribution shown by dotted line) or spin-down configuration (solid line). The particle, which starts in spin-up state, drifts rightward and the one in spin-down state drifts leftward.

of the CRW just scales with $\sqrt{n}$. This means that in QWs, a particle reaches a given distant point quadratically faster (which is known as ballistic spreading) than their classical counter part (which spreads diffusively). This fast spreading of the QWs is useful for developing quantum search algorithms yielding speedups over the classical ones [82].

3.1.2 Quantum Walks in Momentum Space

For an infinitely extended lattice or a finite lattice with periodic boundary conditions, the walk operator, for a homogenous QWs, has discrete translational symmetry, i.e. it remains invariant under discrete translations of the lattice. In this case, a much simpler description of the walk can be given by representing the walk operator in quasimomentum space. As a result, the walk operator simply reduces to a 2×2 matrix which can be diagonalized easily to extract different information about the dynamics of the walk, e.g. energy dispersion, eigenstates and velocities of the walker. To represent the walk operator in quasimomentum space, it is required to carry out Fourier transformation for each individual unitary operator of the walk. The coin operator is diagonal in the quasimomentum basis (as it is in position basis) due to the fact that it does not depend on the spatial coordinates. The Fourier transformation to the quasimomentum space is given by

$$|k_x\rangle = \sum_x e^{ik_x x} |x\rangle, \quad k_x \in [-\pi, \pi[, \quad (3.10)$$

with the inverse Fourier transformation,

$$|x\rangle = \frac{1}{2\pi} \int_{-\pi}^{+\pi} dk_x e^{-ik_x x} |k_x\rangle. \tag{3.11}$$

Implementing these transformation to the shift operator (eq. (3.6)) we can write it in the quasimomentum space as

$$\sum_x |x+1\rangle \langle x| \otimes |\uparrow\rangle \langle \uparrow| = \frac{1}{2\pi} \int_{-\pi}^{+\pi} dk_x e^{-ik_x} |k_x\rangle \langle k_x| \otimes |\uparrow\rangle \langle \uparrow|,$$

$$\sum_x |x-1\rangle \langle x| \otimes |\downarrow\rangle \langle \downarrow| = \frac{1}{2\pi} \int_{-\pi}^{+\pi} dk_x e^{ik_x} |k_x\rangle \langle k_x| \otimes |\downarrow\rangle \langle \downarrow|,$$

$$\implies \hat{S}_x = \frac{1}{2\pi} \int_{-\pi}^{+\pi} dk_x |k_x\rangle \langle k_x| \otimes \left(e^{-ik_x} |\uparrow\rangle \langle \uparrow| + e^{ik_x} |\downarrow\rangle \langle \downarrow| \right). \tag{3.12}$$

The shift operator is diagonal in the k_x-basis and can be reduced to a 2×2 matrix in the spin basis for each value of k_x, i.e.

$$\begin{aligned} \hat{S}_x(k_x) &= \langle k_x|\hat{S}_x|k_x\rangle \\ &= e^{-ik_x} |\uparrow\rangle \langle \uparrow| + e^{ik_x} |\downarrow\rangle \langle \downarrow| \\ &= \begin{pmatrix} e^{-ik_x} & 0 \\ 0 & e^{ik_x} \end{pmatrix}. \end{aligned} \tag{3.13}$$

The coupling of the quasimomentum k_x to the spin states of the particle is evident. The shift operator therefore imprints a phase e^{-ik_x} on right-moving and a phase e^{ik_x} on left-moving particle. The walk operator (eq. (3.7)) with coin angle θ can therefore also be diagonalized in quasimomentum space as

$$\hat{W}_{1D} = \frac{1}{2\pi} \int_{-\pi}^{+\pi} dk_x |k_x\rangle \langle k_x| \otimes \hat{W}_{1D}(k_x),$$

with $\hat{W}_{1D}(k_x)$ given by:

$$\begin{aligned} \hat{W}_{1D}(k_x) &= \hat{S}_x(k_x)\hat{C}(\theta) \\ &= \begin{pmatrix} e^{-ik_x}\cos(\theta/2) & -e^{-ik_x}\sin(\theta/2) \\ e^{ik_x}\sin(\theta/2) & e^{ik_x}\cos(\theta/2) \end{pmatrix}, \end{aligned} \tag{3.14}$$

which acts on the spin states of the particle only. The off-diagonal elements of this operator measure the strength of the spin-orbit coupling (i.e. coupling of the internal degrees of freedom to the external ones), which is proportional to $\sin(\theta/2)$ [83]. This spin-orbit coupling is important for realizing topological phases with QWs [84].

3.1.3 Quasienergy Spectrum

In QWs, a walker is evolved by periodically applying the walk operator at discrete-time steps, i.e. the dynamics of the walker is periodic in time. Hence, a QW is an example of a periodically driven Floquet system. The evolution of a particle generated by the walk operator, at integer time steps, is equivalent to
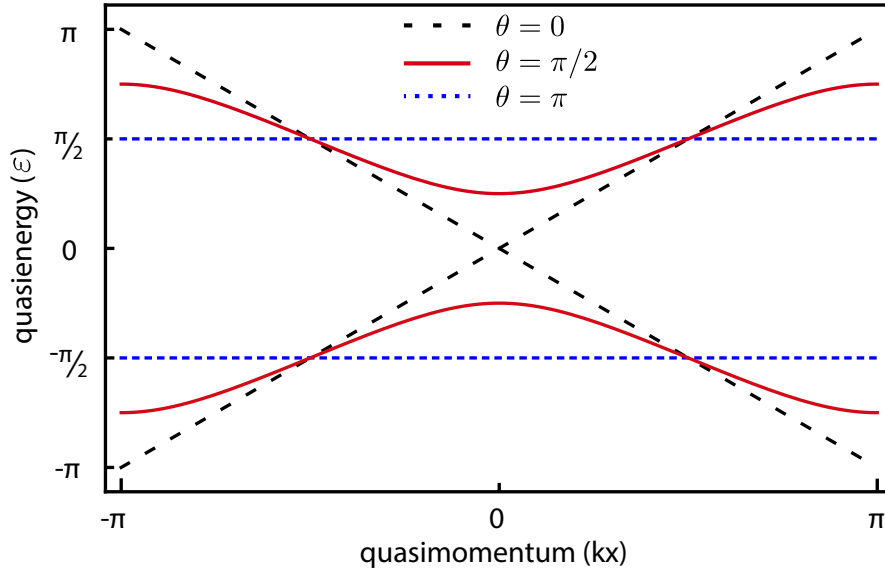
Figure 3.3: Quasienergy dispersion of the 1D QW for different values of the coin angle θ. Due to the periodicity of quasimomentum and quasienergy, π and $-\pi$ values of k_x and ε are identified. The dispersion consists of two bands due to the two spin states of the walker. For $\theta = 0$ (black dashed lines), the two bands are gapless having maximum slope for all values of k_x. In this case, the coin operator is an identity operator that does not change the spin state of the walker. In real space this implies that after each step of the walk the spin-up state of the walker shifts by one lattice site to the left and the spin-down to the right. For $\theta = \pi/2$ (red solid lines), the bands are gapped having zero slope at the centre and at the edges of the quasimomentum BZ. The coin angle $\theta = \pi$ corresponds to a spin flip process resulting in almost flat bands (blue dashed lines). The velocity of the walker is zero for all values of k_x and hence is localized in the lattice. For both $\theta = \pi/2$ and $\theta = \pi$, there are two gaps due to the periodicity of the quasienergy. One is at $\varepsilon = 0$ and the other is at $\varepsilon = \pi$.

the evolution under a time-independent effective Hamiltonian [84], i.e.

$$\hat{W}_{1D}(k_x) \equiv e^{-i\hat{H}_{\text{eff}}.T/\hbar}. \tag{3.15}$$

Here T is the time taken by a single step of the walk and $\hbar$ is the reduced Planck's constant. For simplicity, we set $T = 1$ and work with natural units where $\hbar = 1$. The walk operator (eq. (3.15)) is a unitary operator and its eigenvalues are complex numbers of the form $e^{-i\varepsilon}$ with unit modulus. The dimensionless parameter ε is known as the quasienergy. Similar to quasimomentum, which is defined in the presence of a discrete spatial translational symmetry, ε is a periodic variable defined in the presence of a discrete time translational symmetry[85]. It is uniquely defined in the interval $[-\pi, \pi[$, representing a quasienergy BZ similar to the quasimomentum case. This parameter can be written in physical units of energy by multiplying it with $\hbar/T$. It is important to mention at this point that like real energies in the case of static lattice Hamiltonians (for example, the one introduced in chap. 2), quasienergies can be organized into quasienergy bands [75]. These quasienergy bands can have interesting topological properties like the real energy bands, which we will show in this chapter.

The quasienergy ε and corresponding eigenvectors of the walk can be obtained by diagonalizing $\hat{W}_{1D}(k_x)$ (eq. (3.14)) for each value of k_x. From the quasienergy dispersion $\varepsilon(k_x)$, the dynamics of the walk can be directly explained, e.g. how fast a walker for a given value of the coin angle θ and quasimomentum k_x will spread in the lattice. Figure 3.3 shows the quasienergy dispersion of the 1D

standard protocol for three different values of the coin angle, i.e. $\theta = 0$, $\pi/2$ and π. Since the walker has two spin states, the quasienergy dispersion consists of two bands. For $\theta = 0$, the coin is an identity operator, which does not change the initial spin state of the walker. As a result, the walker travels like a classical particle with the maximum velocity of one lattice site per step of the walk (in QWs, this is the maximum velocity, similar to the velocity of light, a walker can travel with). This can be seen from the dispersion, where the two bands have slope equal to ± 1. For $\theta = \pi/2$, the quasienergy bands are gapped with zero slope at the centre and at the edges of the quasimomentum BZ. The quasienergy bands become flat for $\theta = \pi$ for which the coin operator acts as a spin-flip operator. As a result, the walker is localized in the lattice and the two bands are gapped maximally. In the case of gapped bands, due to the periodicity of the quasienergy, there exist two gaps: one is at $\varepsilon = 0$ and the other is at $\varepsilon = \pi$ ($\varepsilon = \pi$ and $\varepsilon = -\pi$ are identified). The band gap at $\varepsilon = \pi$ (also known as Floquet gap) is a unique property of the Floquet topological systems.

3.2 Topological Properties of Quantum Walks

3.2.1 Discrete Symmetries

The quasienergy bands, besides giving deeper insight into the walk evolution and its characteristics, can also provide insight to the topological properties similar to the gapped lattice Hamiltonians in static systems (chap. 2). For a static system described by a single-particle gapped Hamiltonian, the class of a topological phase, besides the dimensionality, depends on three main symmetries: time-reversal symmetry (TRS), particle–hole symmetry (PHS), and chiral symmetry (CS) [86]. These symmetries are used for the classification of topological insulators and superconductors, which gives ten possible symmetry classes represented by Cartan labels [87]. Different topological phases within a symmetry class are characterized by topological invariants, which are discrete numbers (either an integer $\mathbb{Z}$ or a binary quantity $\mathbb{Z}_2$). In the case of a QW, the class of a topological phase depends on the dimensionality and symmetries of the effective Hamiltonian $\hat{H}_{\text{eff.}}$ (associated with the walk operator) . In the following, I briefly introduce the constraints imposed by the presence of TRS, PHS, or CS symmetry on a walk operator ($\hat{W}$) and on the corresponding effective Hamiltonian ($\hat{H}_{\text{eff.}}$).

Time-reversal Symmetry: A walk operator $\hat{W}$ is invariant under TRS if there exists an anti-unitary operator $\mathcal{T} = K U_T$, which satisfies the property,

$$\mathcal{T}\hat{W}\mathcal{T}^{-1} = \hat{W}^{-1} \quad \Leftrightarrow \quad \mathcal{T}\hat{H}_{\text{eff.}}\mathcal{T}^{-1} = \hat{H}_{\text{eff.}}, \tag{3.16}$$

with a complex conjugation K acting on the complete Hilbert space of the protocol and a unitary operator U_T acting only on the internal states. The term "time reversal" comes from the fact that the time evolution operator $\hat{W}$ transfroms to its inverse under $\mathcal{T}$.

Particle–Hole Symmetry: A walk operator $\hat{W}$ is invariant under PHS if there exist an anti-unitary operator $\mathcal{P} = K U_P$, which satisfies the property,

$$\mathcal{P}\hat{W}\mathcal{P}^{-1} = \hat{W} \quad \Leftrightarrow \quad \mathcal{P}\hat{H}_{\text{eff.}}\mathcal{P}^{-1} = -\hat{H}_{\text{eff.}}. \tag{3.17}$$

This kind of symmetry exists in superconductors, that is why this symmetry is referred to PHS. As a result, the quasienergies come in pairs, i.e. for each eigenstate $|\psi\rangle$ of $\hat{H}_{\text{eff.}}$ with quasienergy ε there exists another state $\mathcal{P}|\psi\rangle$ with quasienergy $-\varepsilon$. Those states which are their own particle–hole symmetric

$\mathcal{T}^2$ \ $\mathcal{P}^2$	$+1$	-1	$\times$
$+1$	$\Gamma : \checkmark$ $\mathbb{Z} \times \mathbb{Z}$		
-1	$\Gamma : \checkmark$ $\mathbb{Z}_2 \times \mathbb{Z}_2$	$\Gamma : \checkmark$ $\mathbb{Z} \times \mathbb{Z}$	
$\times$	$\Gamma : \times$ $\mathbb{Z}_2 \times \mathbb{Z}_2$		$\Gamma : \checkmark$ $\mathbb{Z} \times \mathbb{Z}$

Figure 3.4: Symmetry classes of the non-trivial topological phases in 1D QWs with gapped quasienergy spectrum. The presence of TRS and PHS is indicated by (+1) or (−1) depending on whether $\mathcal{T}^2$ ($\mathcal{P}^2$) is +1 or −1. The absence of these symmetries is marked by (×). The existence of the extra symmetry (CS) is indicated by ($\Gamma : \checkmark$) and its absence is indicated by ($\Gamma : \times$) in five out of nine symmetry classes. These five topological phases are fully characterized by topological invariants $\mathbb{Z} \times \mathbb{Z}$ or $\mathbb{Z}_2 \times \mathbb{Z}_2$, giving the invariants at $\varepsilon = 0$ and $\varepsilon = \pi$. In the absence of TRS and PHS, the presence of CS results in an extra class of non-trivial topological phases, making total ten symmetry classes.

partners, i.e. $\mathcal{P} |\psi\rangle = |\psi\rangle$ and hence with $\varepsilon = -\varepsilon$, are of interest. If these states are separated from the bulk states by a gap, their energies cannot be changed by smooth deformations in the system parameters, unless the PHS is broken.

Chiral Symmetry: If there exists a unitary operator Γ which satisfies the property

$$\Gamma \hat{W} \Gamma^{-1} = \hat{W}^{-1} \iff \Gamma \hat{H}_{\text{eff.}} \Gamma^{-1} = -\hat{H}_{\text{eff.}}, \tag{3.18}$$

this is then referred to CS. In this case time reversal is achieved through a unitary operator which is CS. Due to this fact, CS is also known as a unitary TRS. As a result of CS, quasienergies come in pairs, i.e. for each eigenstate $|\psi\rangle$ of $\hat{H}_{\text{eff.}}$ with quasienergy ε, there exist another state $\Gamma |\psi\rangle$ with quasienergy $-\varepsilon$. Similar to the case of PHS, those states which are their own chiral symmetric partners, i.e. $\Gamma |\psi\rangle = |\psi\rangle$ with $\varepsilon = -\varepsilon$, can have topological protection.

These symmetries give ten possible symmetry classification of topological insulators. There are three possibilities for TRS, i.e. it can be absent ($\mathcal{T}^2 : \times$) or present with $\mathcal{T}^2 = \pm 1$. Similarly for PHS, it is either absent ($\mathcal{P}^2 : \times$) or present with ($\mathcal{P}^2 = \pm 1$). This gives total 9 symmetry classes. The product of TRS and PHS is related to CS, i.e. $\Gamma = \mathcal{T} \cdot \mathcal{P}$, which means that CS is present ($\Gamma : \checkmark$) when both symmetries are present. In the absence of both TRS and PHS, CS can be either absent ($\Gamma : \times$) or present ($\Gamma : \checkmark$). The presence of CS in the absence of TRS and PHS gives the tenth symmetry class. Based on these definitions, five out of ten symmetry classes of 1D QWs and their respective topological invariants are shown in fig. 3.4. The topological invariants come in pairs, i.e. $\mathbb{Z} \times \mathbb{Z}$ or $\mathbb{Z}_2 \times \mathbb{Z}_2$, which control the number of edge states at $\varepsilon = 0$ and at $\varepsilon = \pi$.

3.2.2 Topological Phases of 1D Quantum Walks

In order to introduce topological properties of 1D QW, I consider the simple example of the so called split-step walk protocol whose topological properties have been extensively studied [72, 74, 88–91]. This protocol is defined as

$$\hat{W}_{\text{1DSS}} = \hat{S}_x^{\downarrow} \hat{C}(\theta_2) \hat{S}_x^{\uparrow} \hat{C}(\theta_1), \tag{3.19}$$

where $\hat{S}_x^{\uparrow}$ $(\hat{S}_x^{\downarrow})$ shifts only spin-up (spin-down) part of the wave function to the right (left) leaving the other part unchanged. These shift operators can be written as

$$\hat{S}_x^{\uparrow} = \sum_x \left(|x+1\rangle \langle x| \otimes |\uparrow\rangle \langle\uparrow| + |x\rangle \langle x| \otimes |\downarrow\rangle \langle\downarrow| \right),$$

$$\hat{S}_x^{\downarrow} = \sum_x \left(|x\rangle \langle x| \otimes |\uparrow\rangle \langle\uparrow| + |x-1\rangle \langle x| \otimes |\downarrow\rangle \langle\downarrow| \right). \tag{3.20}$$

The coin operator $\hat{C}(\theta_i)$ (for $i \in \{1, 2\}$) is given by eq. (3.3). For the walk operator (eq. (3.19)), non-trivial topological phases are conditioned to the existence of a discrete symmetry, e.g. CS. At first glance the effective Hamiltonian associated to this walk has no CS. The symmetry however becomes apparent when the walk operator is written in the chiral-symmetric time frames: a notion introduced by J. k. Asbóth and H. Obuse [74]. A walk operator has CS, if a time frame can be found where its effective Hamiltonian has CS. By choosing the origin of the time frame in such a way that the sequence of the unitary operations, constituting the walk operator, has an inversion point. The walk operator eq. (3.19), in a shifted time frame has indeed such an inversion point (as shown in fig. 3.5), where the effective Hamiltonian has CS with $\Gamma = \sigma_x$ (here σ_x is the 1st Pauli matrix). In the shifted time frame of a single step of the walk, the sequence of unitary operators coming just before (earlier in time) and just after (later in time) the inversion point gives two operators

$$\hat{U}_1 = \hat{C}(\theta_2/2)\hat{S}_x^{\uparrow}\hat{C}(\theta_1/2), \tag{3.21}$$

$$\hat{U}_2 = \hat{C}(\theta_1/2)\hat{S}_x^{\downarrow}\hat{C}(\theta_2/2). \tag{3.22}$$

The combination of these provides us with two independent chiral-symmetric time frames; time frames where the walk operators and the associated effective Hamiltonians have CS,

$$\hat{W}'_{\text{1DSS}} = \hat{U}_2\hat{U}_1 = \hat{C}(\theta_1/2)\hat{S}_x^{\downarrow}\hat{C}(\theta_2)\hat{S}_x^{\uparrow}\hat{C}(\theta_1/2), \tag{3.23}$$

$$\hat{W}''_{\text{1DSS}} = \hat{U}_1\hat{U}_2 = \hat{C}(\theta_2/2)\hat{S}_x^{\uparrow}\hat{C}(\theta_1)\hat{S}_x^{\downarrow}\hat{C}(\theta_2/2). \tag{3.24}$$

Using $\hat{U}_2 = \sigma_x\hat{U}_1^{-1}\sigma_x$ and $\sigma_x\hat{U}_1\sigma_x\hat{U}_2 = 1$ for $\sigma_x\hat{S}_x^{\uparrow}\sigma_x = (\hat{S}_x^{\downarrow})^{-1}$ and $\sigma_x\hat{C}(\theta)\sigma_x = \hat{C}^{-1}(\theta) = \hat{C}(-\theta)$, it is easy to show that CS is present, i.e. $\sigma_x\hat{W}'_{\text{1DSS}}\sigma_x = (\hat{W}'_{\text{1DSS}})^{-1}$ and $\sigma_x\hat{W}''_{\text{1DSS}}\sigma_x = (\hat{W}''_{\text{1DSS}})^{-1}$. It is worth mentioning that changing the time frame of a walk corresponds to a unitary transformation on the walk operator, which does not change the quasienergy spectrum; although it is crucial for investigating the symmetries and topological properties.

A chiral symmetric effective Hamiltonian has a symmetric quasienergy spectrum with respect to the zero quasienergy, i.e. each stationary state of the effective Hamiltonian with quasienergy ε has a chiral-symmetric partner eigenstate with quasienergy $-\varepsilon$. There can exist states with $\varepsilon = -\varepsilon$, which are their own symmetry partners. If these states are separated from the bulk states by a gap, they cannot be removed from $\varepsilon = -\varepsilon$ by continuos perturbations, unless CS is broken. We will demonstrate later in this section that in the split-step QWs (in the presence of a boundary, separating two distinct topological domains), edge states can appear with both $\varepsilon = 0$ and $\varepsilon = \pi$. Both of these states satisfy the condition
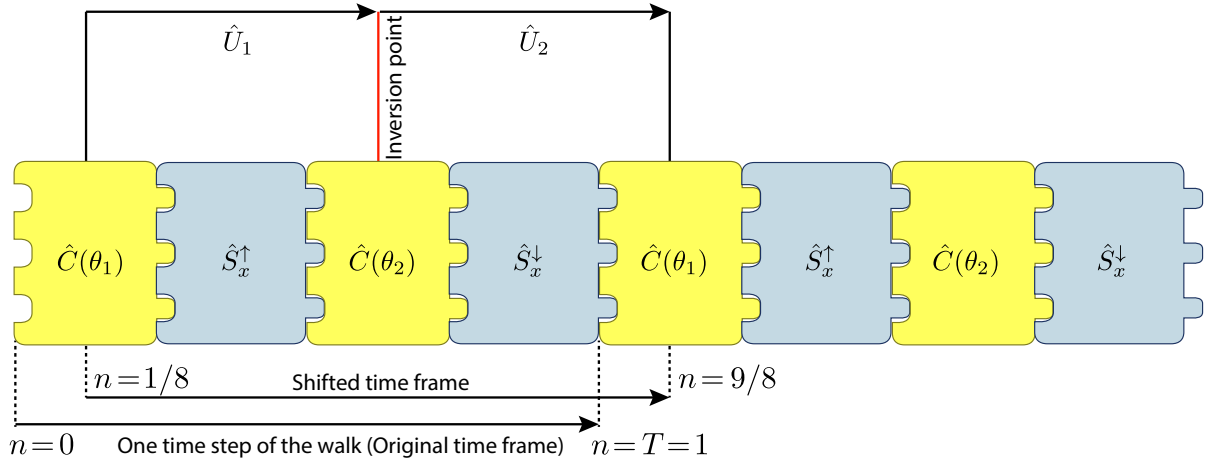
Figure 3.5: Schematic illustration of the notion of the time frames in the 1D split-step QWs. The sequence of unitary operators shown constitutes two time steps of the walk. A single step consists of four operators (two coins and two shifts), each have time duration of $n = 1/4$ (for the time period of a single step $T = 1$). The original time frame of the walk operator (eq. (3.19)) is from $n = 0$ to $n = T = 1$ and the shifted time frame is from $n = 1/8$ to $n = 9/8$. The inversion point of the walk operator (in the shifted time frame) is shown by a red line. In the time interval from $n = 1/8$ to $n = 9/8$, the sequence of operators coming just before (earlier in time) and just after (later in time) the inversion point, gives two operators $\hat{U}_1$ and $\hat{U}_2$. The combination of these provides us with two independent chiral-symmetric time frames.

$\varepsilon = -\varepsilon$ and are protected by CS. The corresponding bulk phases are characterized by a pair of topological invariants, controlling the number of edge states at $\varepsilon = 0$ and $\varepsilon = \pi$. The edge states at $\varepsilon = 0$ are well known from topological insulators described by time-independent lattice Hamiltonians, however, the edge (surface) states at $\varepsilon = \pi$ are unique to periodically driven systems. The existence of these states enrich the physics of Floquet topological insulators compared to the time-independent ones.

The bulk topological invariants of the 1D split-step walk (eq. (3.19)) are obtained from the winding numbers (ν', ν'') associated with the chiral symmetric bulk effective Hamiltonians ($\hat{H}'_{\text{eff.}}(k_x) = i \ln \hat{W}'_{\text{1DSS}}$, $\hat{H}''_{\text{eff.}}(k_x) = i \ln \hat{W}''_{\text{1DSS}}$). To obtain the winding number ν' (ν''), the effective Hamiltonian $\hat{H}'_{\text{eff.}}(k_x)$ ($\hat{H}''_{\text{eff.}}(k_x)$) is transformed to chiral basis: the basis where $\hat{\Gamma}$ is diagonal (see Appendix E for such transformation) and $\hat{H}'_{\text{eff.}}(k_x)$ ($\hat{H}''_{\text{eff.}}(k_x)$) is off-diagonal with upper block element $h'(k_x)$ ($h''(k_x)$),

$$\hat{H}'_{\text{eff.}}(k_x) = \begin{pmatrix} 0 & h'(k_x) \\ h'(k_x)^\dagger & 0 \end{pmatrix}; \quad \hat{H}''_{\text{eff.}}(k_x) = \begin{pmatrix} 0 & h''(k_x) \\ h''(k_x)^\dagger & 0 \end{pmatrix}. \quad (3.25)$$

The winding number associated with $\hat{H}'_{\text{eff.}}(k_x)$ is determined from the upper off-diagonal element $h'(k_x)$ in the following way,

$$\nu' = \frac{1}{2\pi i} \int_{-\pi}^{\pi} dk_x \frac{d}{dk_x} \ln \det h'(k_x). \quad (3.26)$$

The winding number ν'' for $\hat{H}''_{\text{eff.}}(k_x)$ can be obtained analogously. Geometrically, ν' and ν'' can be represented as the winding of the eigenspinors $\hat{n}'(k_x)$ and $\hat{n}''(k_x)$ on the Bloch sphere. These $(\hat{n}'(k_x), \hat{n}''(k_x))$ can be determined from the translational invariant bulk effective Hamiltonians ($\hat{H}'_{\text{eff.}}(k_x) =$
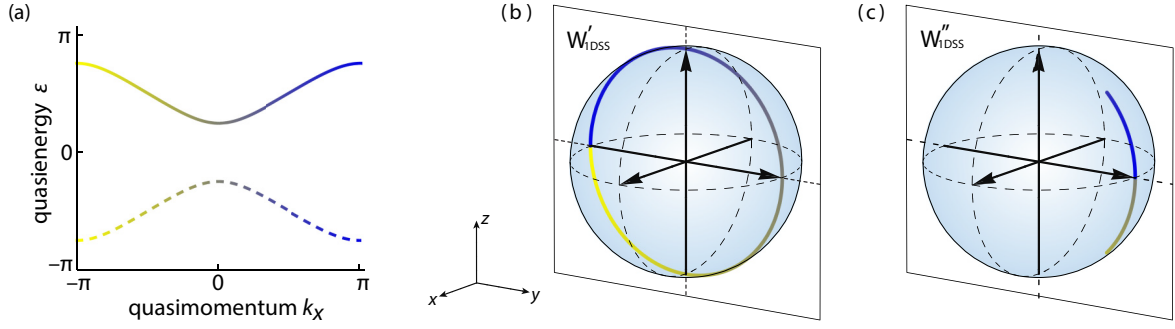
Figure 3.6: Quasienergy spectrum and topological winding of the 1D split-step protocol with ($\theta_1 = \pi/2$, $\theta_2 = 0$) (Hadamard walk). (a) Quasienergy spectrum consists of two bands, which are separated by finite quasienergy gaps at $\varepsilon = 0$ and $\varepsilon = \pi$. (b) Winding of the eigenspinor corresponding to the upper band represented on the Bloch sphere (for $\hat{W}'_{1DSS}$). The presence of CS, restricts the eigenspinors to a plane ($x = 0$) passing through the origin of the Bloch sphere. By sweeping the quasimomentum k_x through the BZ (indicated by the color gradient from yellow to blue), the eigenspinor traces a closed loop on the surface of the Bloch sphere (same color gradient is used to match the corresponding quasimomentum). The (signed) winding number is $\nu' = 1$. (c) Winding of the eigenspinor in the second chiral-symmetric time frame ($\hat{W}''_{1DSS}$). The (signed) winding number (ν'') is 0 in this case. This figure is adapted from [91].

$\varepsilon'(k_x)\hat{n}'(k_x) \cdot \vec{\sigma}$, $\hat{H}''_{\text{eff.}}(k_x) = \varepsilon''(k_x)\hat{n}''(k_x) \cdot \vec{\sigma})$[3]. The presence of CS restricts the eigenspinor (with $\varepsilon \neq 0$, π)[4] to a single plane passing through the origin of the Bloch sphere (in this case, the plane is $x = 0$). By sweeping the quasimomentum k_x through the BZ, the eigenspinor rotates around the origin of the Bloch sphere in the single plane, tracing a closed trajectory. The (signed) number of times an eigenspinor rotates around the origin is the winding numbers associated with the bulk effective Hamiltonian. The quasienergy spectrum of the 1D QW with the split-step protocol and the rotation of the eigenspinors in the two chiral-symmetric time frames are shown in fig. 3.6.

The winding number ν' or ν'' alone do not directly give the number of edge states (see sec. 3.2.3 for edge spectrum). These numbers (ν' and ν'') are obtained from the bulk effective Hamiltonians which, in general, do not provide full information on the walker's state at intermediate times of a single step of the walk. The bulk topological invariants (ν_0, ν_π), which determine the number of edge states at ($\varepsilon = 0$, π), are obtained by combining the information in the two chiral-symmetric time frames (for details, we refer the readers to [74]), i.e.

$$(\nu_0, \nu_\pi) = \left(\frac{\nu' + \nu''}{2}, \frac{\nu' - \nu''}{2}\right) + 1/2. \tag{3.28}$$

The invariant ν_0 (ν_π) counts the minimal number of times the band gap closes at $\varepsilon = 0$ ($\varepsilon = \pi$) during a continous transformation from one topological phase to another. Their values depend on the coin angles (θ_1 and θ_2). A range of values of θ_1 and θ_2, for which the bulk gaps remain open, defines a single

---

[3] Since $\hat{H}'_{\text{eff.}}(k_x)$ is a 2×2 matrix and can be expressed in terms of Pauli matrices $\sigma = \{\sigma_x, \sigma_y, \sigma_z\}$, i.e.

$$\begin{aligned} \hat{H}'_{\text{eff.}}(k_x) &= \vec{n}'(k_x) \cdot \vec{\sigma} \\ &= |\vec{n}'(k_x)| \, \hat{n}'(k_x) \cdot \vec{\sigma} \\ &= \varepsilon'(k_x) \, \hat{n}'(k_x) \cdot \vec{\sigma}. \end{aligned} \tag{3.27}$$

Here $|\hat{n}'(k_x)| = 1$ and $|\vec{n}'(k_x)| = \varepsilon'$. Same is the relation between $\hat{H}''_{\text{eff.}}(k_x)$ and $\hat{n}''(k_x)$.

[4] $\varepsilon = 0$, π are gap-closing points at which eigenspinors $\hat{n}'(k_x)$ and $\hat{n}''(k_x)$ become ill-defined
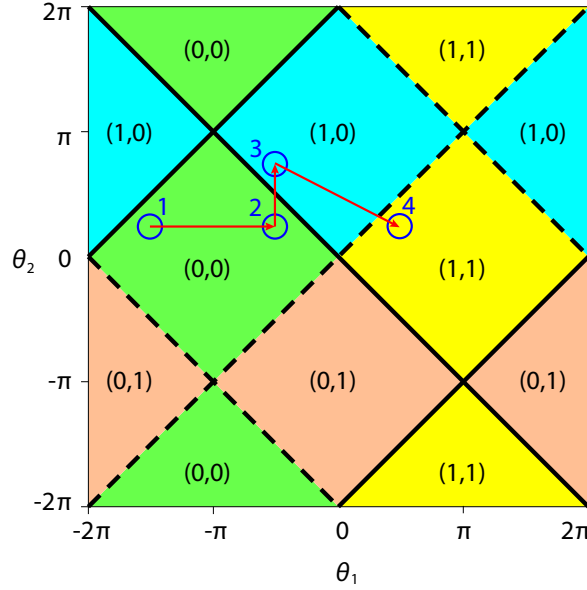
Figure 3.7: Topological phase diagram of the 1D split-step QW. Different gapped topological phases are indexed by the bulk topological invariants (ν_0, ν_π) and are separated by phase boundaries. The quasienergy gap closes at $\varepsilon = 0$ (solid) and $\varepsilon = \pi$ (dashed) at the phase boundaries. Due to our definition of the coin operator (eq. (3.3)), the walk has 4π periodicity in both coin angles. The circles, marked with 1, 2, 3 and 4, are the four pairs of coin angles used for implementing inhomogeneous QWs (see sec. 3.2.3) in order to demonstrate the existence of TP edge states. This figure is adapted from [91].

topological phase. Other phases, characterized by different bulk invariants, are separated by gap-closing points. By changing θ_1 and θ_2 through its complete period, different topological phases can be realized as shown in fig. 3.7. At a phase boundary, the bulk gap closes at $\varepsilon = 0$ or $\varepsilon = \pi$.

3.2.3 Topologically-protected Edge States: Physical Manifestation of the Non-trivial Topology of the Bulk

The physical manifestation of the non-trivial topology of the bulk phases is the existence of TP edge states at a boundary separating two different topological domains. In 1D, the energy of these states is pinned to the middle of the gaps and remain spatially localized at the phase boundaries. To demonstrate the existence of TP edge states, I consider spatially inhomogeneous 1D QWs with the coin angle depending on the spatial coordinates, i.e. $\theta = \theta(x)$. This breaks the translation invariance of the problem, however, this does not break the CS due to the fact that this symmetry acts only locally. In this situation, topological invariants can change only by closing a bulk gap. It is clear from the phase digram (fig. 3.7) that an inhomogeneous QW defined inside a single phase does not manifest edge states, as the bulk gaps remain open. Edge states can occur when the coin angles are varied from one topological phase to another, both having different topological invariants. At the phase boundary (where the bulk gap closes) the topological invariants become ill-defined and change values when transition to another phase takes place. According to the bulk–boundary correspondence principle, the minimum number of edge states at a phase boundary is equal to the absolute value of the algebraic difference of the topological invariants of the two phases.

Let us consider a 1D lattice which consist of $2N + 1$ lattice sites with periodic boundary conditions. The lattice is split into two regions (as illustrated in fig. 3.8(a)): a left region ($x << 0$) with pair of coin
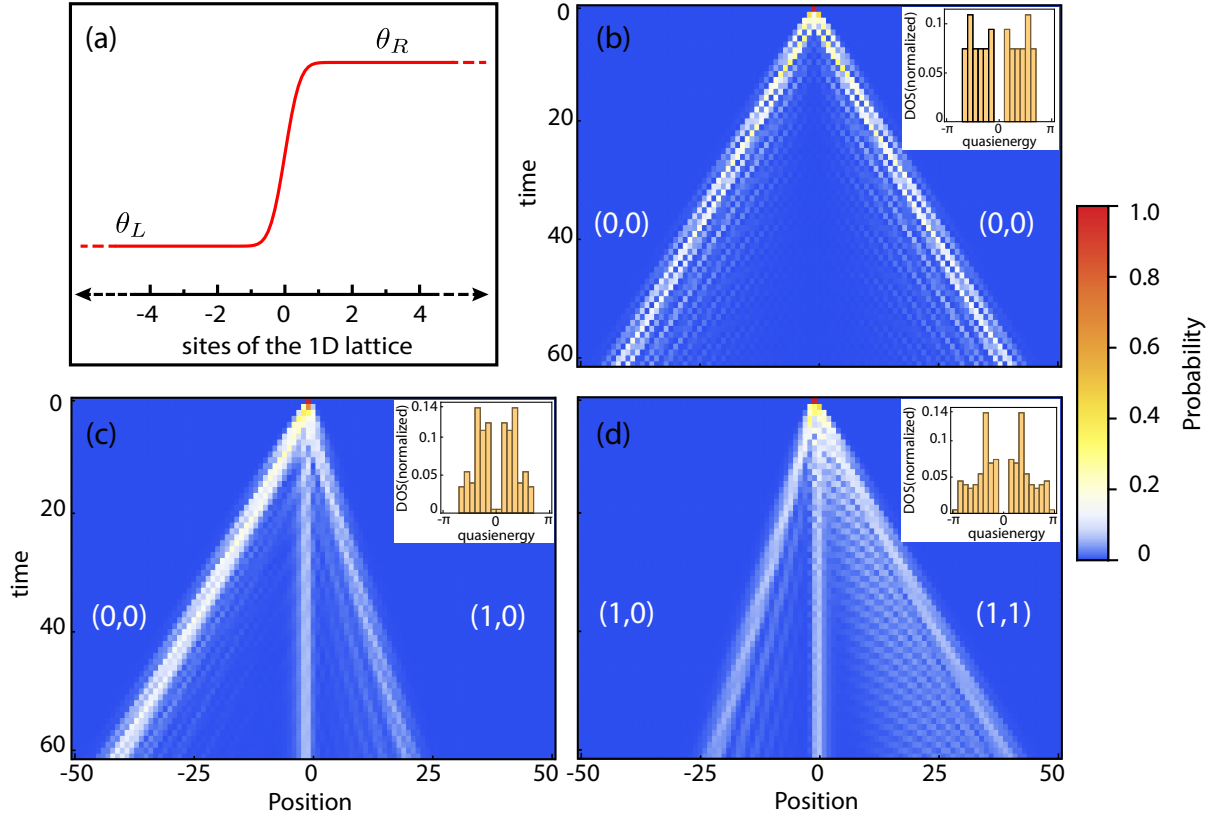
Figure 3.8: Inhomogeneous 1D QW demonstrating the existence of TP edge states at the interface of two different topological phases. (a) Schematic of the 1D lattice that consist of two regions: left ($x \ll 0$) with coin angles θ_L, and right ($x \gg 0$) with coin angles θ_R with smooth transition between the two takes place in the centre of the lattice. (b) The probability distribution of a walker in position-time plane, which is initialized at the centre of the 1D lattice. The coin angles in the left ($\theta_L^{(1)}$: (θ_{1L}, θ_{2L})) and in the right ($\theta_R^{(1)}$: (θ_{1R}, θ_{2R})) regions belong to the same phase as indicated by the arrow going from point 1 to 2 in the phase diagram (fig. 3.7). The bands remain open while going from point 1 to 2 and hence no edge state exist, as expected. (c) While going from point 2 to 3 (shown in the phase diagram fig. 3.7), the band gap closes at $\varepsilon = 0$ and hence a TP edge state with $\varepsilon = 0$ exists, which is localized around the centre of the lattice (transition region between two phases). (d) The band gap closes at $\varepsilon = \pi$ while going from point 3 to 4 and a TP edge state with $\varepsilon = \pi$ exist at the phase boundary. The insets show the normalized DOS which also indicate no edge state in (b), edge states at $\varepsilon = 0$ in (c), and edge states at $\varepsilon = \pi$ in (d). The pair of integers (ν_0, ν_π), in the left and right of (b)-(d) indicate the topological invariants of the respective phases. The difference of the topological invariants of the two bulks, for a given quasienergy, gives the number of edge states at that energy.

angles $\theta_\text{L} : (\theta_{1\text{L}}, \theta_{2\text{L}})$ and a right region ($x \gg 0$) with $\theta_\text{R} : (\theta_{1\text{R}}, \theta_{2\text{R}})$. The transition between the two regions takes place closed to the origin of the lattice ($x \approx 0$)[5]. I consider four different pairs of coin angles (as shown in fig. 3.7) for realizing three different configurations of inhomogeneous QWs with different edge spectra. The first two pairs of the coin angles (denoted by $\theta_{\text{L,R}}^{(1)}$) correspond to going from point 1 to 2 in the phase diagram,

$$1 \; \rightarrow \; 2 : \quad \theta_{\text{L,R}}^{(1)} = \begin{cases} (-3\pi/2, \pi/4) & \text{if } x \ll 0 \\ (-\pi/2, \pi/4) & \text{if } x \gg 0, \end{cases} \tag{3.29}$$

with left and right region have same topological invariants, i.e. $(0, 0)$. The quasienergy spectrum remains gapped during transition from left to right region of the lattice and hence no TP edge states are expected to exist. The second two pairs of coin angles ($\theta_{\text{L,R}}^{(2)}$), for making the transition from point 2 to 3, consist of

$$2 \; \rightarrow \; 3 : \quad \theta_{\text{L,R}}^{(2)} = \begin{cases} (-\pi/2, \pi/4) & \text{if } x \ll 0 \\ (-\pi/2, 3\pi/4) & \text{if } x \gg 0, \end{cases} \tag{3.30}$$

where the first pair of the coin angles realizes a topological phase with topological invariants $(0, 0)$ and the second one realizes a phase with invariants $(1, 0)$. Thus the quasienergy gap closes at the phase boundary at $\varepsilon = 0$ and hence a TP edge state with $\varepsilon = 0$ is expected to exist. The third two pairs of the coin angles ($\theta_{\text{L,R}}^{(3)}$), for making the transition from point 3 to 4, consists of

$$3 \; \rightarrow \; 4 : \quad \theta_{\text{L,R}}^{(3)} = \begin{cases} (-\pi/2, 3\pi/4) & \text{if } x \ll 0 \\ (\pi/2, \pi/4) & \text{if } x \gg 0, \end{cases} \tag{3.31}$$

which corresponds to joining two different topological phases with topological invariants $(1, 0)$ and $(1, 1)$. The quasienergy gap closes at $\varepsilon = \pi$ while going from point 3 to 4 and hence a TP edge state is expected to exist with $\varepsilon = \pi$. In all three cases, the crossover between the two regions is smooth, approximately over two lattice sites, instead of a sharp transition. This corresponds to the realistic conditions of the experiments with cold neutral atoms where the optical resolution of the imaging system puts limit on the sharpness of the crossover (for details, see [91]).

In all three configurations, the time evolution of a walker is investigated. The walker is initialized at the centre of the lattice with initial state $|\psi_\text{init.}\rangle = (|0, \uparrow\rangle + i |0, \downarrow\rangle)/\sqrt{2}$. One of the important property of the TP edge states is that they remain exponentially localized to the boundary between two distinct topological domains. Owing to this fact, the initial state of walker will have a non-zero overlap with the edge state (≈ 0.1 for the cases considered here). In this case, the probability for the walker to remain trapped at the boundary, after a large number of steps of the walk, is significant (≈ 0.15, after $n = 60$). In fig. 3.8, the time evolution ($\hat{W}_\text{1DSS}^n |\psi_\text{init.}\rangle$) of the walker is shown by plotting the probability $\text{pr}_n(x)$ of the walker in position-time plane. The numerical computations are carried out with $N = 50$ and $n = 60$. For the first configuration ($1 \rightarrow 2$), fig. 3.8(b) shows that the probability of the walker to remain close to the transition region is negligibly small and hence their is no TP edge state. On the other hand, in the second and third configurations ($2 \rightarrow 3$ and $3 \rightarrow 4$), fig. 3.8(c) and 3.8(d) show that the walker has significant probability of remaining trapped in the vicinity of the boundary, which show the existence of TP edge states. In the insets the numerically computed density of states (DOS), normalized to the total number of states, of the walk are shown, confirming the theoretically expected results for each configuration.

---

[5] Due to periodic boundary conditions, there are two, instead of one, boundaries. The second boundary is at $x = -N$ where the TP edge state has exponential localization as well. The TP edge states of the same quasienergy, localized on the two different boundaries overlap due to their exponential tails in the bulk [88].

3.3 Quantum Walks in 2D and their Topological Properties

To simulate transport phenomena and topological phases, QWs have been extended to 2D. In the beginning it was demonstrated that 2D QWs realize topological phases with topological invariants similar to the ones characterizing integer quantum Hall phases, i.e. the Chern numbers [84]. However, these invariants do not give a full characterization of periodically driven systems. Later in this section, we will demonstrate that due to the Floquet character of the QWs, edge modes exist even the Chern numbers assigned to the bulk bands of the effective Hamiltonian predict none. Various topologically phases in 2D can be realized using different walk protocols on lattices with different geometries. I will introduce topological properties of QWs on the square lattices, which our group is aiming to investigate with the newly constructed 2D machine [92].

Let us consider a 2D extension of the 1D-standard protocol. A particle having two spin degrees of freedom, is now positioned on a 2D square lattice. The coordinates on the lattice are labelled by $\boldsymbol{x} = (x, y) \in \mathbb{Z}^2$ with basis vectors denoted by $|x, y\rangle$ spanning a 2D Hilbert space. In a simple case, the walk operator consists of two coin operators and two shift operators (one for shifting particle along the x axis and other for shifting along the y axis of the 2D lattice). For a homogenous 2D QWs, the coin operator can be written by modifying the definition eq. (3.3) in the following way,

$$\hat{C}(\theta) = \sum_{x,y} |x, y\rangle \langle x, y| \otimes e^{-i\frac{\theta\, \sigma_y}{2}} = \sum_{x,y} |x, y\rangle \langle x, y| \otimes \begin{pmatrix} \cos(\theta/2) & -\sin(\theta/2) \\ \sin(\theta/2) & \cos(\theta/2) \end{pmatrix}. \tag{3.32}$$

Similarly, the shift operators along the x axis and the y axis can be written as

$$\hat{S}_x = \sum_{x,y} \left(|x + 1, y\rangle \langle x, y| \otimes |\!\uparrow\rangle \langle\uparrow\!| + |x - 1, y\rangle \langle x, y| \otimes |\!\downarrow\rangle \langle\downarrow\!| \right), \tag{3.33}$$

$$\hat{S}_y = \sum_{x,y} \left(|x, y + 1\rangle \langle x, y| \otimes |\!\uparrow\rangle \langle\uparrow\!| + |x, y - 1\rangle \langle x, y| \otimes |\!\downarrow\rangle \langle\downarrow\!| \right). \tag{3.34}$$

The shift operator ($\hat{S}_x$) shifts a walker in spin-up (spin-down) state by one lattice site in the positive (negative) x direction leaving the y coordinate of the walker unchanged. Similarly, The $\hat{S}_y$ shifts a walker in spin-up (spin-down) state by one lattice site in the positive (negative) y direction leaving the x coordinate of the walker unchanged. These operator constitute the walk protocol for 2D QWs, which takes the following form,

$$\hat{W}_{2D} = \hat{S}_y \hat{C}(\theta_2) \hat{S}_x \hat{C}(\theta_1). \tag{3.35}$$

A schematic of the walk protocol (for the 2D Hadamard-like walk) and the evolution of a walker for a single step of the walk is shown in fig. 3.9 (the walker is initially prepared in spin-up state localized at a single site of the 2D lattice).

For homogenous QWs on an infinitely extended lattice, or a lattice with periodic boundary conditions along the x and the y axes, these operators can be transformed into quasimomentum space by using the Fourier transformation introduced in sec. 3.1.2. In the quasimomentum representation, the coin operator is again diagonal and the shift operators take the following form:

$$\hat{S}_x(k_x) = e^{-ik_x} |\!\uparrow\rangle \langle\uparrow\!| + e^{ik_x} |\!\downarrow\rangle \langle\downarrow\!|, \tag{3.36}$$

$$\hat{S}_y(k_y) = e^{-ik_y} |\!\uparrow\rangle \langle\uparrow\!| + e^{ik_y} |\!\downarrow\rangle \langle\downarrow\!|, \tag{3.37}$$

here k_y is the quasimomentum along the y direction and takes values, similar to k_x, inside the first quasimomentum BZ (which is now a 2D BZ), i.e. $k_y \in [-\pi, \pi[$. The walk operator in quasimomentum
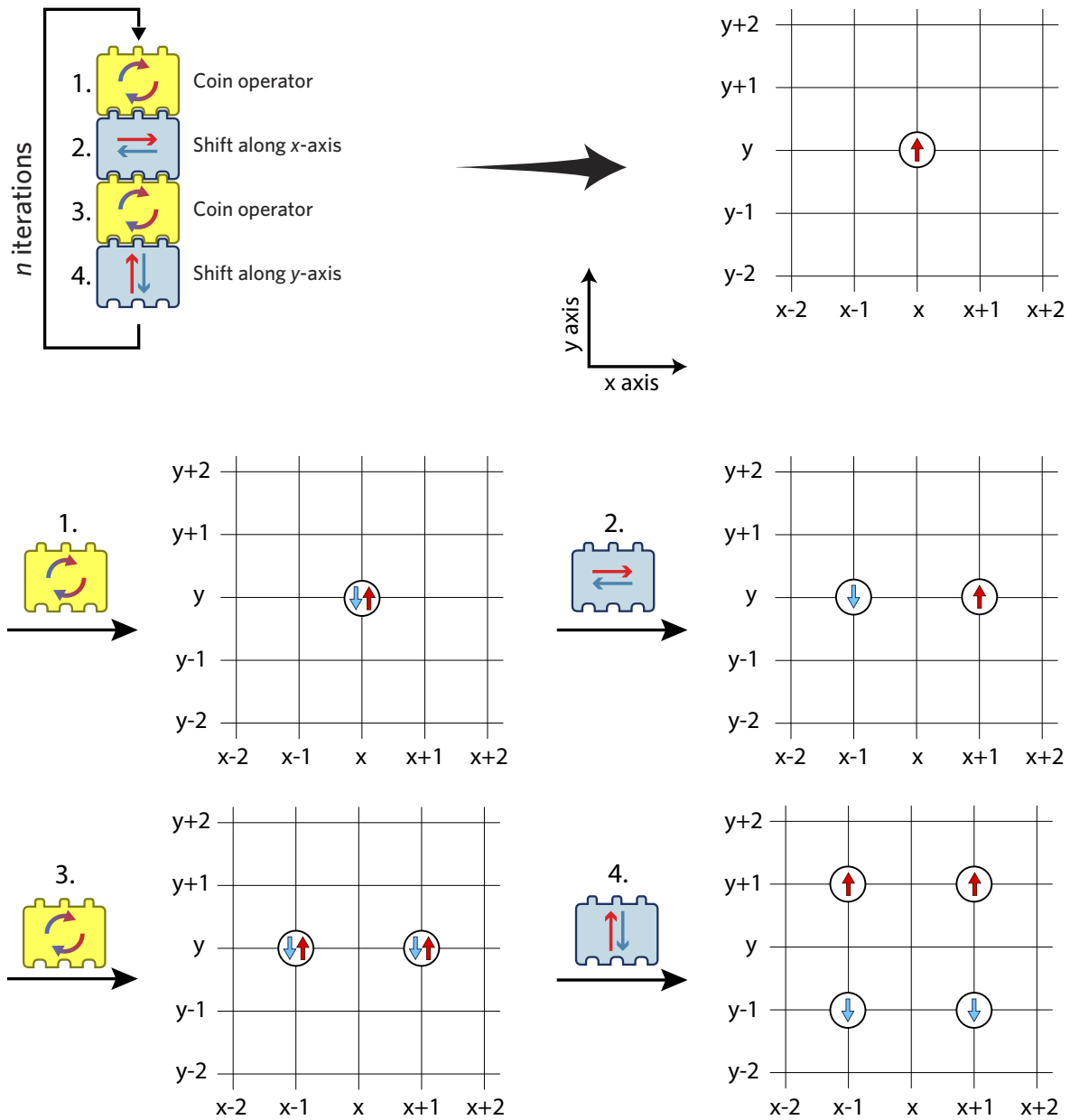
Figure 3.9: Schematic illustration of a simple 2D Hadamard-like QW (both coin angles, i.e. θ_1 and θ_2 are considered to be $\pi/2$, hence each coin operator prepares each spin state into an equal superposition of the two spin states). Top row left, a connected-blocks representation of the walk protocol and at the right is the schematic of a particle's initial state, which is positioned on the square lattice with spin-up internal state. Middle and last rows show the evolution generated by one step of the walk. After a single step, spin-up (spin-down) state is shifted by one lattice site along the positive (negative) x axis and by one lattice site along the positive (negative) y axis. The probability of the particle to be in a given spin state and at a given lattice site is not schematized in this illustration.

space can be written as,

$$\hat{W}_{2D}(k_x, k_y) = \hat{S}_y(k_y)\hat{C}(\theta_2)\hat{S}_x(k_x)\hat{C}(\theta_1). \tag{3.38}$$

The quasienergy spectrum of the corresponding effective Hamiltonian consists of two bands, which, depending on the values of the coin angles, can be gapped or gapless. The gapped phases are topologically non-trivial. In contrast to the 1D case, the existence of a non-trivial topological phase in 2D does not rely on any symmetry, e.g. quantum Hall phase (discussed in chap. 2). For 2D time-independent lattice Hamiltonians, in the presence of translational invariance with no additional symmetries, Chern numbers are used to fully characterize the topological properties of the system. The Chern number is evaluated for each single band or group of touching bands separated by a gap from other bands[6]. For the 2D QW, the Chern number of both bands is zero, which reflects the fact that the effective Hamiltonian is topologically trivial. However, there exist TP edge states whose topological invariants are not covered by the standard theory of topological phases [86]. This is in stark contrast to 2D static systems, where chiral edge states exist in the bulk gaps if the bulk bands have non-vanishing Chern numbers (as shown in chap. 2). In 2D QWs, TP edge modes have been numerically studied although the underlying topological invariants were not known at that time [84]. The corresponding topological invariants were found by J. K. Asbóth and J. M. Edge [93], where by mapping the QW to a periodically driven lattice Hamiltonian, they identified the invariants of the gaps ($\nu \in \mathbb{Z}$). These are the QWs analogue of the winding number found by Rudner et al. [75]. The Rudner invariant (or simply RLBL invariant) is assigned to the bulk Floquet gap, which determines the number of chiral edge modes crossing this gap. The invariant for any other bulk gap can be computed by shifting that particular gap to the quasienergy BZ boundary.

I compute the Chern number of the bands using the method similar to the one discussed in Appendix C. The gap invariants are computed with techniques outlined in Chapter 5. The phase diagram for the simple 2D QWs, characterized by the RLBL invariant as a function of the two coin angles, is shown in fig. 3.10 (a). The RLBL number of each phase is indicated by a bold letter and the Chern number is indicated by a normal letter (which is always zero for this walk). Inside each phase, the quasienergy spectrum has two gaps, i.e. one around ($\varepsilon = 0$) and another around ($\varepsilon = \pi$). Both gaps close at phase boundaries of the phase diagram.

Similar to the 1D case, TP edge states exist in 2D in the presence of a boundary, separating two distinct topological phases. These states are propagating uni-directionally (chiral edge states) in the bulk gaps and connect the bulk bands. A particle, that is prepared in the superposition of the TP edge states, propagates coherently along the spatial boundary. The chirality of the edge states is topologically protected, i.e. their direction of propagation cannot be changed by continuously changing the parameters of the system as long as the bulk gaps remain open. For details on changing the chirality of an edge mode by closing a bulk gap, see the paper by J. K. Asboth and J. M. Edge [93].

I demonstrate TP propagating edge modes by considering an inhomogeneous 2D QW with two coin angles (θ_1 and θ_2) depending on the x coordinate of the lattice. I consider a flat boundary in form of a strip geometry in the 2D lattice (see fig. 3.10 (b) for schematic illustration of the strip), where the pair of coin angles inside and outside the strip belongs to different topological phases. The considered pairs of coin angles are

$$1 \rightarrow 2: \quad \theta^{\text{in,out}} = \begin{cases} (\theta_1^{\text{in}}, \theta_2^{\text{in}}) = (-3\pi/4, \pi/4) & \text{if } |x| << x_o \\ (\theta_1^{\text{out}}, \theta_2^{\text{out}}) = (-\pi/4, 3\pi/4) & \text{if } |x| >> x_o, \end{cases} \tag{3.39}$$

with the width of the strip equal to $2x_o$. The pair of coin angles inside the strip ($|x| << x_o$) realizes

---

[6] In this case, Chern numbers can be defined as the winding number of the mapping from the 2D quasimomentum BZ, which is a torus, to a unit Bloch sphere [84].
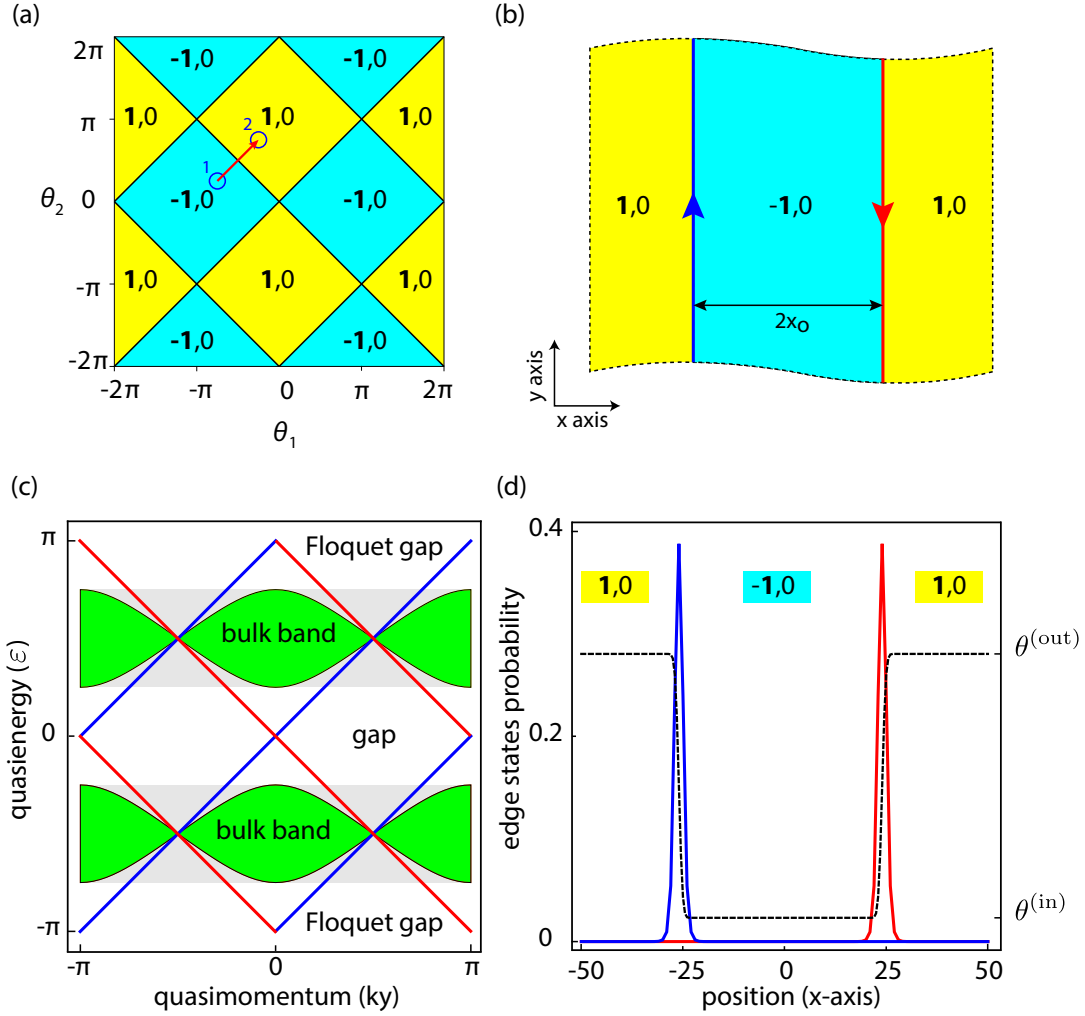
Figure 3.10: Phase diagram and edges spectrum of the simple 2D QW. (a) Topological invariants of the walk as a function of the two coin angles (θ_1 and θ_2) characterizing different topological phases (as defined in [93]). The numbers in bold represent the RLBL invariant of the corresponding topological phases. The Chern number of each phase is also shown (normal letter), which is always zero. At the phase boundaries, the band gaps close both at $\varepsilon = 0$ and $\varepsilon = \pi$. (b) Schematic of a strip boundary implemented in the 2D lattice for demonstrating the edge spectrum of the walk. (c) Quasienergy spectrum of the inhomogeneous QW where the pair of coin angles makes a transition from one topological phase to another. The two gapped bands (light green) represent the bulk spectrum and the unidirectionally propagating modes in the bulk gaps represent the edge spectrum (solid lines with red and blue colors). The chirality of each mode is topologically protected. (d) Edge modes of opposite chiralities are spatially localized on different boundaries of the strip. Each mode is represented by the same color (red, blue) as in (c). In order to indicate the position of the boundaries in the lattice, the spatial variation of the coin angles along the x axis is overlaid on top of the edge states probabilities (black dashed). The coin angles are independent of the y coordinate and hence the y axis of the plot is not shown. The topological invariants corresponding to each domain are indicated. Here θ^{in} (θ^{out}) is the pair of coin angles chosen for the lattice sites that are lying inside (outside) the strip. In the phase diagram (a), θ^{in} and θ^{out} lie in different topological phases and are represented by circles with numbers 1 and 2 respectively.

a topological phase with the winding number -1 and the one outside the strip ($|x| >> x_o$) realizes a topological phase with the winding number $+1$. According to the bulk–boundary correspondence principle, two TP edge modes are expected to exist at the two boundaries of the strip.

The considered configuration has translational invariance along the y axis and hence k_y is still a good quantum number. I numerically compute the quasienergy spectrum of the corresponding effective Hamiltonian and plot it as a function of k_y in fig. 3.10(c). The quasienergy spectrum consists of two main parts: bulk spectrum and edge spectrum. The bulk spectrum consists of two gapped bands. The edge spectrum consists of unidirectionally propagating modes in the bulk gaps (there are two gaps, one around $\varepsilon = 0$ and other $\varepsilon = \pi$). For a given quasienergy ε, there are two edge modes per boundary (or of a given chirality) in each gap (edge modes of opposite chiralities are shown by different colors, i.e. red and blue). This can be understood from the bulk–boundary correspondence, as the absolute value of the algebraic difference of the topological invariants of the two phases is equal to two. The slope of the edge mode's dispersion gives the group velocity of the wavepacket which is $+1$ (in units of a number of sites per step of the walk) for the edge mode represented by a blue line and is -1 for the one represented by a red line. It is worth mentioning that the dispersionless transport (the group velocity is independent of k_y) of the edge modes is property of the walk protocol eq. (3.35) and not related to the topological features [91]. Edges modes are spatially localized at the boundary and have exponential tails extending into the bulk (fig. 3.10(d)). The edge modes with opposite chiralities (group velocities) are spatially localized at different boundaries of the strip. Quantum transport on a chiral edge mode along a given boundary is immune to backscattering, as there are no counterpropagating modes on that particular edge to which it can scatter. The only counterpropagating modes are the ones localized on the other edge of the strip, but coupling to those is exponentially suppressed.

The robustness of TP edge modes against spatial deformation of the boundary can be tested by defining a closed boundary of irregular shape in the lattice, with the winding number inside the closed boundary different than its outside region. By initializing a walker closed to the boundary (so that the initial state of the walker has significant overlap with an edge mode) and evolving it for a large number of steps of the walk, numerical studies indeed show that the walker remain propagating along the boundary even after a large number of revolution around the boundary [91]. I will demonstrate the robustness of TP edges modes in the next chapter while studying the topological properties 2D QWs in the presence of a synthetic magnetic field.

Quantum Walks on the Square Lattice in the Presence of a Synthetic Magnetic Field

Iɴ Chapter 2 I introduced the physics of a tightly bounded charged particle in 2D in the presence of an external magnetic field. The energy spectrum consists of discrete magnetic Bloch bands which have non-trivial topological structure indicated by the non-vanishing values of their Chern numbers. These bands, besides being topologically non-trivial, are nearly flat and separated by large gaps. Such flat bands with non-vanishing Chern numbers are of interest for realizing interaction-induced topological phases such as fractional quantum Hall states for partially filled Chern bands, known as fractional Chern insulators [15–17]. These topological phases, protected by a large energy gap, are expected to survive at high temperatures, possibly even at room temperature in electronic solid-state systems [18]. Nearly flat bands with non-vanishing Chern numbers and large gap separation have been identified as favorable conditions to realize these states, since in these circumstances interactions among particles are the dominating physical mechanism [19–21]. Efforts have been made, both in solid-state materials and neutral atoms setups, to access these novel topological phases. In this journey, the first demonstration of an integer Chern insulator has been reported in a solid-state magnetic topological insulator [11] and with ultracold atoms trapped in optical lattices [12, 13] in the regime of weakly or non-interacting particles. However, no experimental realization of fractional Chern insulators has been reported yet. In solid-state materials, the requirements of strong magnetic fields and ultra-clean samples pose major challenges for their realization. In systems of cold neutral atoms in optical lattices, one of the main challenge to access these phases is to carry such experiments at extremely low energy scales, corresponding to few nK. However, this in turn reduces the tunneling rates and increases the evolution times, during which heating [39, 42] and other decoherence mechanism can be harmful to the coherent evolution of the system.

In this chapter, I map out a different way to realize Chern insulators by making use of Floquet-engineering, where the 2D QW protocol (introduced in Chapter 3) is modified to include artificial magnetic fields. I start with an extension of a simple 2D Hadamard-like walk to introduce the magnetic QW protocol. For rational values of the flux ratio (ϕ), the quasienergy spectrum of the walk has a fractal structure, which we call "the Floquet Hofstadter butterfly". I demonstrate, by computing the Chern numbers of the bulk bands (sec. 4.1.2) and studying the excitation of midgap TP edge modes extended all along the boundary between different magnetic domains, that the system behaves like a Chern insulator (sec. 4.2). For experimental implementation with neutral atoms, we propose a realistic scheme based on QWs to artificially engineer arbitrary magnetic field landscapes, including those with sharp spatial boundaries (sec. 4.3). The proposed scheme does not rely on laser-assisted tunneling of neutral atoms

in a lattice rather atoms are delocalized through state-dependent transport. This avoids the problem of photon scattering by the dressing laser and the problem of damping of tunneling rates that arise when working with super lattice potentials.

4.1 Quantum Walk in a Synthetic Magnetic Field

We use the magnetic QW protocol (an extension of the simple 2D QW protocol given by eq. (3.35) of Chapter 3) to simulate the effects of a synthetic magnetic field in the 2D squared lattices. Let us consider a single particle with two internal states (same as I have considered in Chapter 3) labeled by $s \in \{\uparrow, \downarrow\}$. The walker is positioned on the 2D square lattice, with coordinates $\boldsymbol{x} = (x, y) \in \mathbb{Z}^2$. The magnetic QW protocol consists of a sequence of unitary operators: the coin, the shift, and the magnetic field operator. The coin operator $\hat{C}$ is a Hadamard-like coin [80, 81] that is given by eq. (3.4) of Chapter 3. The shift operators ($\hat{S}_x$ and $\hat{S}_y$) are given by equations (3.33), (3.34) of Chapter 3. The magnetic field operator is introduced to simulate the effects of a magnetic field with QWs. This imprints spin-dependent phases, analogous to the Peierls' phases, to the walker's wave function in a stroboscopic manner. These phases depend on the coordinates of the walker and on the choice of the gauge. I choose a Landau gauge $\vec{A}(x) = (0, Bx, 0)$, which corresponds to a synthetic magnetic field of strength B pointing along the positive normal of the xy plane of the 2D lattice. The magnetic field operator ($\hat{F}$) is defined as

$$
\hat{F} = \sum_{x,y} \left(e^{iBx} |x, y\rangle \langle x, y| \otimes |\uparrow\rangle \langle\uparrow| + e^{-iBx} |x, y\rangle \langle x, y| \otimes |\downarrow\rangle \langle\downarrow| \right)
$$

$$
= \sum_{x,y} |x, y\rangle \langle x, y| \otimes \begin{pmatrix} e^{iBx} & 0 \\ 0 & e^{-iBx} \end{pmatrix}, \tag{4.1}
$$

where B can be written in terms of the flux ratio as $B = 2\pi\phi$. Combining the magnetic field operator with the coin and shift operators, the protocol for magnetic QW can be written in the following way:

$$
\hat{W}_{\text{2DM}} = \hat{F}\, \hat{S}_y\, \hat{C}\, \hat{S}_x\, \hat{C}. \tag{4.2}
$$

We evolve the quantum state of the walker by applying this protocol periodically at discrete time steps $n \in \mathbb{N}$. The effect of each unitary operator on the walker is schematically illustrated in fig. 4.1. The final state of the walker, when the walk protocol is applied n-times to its initial state $|\psi_{\text{init.}}\rangle$, is denoted by

$$
|\psi_n\rangle = \hat{W}_{\text{2DM}}^n |\psi_{\text{init.}}\rangle. \tag{4.3}
$$

4.1.1 Quasienergy Spectrum of the Bulk: the Floquet Hofstadter Butterfly

The dynamics of the walker has discrete translational invariance in time due to the periodic driving through the walk protocol. I have set, for simplicity, the time period T equal to 1. As already discussed in Section 3.1.2, the evolution of the quantum state of the walker after an integer number of steps can be reproduced by a static effective Hamiltonian, linked to the walk protocol through $\hat{W}_{\text{2DM}} = \exp(-i\hat{H}_{\text{eff.}})$. The eigenvalues of this effective Hamiltonian form the quasienergy spectrum of the walk. Just like the quasimomentum, which arises due to discrete translational invariance in space, the quasienergy arises due to discrete translational invariance in time and can be uniquely defined only up to an integer multiple of 2π.

To study the bulk quasienergy spectrum of the walker, I consider the 2D square lattice of size $M \times N$ (here $M, N \in \mathbb{N}$) with periodic boundary conditions, i.e. $M + 1 = 1$ and $N + 1 = 1$, ensuring the discrete
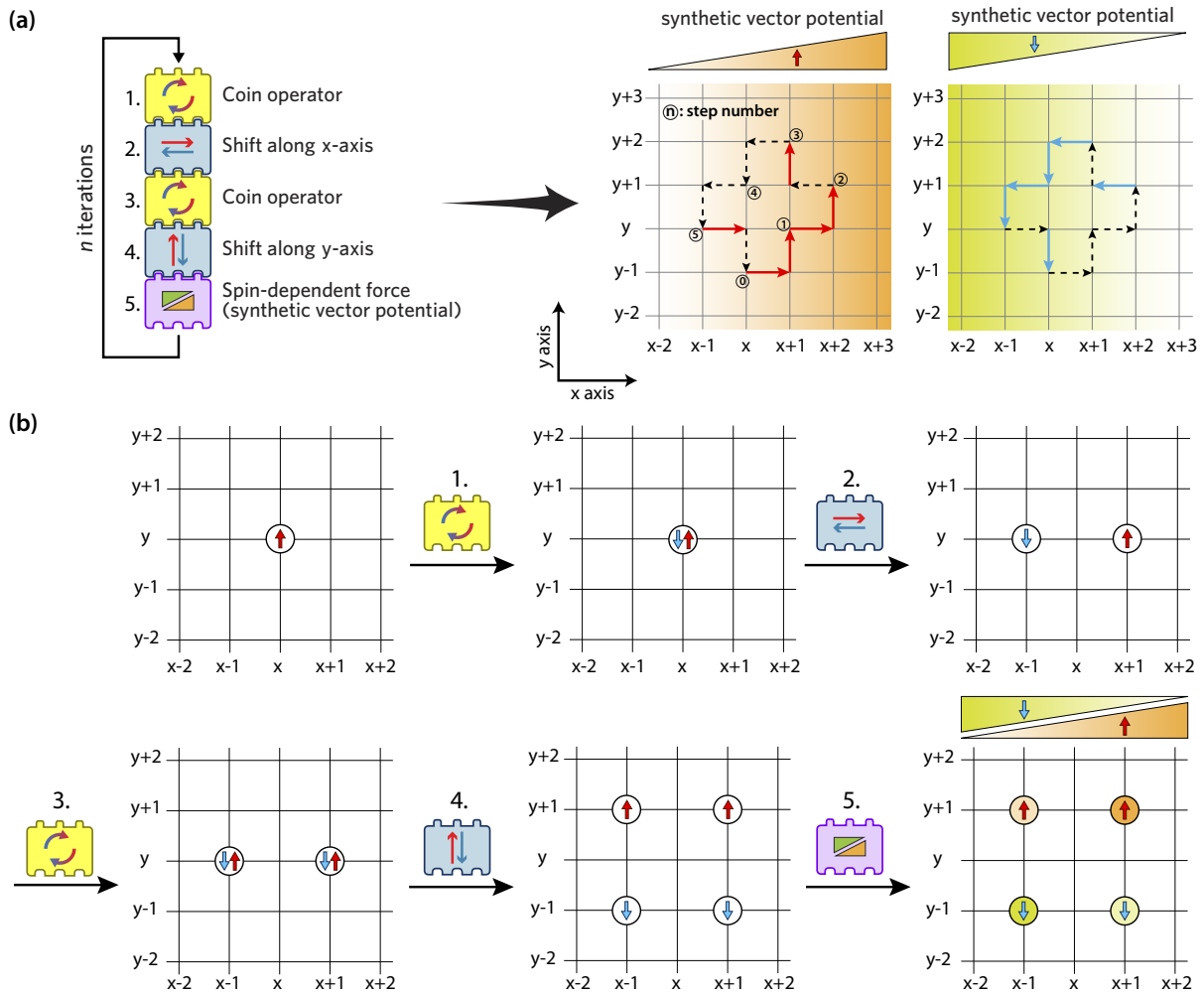
Figure 4.1: Schematic illustration of the implementation of 2D magnetic QW and the resulting Peierls phases. (a) At the left side is the connecting-block representation of the walk protocol and at the right side is shown one of the possible closed trajectory the walker can follow under the walk protocol. Two separate lattices are used to show that the direction of the vector potential gradient is opposite for the two spin states. (b) The evolution of a walker, initially prepared in a spin-up state, under a single step of the walk protocol. An atom is first delocalized in the lattice through spin-dependent shift operators (labelled with 1 to 4) and then a spin-dependent force (called a magnetic field operator) is applied (labelled with 5) to implement the so called Peierls phases mimicking the effect of a magnetic field on a charged particle.

spatial translational invariance. In the absence of a magnetic field, the walk protocol is diagonal in momentum space and quasimomentum is a constant of motion. The presence of a magnetic field breaks the translational invariance of the problem and quasimomentum is no longer a good quantum number. However, for rational values of the flux ratio $\phi = p/q$, translational invariance can be restored by defining the so called magnetic unit cell, which is q-times larger than the original unit cell of the lattice. The corresponding quasimomentum BZ is q times smaller and the values of quasimomentum quantum number are restricted to the reduced BZ, $[-\pi/q, \pi/q[$. For the chosen Landau gauge, the walk protocol does not depend on the y coordinate and hence k_y is still a good quantum number having values that are restricted to the first BZ $[-\pi, \pi[$.

Figure 4.2 shows the quasienergy spectrum for a vanishing magnetic field (Hadamard-like walk) and a non-vanishing magnetic field with $\phi = 1/3$. The quasienergy spectrum for the vanishing strength of magnetic field exhibits Dirac-like points[1] and is behaving like a non-insulator. There are two gaps that are closing: one at $\varepsilon = 0$ and the other at $\varepsilon = \pm\pi$. The presence of a magnetic field splits each band into magnetic subbands, which are gapped (for a magnetic field that results in $\phi = p/q$, each band splits into q subbands as there are q states per magnetic unit cell). The system becomes topologically non trivial as the the magnetic subbands are characterized by non-vanishing Chern numbers. Due to the fact that here we have quasienergies instead of real energies, we call this system a Floquet Chern insulator. The quasienergy spectrum as a function of $\phi = p/q$ has periodic structure as was the case for the time-independent tight-binding model with magnet fields (chap. 2). We show this behavior in fig. 4.3 while scanning the values of p/q from 0 to 1. The walker has twice as many states per unit cell as compared to a spin-less particle. As a result, for each $\phi = p/q$, the quasienergy bands get doubled with respect to the original Hofstadter spectrum [24]. We call this figure *Floquet Hofstadter butterfly* (see fig. 2.3 for comparison). The specific case of flux ratio with $p = 1$ and $q = 3$ is highlighted in fig. 4.3 with colors.

4.1.2 Topological Invariants of the Magnetic Quantum Walk

As shown in sec. 2.3.2, the topological invariants of a 2D time-independent lattice Hamiltonian are Chern numbers of the energy bands. Each band, or, more generally, each set of bands that is separated by energy gaps from the other bands has an integer Chern number. For a system with a boundary, the Chern numbers can be used to predict the net number of edge modes crossing any of the bulk energy gaps (as demonstrated in sec. 2.3.3). The magnetic subbands of the magnetic QW have also non-vanishing Chern numbers. The example in fig. 4.2 shows that some of the magnetic subbands touch: the 3rd and the 4th band touch at $\varepsilon = 0$ and the 1st and 6th band touch at $\varepsilon = \pi$. I compute the Chern numbers for all sets of subbands using the numerical method [59] outlined in Appendix C and include the values of these Chern numbers in fig. 4.2. The method involves the numerical integration of the non-abelian Berry curvature of the set of subbands over the quasimomentum BZ. Due to the presence of CS in the magnetic QW, the Chern number of a band at quasienergy ε is the same as that of $\varepsilon + \pi$.

The Chern numbers of the effective Hamiltonian do not completely characterize the bulk topology of 2D QWs. One can expect that the simple form of bulk–boundary correspondence mentioned above does not hold [84], since quasienergy is a periodic quantity, and so the "sum of Chern numbers below a band gap" is, strictly speaking, not meaningful for QWs. Indeed, to a QW with N bulk quasienergy gaps, one can assign N gap invariants (based on RLBL invariant) ν_i, with $i = 1, \ldots, N$, e.g. through a mapping to a periodically driven Hamiltonian [93] and using a construction introduced by Rudner et al. [75]. The

---

[1] These are the points inside the quasimomentum BZ where the two quasienergybands touch each other. The quasienergy dispersion in the proximity of these points is linear in k_x and k_y. This is similar to the dispersion of low-energy electrons in graphene around the band touching points (known as Dirac points), where electrons behave like massless Dirac fermions [4].
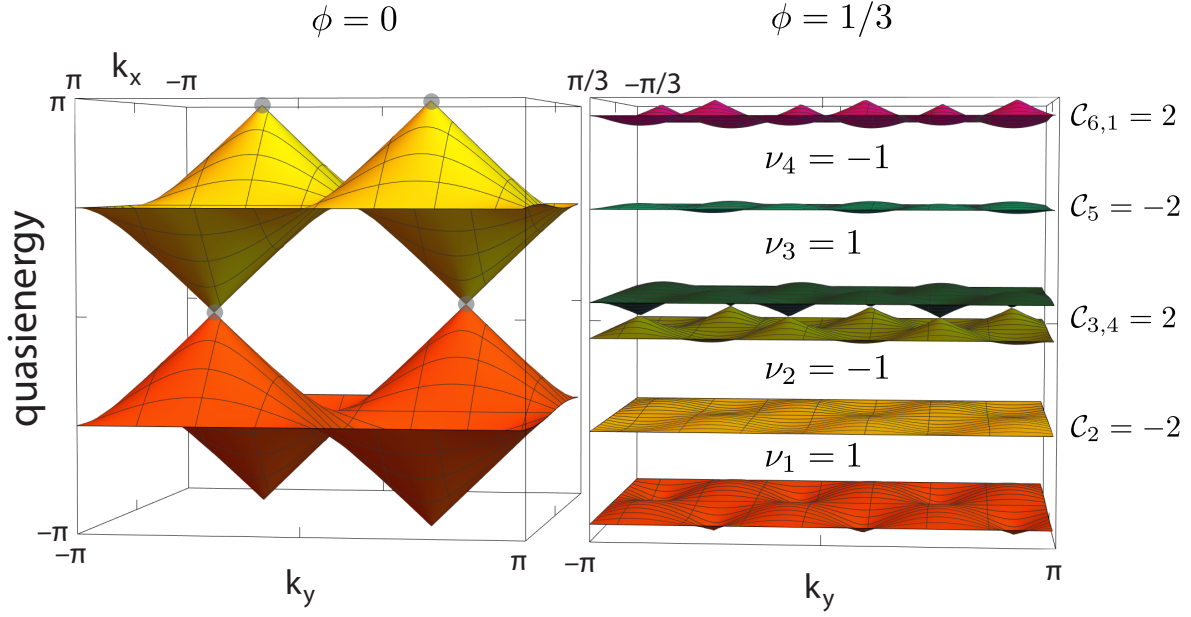
Figure 4.2: The quasienergy spectrum of the walk protocol $\hat{W}_{2DM}$, for a vanishing magnetic field (left), exhibits Dirac like points and has non-insulating behavior. Applying a magnetic field with $\phi = 1/3$ (right), splits each of these 2 bands into 3 magnetic subbands, which preserves the inner-most-bands and outer-most-bands touching as well as the linearity of the spectrum where the bands touch. The spectrum shows insulating behavior and is topologically non-trivial. The numerically computed Chern numbers (denoted by C, with indices representing the respective bands), in the non-vanishing magnetic field case, are shown at the right side. The gaps invariants of the gaps, denoted by ν_i, $i \in [1, 4]$, are indicated in their respective gaps and are computed numerically using the procedure explained in Appendix F. The difference of gaps invariants of any two gaps is equal to the sum of the Chern numbers of the bands lying between these two gaps.

bulk–boundary correspondence for QW states that the gap invariant ν_n of each gap gives the net number of edge states crossing that gap at an edge with (the appropriately defined) vacuum.

I compute the topological invariants of the band gaps by tracking the spectral flow induced by an additional magnetic field [94]. The details of this computation are given in Appendix F. The computed value of the topological invariant for each gap is shown in fig. 4.2. As expected [75], the gap invariants are related to the Chern numbers: The difference of the gap invariants at two different quasienergies is equal to the sum of the Chern numbers of all the bands lying in between these quasienergies. This can be easily verified from the values given in fig. 4.2.

4.1.3 Evolution of the Walker in a Weak Magnetic Field

From solid-state systems, it is a well known fact that the expectation value of the position of a wave packet (describing a nearly free charged particle) in an external quantizing magnetic field follows a circular orbit resembling the dynamics of a classical particle. However, the presence of a 2D periodic potential (lattice) drastically modifies the evolution trajectory when the length scale of the lattice (e.g. with lattice constant of unit length) is comparable with the magnetic length scale, i.e. $\ell_B \approx 1$. This is the regime of strong magnetic fields. In this regime, the energy bands are nearly flat and the particle is strongly localized. This can be demonstrated in simulations by initializing a walker in a given spin state localized around a lattice site and evolving through the walk protocol given by eq. (4.2). However, in the weak magnetic
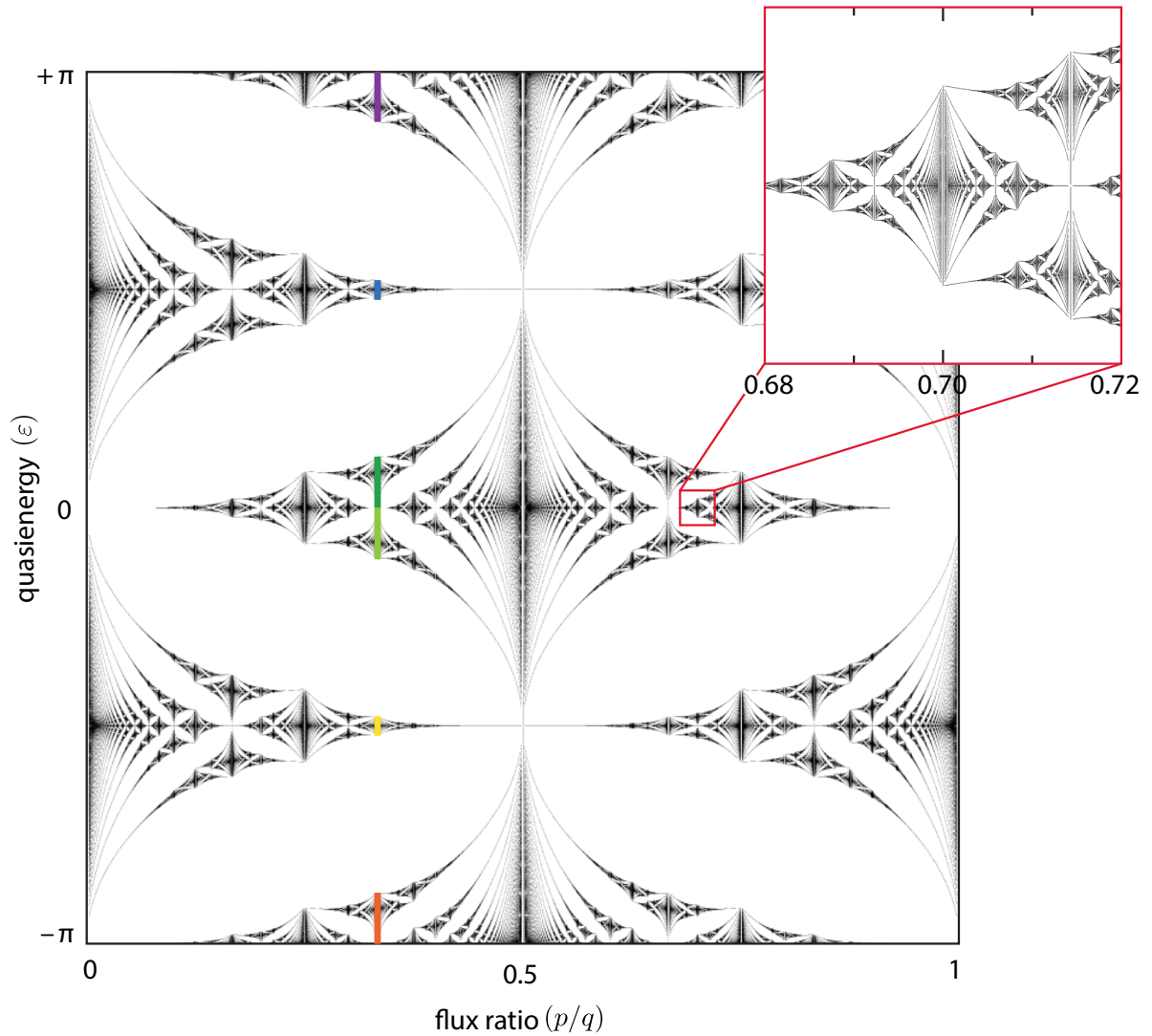
Figure 4.3: Floquet Hofstadter butterfly, showing that the number of bands is two times q for a given $\phi = p/q$. The colored vertical lines show the quasienergy band-widths corresponding to the quasienergy spectrum of fig. 4.2, right, i.e. for $p = 1$ and $q = 3$. From the spectrum it is apparent that the widths of the bands are smaller (characterized by non-vanishing Chern numbers) than the gaps and hence the system is a type of flat-band Floquet Chern insulator.

field regime, i.e. $\ell_B >> 1$, the role of the lattice is minute (long wavelength limit) and the particle is expected to move on a circular trajectory in the lattice.

I demonstrate the evolution of the walker on a circular orbit by considering a weak magnetic field. A walker is initially prepared in a momentum state having a 2D gaussian envelope with initial spread over several lattice sites, i.e.

$$|\psi_{\text{init.}}(\mathsf{q}_x, \mathsf{q}_y)\rangle = \sum_{x,y} \sqrt{\mathbb{G}_w(x,y)} \, e^{i\mathsf{q}_x x} e^{i\mathsf{q}_y y} |x, y, s\rangle, \qquad (4.4)$$

$$\text{with } \mathbb{G}_w(x,y) = \frac{1}{2\pi w^2} e^{-\left[\frac{(x-x_o)^2 + (y-y_o)^2}{2w^2}\right]}.$$

here $\mathbb{G}_w(x,y)$ is the normalized gaussian probability density of the initial state centered at $x = x_o$, $y = y_o$ and w is its initial spread. The components of the the initial momentum, i.e. $\mathsf{q}_x = k_x - K_x$ and $\mathsf{q}_y = (k_y + Bx_o) - K_y$ (where $K = \{K_x, K_y\}$ is the location of a Dirac point in the BZ as given in Appendix E), are defined with respect to a Dirac point of the dispersion shown in fig. 4.2 (left). Since quasimomentum $k = (k_x, k_y)$ is a gauge-dependent quantity, we have considered its gauge invariant form, i.e. $k = (k_x, k_y + Bx_o)$, which is proportional to the initial velocity of the wavepacket. Spin state should be chosen to represent a single band (upper or lower band, when there is no magnetic field). The quasienergy spectrum of the walk (fig. 4.2), close to Dirac points has dispersion similar to that of low energy Dirac fermions in graphene. The effective Hamiltonian, after series expansion around a Dirac point to first power in q_x and q_y, shows Rashba type spin-orbit coupling, i.e. $H_{\text{eff}} \approx -\mathsf{q}_y \sigma_x \pm \mathsf{q}_x \sigma_y$ (see Appendix E for the expansion of effective Hamiltonian around a Dirac point). In this case, the velocity of the walker is equal to 1 in units of lattice sites per step of the walk evolution. As a consequence of this linear dispersion, the walker moves at constant (maximum) speed of 1 lattice site per step of the walk. I consider that the initial state of the walker is displaced by $\mathsf{q}_{x,y}$ from one of the four Dirac points in the BZ. By applying a weak magnetic field, the walker evolve on a circular orbit. From semiclassical theory, I estimate the radius of the circular trajectory, in units of lattice sites, equal to $\mathsf{q}_{x,y}/(2\pi\phi)$ and the evolution period, in units of QW steps, equal to $\mathsf{q}_{x,y}/\phi$. The time evolution is shown in fig. 4.4 for a magnetic field strength with $\phi = 1/1200$. The numerical result matches the semiclassical estimations, i.e. the radius of the cyclotron orbit and evolution period, quite well.

4.2 Edge Spectrum of the Magnetic Quantum Walk

The bulk quasienergy spectrum shown in fig. 4.2 manifests non-trivial topological behavior, i.e. the gap invariant of each bulk gap is a non-zero integer number, and hence TP edge states are expected to exist in the presence of a spatial boundary. There are several techniques of implementing such boundaries in a system, like using split-step QW protocol with inhomogeneous coin angles [84, 91], using reflective coins or setting tunneling amplitudes of the walker equal to zero at spatial boundaries [73]. However, I define a boundary by making a sharp transition between two magnetic domains, where magnetic field in one domain points in opposite direction with respect to the field in the other one. This demonstrates the power of the QW protocols, i.e. it allows for the local control of the walk parameters, and one of the advantage of our proposed scheme, i.e. it allows for simulating arbitrary landscapes of magnetic fields. A similar configuration has been realized in condensed matter systems where the so called snake states[2] have been observed either by inverting the magnetic field direction or by changing the type of charge carriers at the interface [95–97]. However, these observations are limited to weak magnetic fields only

---

[2] Snake states are open orbits (with opposite chiralities) of charged particles that arise in a 2D system of charged particles in the presence of a spatially inhomogeneous magnetic field [95].
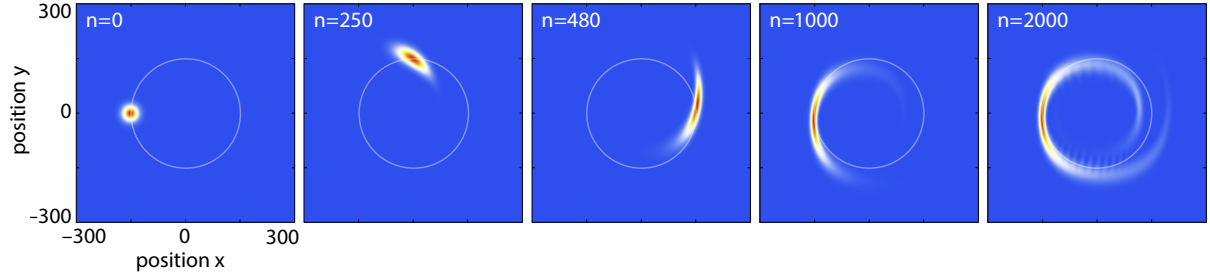
Figure 4.4: The time evolution of a walker, initially prepared in a momentum state with average momentum close to one of the four Dirac points. The initial state has a 2D Gaussian probability density profile and is spread over 15 lattice sites ($w = 15$) in both directions of the lattice. The animation is generated for a flux ratio $\phi = 1/1200$ and the average value of momentum is $q_{x,y} = 0.25\pi$ with respect to the Dirac point at $\{\pi/2, -\pi/2\}$. The color scale is rescaled in order to maintain a constant visibility of the wave packet, since the matter wave spreads out with time over several lattice sites. The dark red color represents the maximum, white the intermediate and blue the minimum of the probabilities. The radius of the orbit and the evolution period fits very well with the semiclassical estimations.

as the strong magnetic field regime was not accessible in these systems. In our case, we juxtapose two regions with $\phi = 1/3$ and $\phi = -1/3$ (this would correspond to $\sim 10^5$ T and $\sim -10^5$ T) that allows for the demonstration of these states in the fully quantum limit where they are interpreted as TP edge states[3].

Here I consider two types of boundaries, i.e. a 1D boundary of strip geometry and a 2D closed boundary in the form of a topological island. In both cases, a boundary separates two different non-trivial topological domains, one with magnetic field $+B$ and the other with $-B$. Mathematically, these boundaries can be realized by replacing the vector potential $A = (0, Bx, 0)$ by $A = (0, Bx, 0) \, b(x, y)$, where $b(x, y)$ is the boundary function. Experimentally, this can be accomplished by using a spatially-dependent ac Stark shift induced by a pattern of a laser field intensity with positive slope in one region and negative in the other region of the lattice (for details, see sec. 4.3). To experimentally probe the TP edge states, it is necessary to make the transition from one topological domain to the other as sharp as possible [91], in order to localize TP edge states in a small region of space. This makes it relatively easier to realize coherence lengths of the size of TP edge states in experiments. However, the diffraction limit of imaging systems sets an upper limit on the sharpness of this transition.

4.2.1 A Boundary of Strip Geometry

To demonstrate the existence of TP edge states that propagate with quasienergies in the bulk gaps, I consider a 1D boundary of a strip geometry which is shown (schematically) in fig. 4.5 (a). A strip along the y axis can be parametrized by $b(x, y) \equiv b(x) = +1$ if $x \leq x_0$ or $x > 3x_0$, and $b(x) = -1$ if $x_0 < x \leq 3x_0$ (here x_0 and $3x_0$ are the positions of the two edges of the strip). In this case, the magnetic field is no more uniform along the x axis of the lattice. Hence the magnetic translational invariance, discussed in sec. 4.1.1, is broken and k_x is not a good quantum number anymore. However, such a strip preserves the translational invariance of the walk along the y axis and k_y is still a good quantum number. This makes it possible to show the quasienergy dispersion of the walker in the presence of the strip shaped boundary as a function of quasimomentum k_y.

Figure 4.5 (b) shows the quasienergy dispersion of the walker on a lattice with $M = 60$ and $x_0 = 15$. The spectrum consists of three parts. The continuous bands (filled regions) represent the bulk spectrum

---

[3] In our case, these states exist at the interface of two distinct topological phases and hence they are protected by topology.

and the lines (solid and dashed), connecting these bands, are the TP edge states. The solid (dashed) lines represent the TP edge states that are localized at the left (right) edge of the strip. Each bulk gap has a net number of edge state equal to the invariant (ν) of the gap (states with opposite chirality on a given edge are counted with opposite sign).

4.2.2 Topological Island: A Closed Boundary

A remarkable feature of these TP edge states is their robustness against deformations in the system parameters as long as the bulk remain insulating. These states are protected by the bulk gaps and are spatially localized on the boundary separating two distinct topological domains. To demonstrate these properties, I consider a closed boundary in the form of a topological island on a 2D lattice with $M = 81$ and $N = 81$ for numerical computation. The boundary function $b(x, y)$ now defines a closed path in the xy plane. The magnetic field takes the value $-B$ inside the island, and $+B$ outside. I initialize a walker close to the spatial boundary of the topological island. In the presence of a TP edge state, the initial state of the walker will have a significant overlap with it [84]. I evolve the initial state of the walker by periodically applying the walk protocol defined in (eq. (4.2)) with inhomogeneous magnetic field. I found that after a large number of steps ($n = 500$) of the walk evolution, the walker remains localized along the boundary even in the presence of sharp corners in the boundary which act as spatial deformations. Figure 4.5 (c) shows the time evolution of an initially localized walker close to the boundary of the topological island. The numerical simulation is carried out using the realistic conditions of the experiments, i.e. taking into account the finite resolution of the imaging system. (sec. 4.3.3). For robustness of the TP edge states against experimental deformations, see fig. 4.8.

4.3 Experimental Realization with Neutral Atoms in Optical Lattices

We propose a realistic scheme for engineering an artificial magnetic field, which is based on ultra cold neutral atoms trapped in optical lattices. This scheme has a number of unique advantages. One of the unique feature of this scheme is that it does not rely on laser-assisted tunneling in a lattice but rather atoms are delocalized through state-dependent transport. Laser assisted tunneling is usually accompanied by scattering processes which results in heating the atoms. The proposed scheme avoids the problem of high scattering rates and damping of tunneling rates that arise when working with super lattice potentials. Our scheme is based on state-dependent transport, which allows to shift individual spin state of the atom over several lattice sites in a controlled way [98, 99]. This makes it possible to effectively enlarge the lattice constant and work with super lattice potentials. Another remarkable feature is that it allows for generating arbitrary landscapes of synthetic vector potentials giving the flexibility to change the direction of the simulated magnetic field at ease. This is favourable to create different topological domains with sharp spatial boundaries along which TP edge states can be localized and probed.

4.3.1 Homogeneous Magnetic Field to Study Bulk Dynamics

This scheme is based on a single neutral cesium (Cs) atom trapped in an optical lattice at a specific wavelength $\lambda_L = 866$ nm. The outermost hyperfine ground states define the two spin states of the walker, i.e. $|\uparrow\rangle = |F = 4, m_F = 4\rangle$ and $|\downarrow\rangle = |F = 3, m_F = 3\rangle$. The 2D optical lattice consists of two superimposed optical-lattice potentials with right and left circular polarizations, which are controlled independently. Due to the fact that the ac polarizability of the two spin states ($|\uparrow\rangle$ and $|\downarrow\rangle$) depends on polarization, hence each of them experiences mainly the potential of either right or left circular polarized optical lattice [100]. The spin-dependent shift is then realized by changing the polarization angles of the laser beams forming
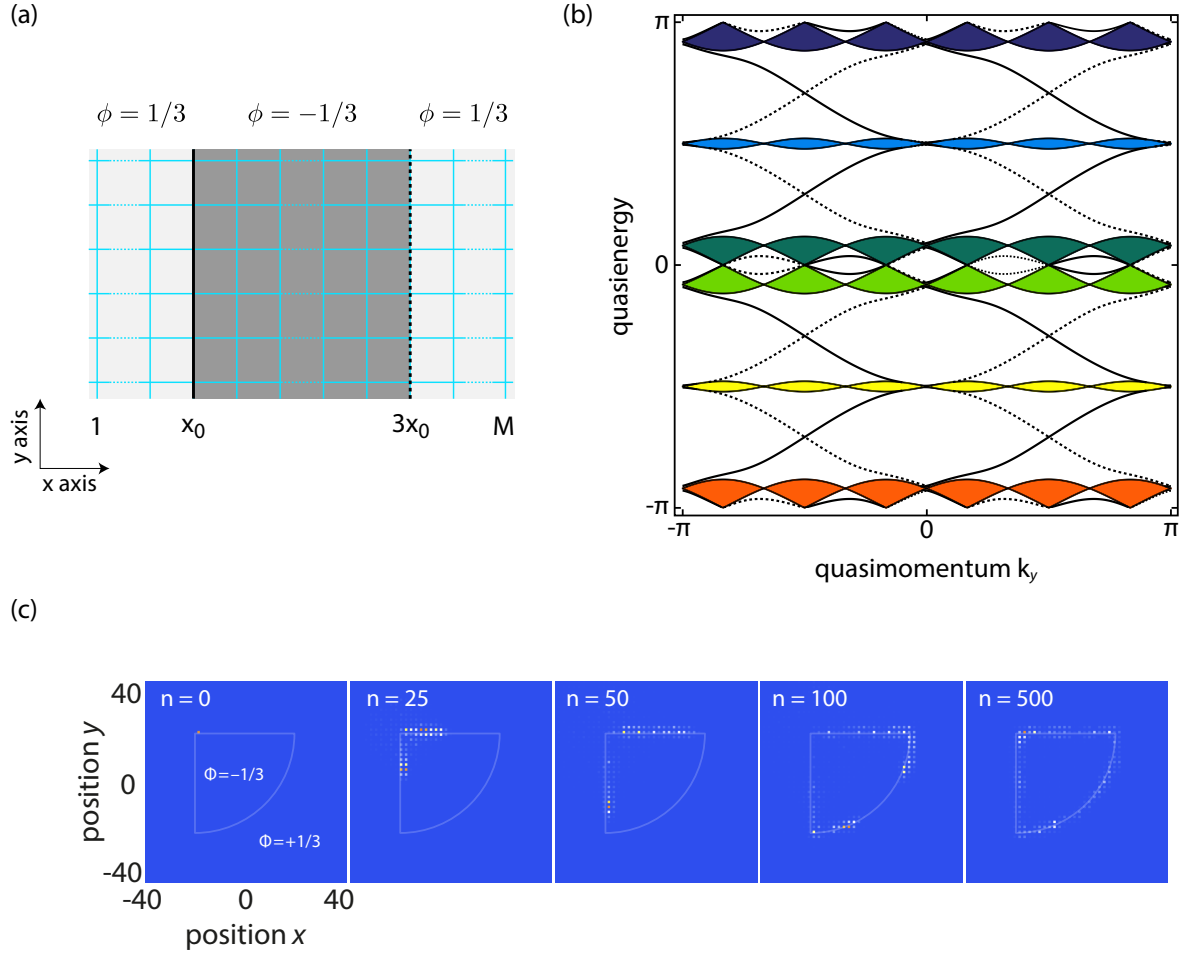
(a)

(b)

(c)

Figure 4.5: Quasienergy spectrum of the walk $\hat{W}_{2DM}$ in the presence of a strip shaped boundary along the y axis of the 2D lattice. (a) Schematic of the strip boundary which I implement to study the edge spectrum. The boundary maintains translational invariance of the problem in the y direction and breaks it the x direction. The magnetic field is pointing along the positive normal of the 2D lattice ($+B$) with $\phi = 1/3$ outside the strip, and is pointing in opposite direction ($-B$) with $\phi = -1/3$ inside the strip. (b) The quasienergy spectrum computed in the presence of this boundary. The filled bands represent the bulk spectrum and the states propagating in the gaps represent the edge spectrum. The solid (dashed) lines represent the edge states localized on the left (right) edge of the strip (shown in (a)). The magnetic field in the two domains is pointing in opposite direction, which changes the sign of the Chern numbers of the bands. Hence the number of edge states in each gap of the spectrum is twice of their respective gap invariant (shown in fig. 4.2). (c) Demonstrating the robustness of these TP edge states against spatial deformation and its propagation along the whole length of the boundary while remaining exponentially localized to it. Probability density (maximum, intermediate and minimum values are indicated by orange, white and blue colors respectively), at different time steps n, of a walker initially localized at the top left corner of the closed boundary that separates two distinct non-trivial topological phases. The flux ratio (ϕ) is ($-1/3$) inside the island, and ($1/3$) outside. These simulations are carried out for realistic parameters of the experiment, i.e. for a simple lattice (see fig. 4.8) with the synthetic magnetic field simulated by the proposal given in sec. 4.3. The relative shift between the lattice and the intensity profile is kept to 0.5, for which the quasienergy gap width is maximum, as shown in fig. 4.8.
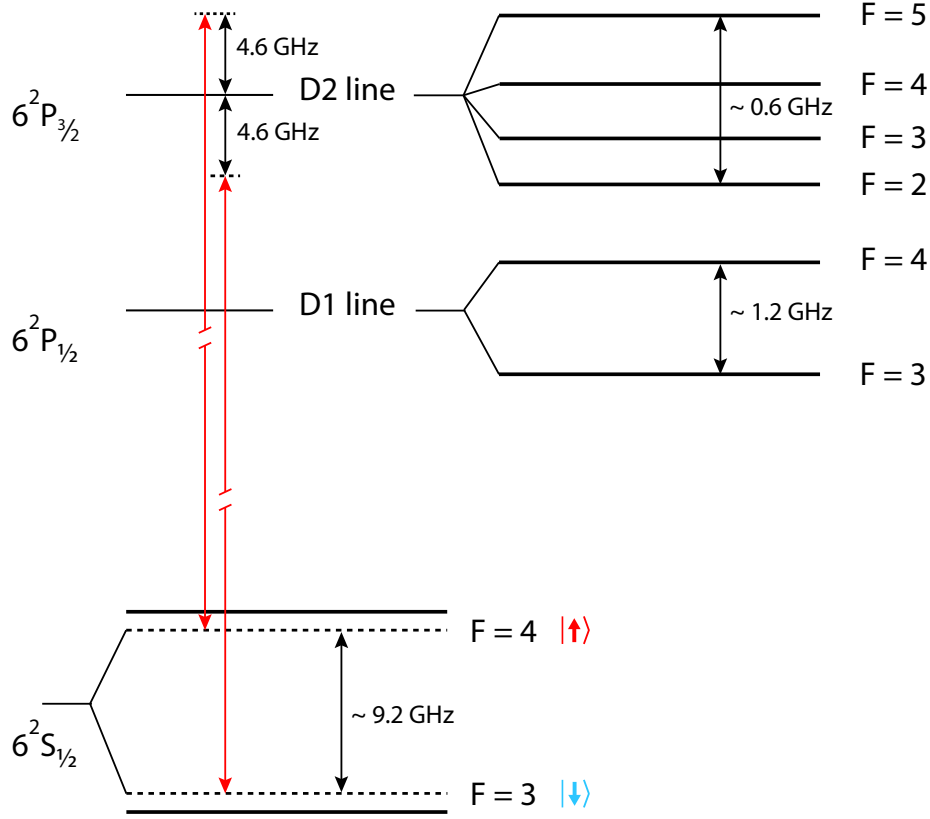
Figure 4.6: Schematic of the cesium atom's fine and hyperfine structure. A laser beam, detuned by ~ 4.6 GHz from the D2 line is used (blue detuned with respect to the spin-up and red detuned with respect to the spin-down state). The two spin states get light-shifted by an equal magnitude but opposite in sign resulting in a spin-dependent optical dipole potential for the atom. Because of the detuning of the laser, the contribution of the small hyperfine splitting to the optical dipole potential and scattering rate can be ignored.

the lattice. To implement uniform global coin operations, we use microwave radiation at 9.2 GHz that is resonant with the splitting between the two spin states (for details on experimental setup, we refer the readers to [91, 92]). To include the effects of a magnetic field in the QW experiment, we need to project spatial patterns of light field on atoms to generate and modulate ac stark shifts for the two spin states. In this way we engineer the spin-dependent force $\hat{F}$ defined in eq. (4.1). This is implemented in a stroboscopic manner, i.e. first the walker is shifted in the lattice and then the spin-dependent force is turned on for a short period, resulting in a spin-dependent phase shift of the walker wavefunction. In contrast to other cold atoms realizations, where the implementation of extra phase is coupled to the tunneling of an atom in the lattice, here they are realized in two separate operations illustrated schematically in fig. 4.1 (b).

We make use of the position and spin-dependent optical dipole potential of the pseudo spin states to generate a spin-dependent force ($\hat{F}_{\text{exp.}}$), which is given by

$$\hat{F}_{\text{exp.}} = \sum_r |r\rangle \langle r| \otimes \begin{pmatrix} e^{i\left(\frac{U_{\text{dip.}}^{\uparrow}(r)t}{\hbar}\right)} & 0 \\ 0 & e^{i\left(\frac{U_{\text{dip.}}^{\downarrow}(r)t}{\hbar}\right)} \end{pmatrix}. \tag{4.5}$$
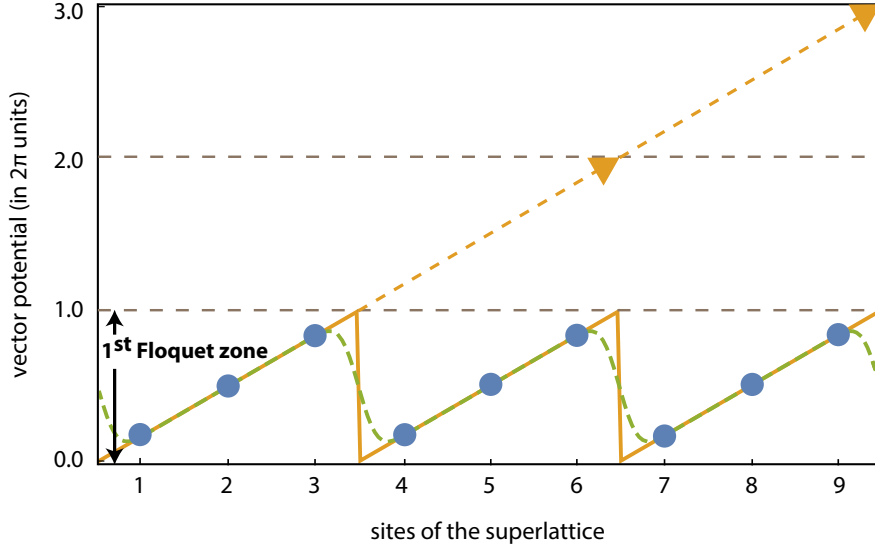
Figure 4.7: Spatial profile of the engineered synthetic gauge potential (intensity of the laser has the same profile) along the x axis of the superlattice. For the chosen gauge of the vector potential, the profile is independent of the y coordinate. Due to the 2π-periodicity of the imprinted phase, the linear ramp of the intensity and hence that of the gauge potential (shown by the dashed line extending beyond the first Floquet zone) is folded to the first Floquet zone. Inside the first Floquet zone, the solid saw-tooth line represents the ideal profile of the vector potential that is required, and the dashed line (after taking into account the effects of the imaging system) is the one which the atoms will experience. The small filled circles, lying on the linear slope of the saw-tooth profile, represent the atoms' positions in the superlattice.

Here $U_{\text{dip.}}^{\uparrow}(r)$ ($U_{\text{dip.}}^{\downarrow}(r)$) is the position-dependent optical dipole potential of the spin-up (spin-down) state of a Cs atom, t is the time duration for which the force operator should be applied and $\hbar$ is the reduced Planck's constant. When a Cs atom is dressed in a laser field that is detuned ($\sim 4.6\,\text{GHz}$) from the D2 line (852 nm), the two spin states get light-shifted generating an optical dipole potential for the atom. The dipole potential for the two spin states can be written as [101],

$$U_{\text{dip.}}^{\uparrow}(r) \simeq \frac{\pi c^2}{2}\left[\left(\frac{\Gamma_{\text{D2}}}{\omega_{\text{D2}}^3}\right)\left(\frac{2}{2\pi c(\frac{1}{\lambda}-\frac{1}{\lambda_{\text{D2}}})+\frac{2\pi\Delta_{\text{Hyp.}}}{2}}\right)\right.$$
$$\left.+\left(\frac{\Gamma_{\text{D1}}}{\omega_{\text{D1}}^3}\right)\left(\frac{1}{2\pi c(\frac{1}{\lambda}-\frac{1}{\lambda_{\text{D1}}})+\frac{2\pi\Delta_{\text{Hyp.}}}{2}}\right)\right]I(r), \tag{4.6}$$

$$U_{\text{dip.}}^{\downarrow}(r) \simeq \frac{\pi c^2}{2}\left[\left(\frac{\Gamma_{\text{D2}}}{\omega_{\text{D2}}^3}\right)\left(\frac{2}{2\pi c(\frac{1}{\lambda}-\frac{1}{\lambda_{\text{D2}}})-\frac{2\pi\Delta_{\text{Hyp.}}}{2}}\right)\right.$$
$$\left.+\left(\frac{\Gamma_{\text{D1}}}{\omega_{\text{D1}}^3}\right)\left(\frac{1}{2\pi c(\frac{1}{\lambda}-\frac{1}{\lambda_{\text{D1}}})-\frac{2\pi\Delta_{\text{Hyp.}}}{2}}\right)\right]I(r) \tag{4.7}$$

Here c is the speed of light, Γ_{D2} (Γ_{D1}) is the scattering rate of the D2 (D1) line, ω_{D2} (ω_{D1}) is the transition frequency from the ground state to the excited state of D2 (D1) transition, λ_{D2} (λ_{D1}) is wavelength

corresponding to the D2 (D1) transition, λ is the wavelength of the laser being used, $\Delta_{\text{Hyp.}}$ is the hyperfine splitting of the ground state and $I(r)$ is the intensity of the laser field. Due to the detuning of the laser field much larger than the hyperfine splitting of the D1 and D2 lines, we have neglected the contribution of this splitting to the dipole potential and to the scattering rate, as schematically shown in fig. 4.6. The optical dipole potential for the two spin states is equal in magnitude but has opposite sign which results in opposite phase shifts for the two spin states. We can write the phase shift for the two spin states in terms of the mean and difference values of the optical dipole potentials in the following way:

$$\Delta U_{\text{dip.}}(r) = U^{\uparrow}_{\text{dip.}}(r) - U^{\downarrow}_{\text{dip.}}(r), \quad \overline{U}_{\text{dip.}}(r) = (U^{\uparrow}_{\text{dip.}}(r) + U^{\downarrow}_{\text{dip.}}(r))/2,$$
$$\implies \quad U^{\uparrow}_{\text{dip.}}(r) = \overline{U}_{\text{dip.}}(r) + \Delta U_{\text{dip.}}(r)/2,$$
$$U^{\downarrow}_{\text{dip.}}(r) = \overline{U}_{\text{dip.}}(r) - \Delta U_{\text{dip.}}(r)/2. \tag{4.8}$$

Using these definitions, eq. (4.5) can be rewritten as,

$$\hat{F}_{\text{exp.}} = \sum_r |r\rangle \langle r| \otimes e^{\left(\frac{\overline{U}_{\text{dip.}}(r)t}{\hbar}\right)} \begin{pmatrix} e^{i\left(\frac{\Delta U_{\text{dip.}}(r)t}{2\hbar}\right)} & 0 \\ 0 & e^{-i\left(\frac{\Delta U_{\text{dip.}}(r)t}{2\hbar}\right)} \end{pmatrix}. \tag{4.9}$$

The factor $\overline{U}_{\text{dip.}}(r)$ results in a position-dependent global phase which is similar for both spin states. This generates an artificial electric field for the atom, which is similar to case already studied in our group [102]. The effects of $\hat{F}_{\text{exp.}}$ (in the form given in eq. (4.9)) will be interesting to study electromagnetic QWs; however, here we focus only on simulating artificial magnetic field and set $\overline{U}_{\text{dip.}}(r) = 0$. The phase $\Delta U_{\text{dip.}}(r)t/2\hbar$ plays the role of the vector potential for the neutral atom. The difference of the optical dipole potentials, and hence the phase shift for the two spin states, varies linearly with the intensity of the light field. By applying a linear intensity ramp, a linear gradient of the potential is generated that results in a spin-dependent force and hence a linear gradient of the phase shift for the atom. The spatial profile of the intensity is controlled by using a spatial light modulator (SLM). The scattering rate for the two spin states, for detuning much larger than the hyperfine splitting of the D1 and D2 lines, can be estimated as

$$\Gamma^{\uparrow}_{\text{scat.}} \simeq \frac{\pi c^2}{2\hbar} \left[\left(\frac{\Gamma^2_{\text{D2}}}{\omega^3_{\text{D2}}}\right)\left(\frac{2}{(2\pi c(\frac{1}{\lambda} - \frac{1}{\lambda_{\text{D2}}}) + \frac{2\pi\Delta_{\text{Hyp.}}}{2})^2}\right) \right.$$
$$\left. + \left(\frac{\Gamma^2_{\text{D1}}}{\omega^3_{\text{D1}}}\right)\left(\frac{1}{(2\pi c(\frac{1}{\lambda} - \frac{1}{\lambda_{\text{D1}}}) + \frac{2\pi\Delta_{\text{Hyp.}}}{2})^2}\right) \right] I(r), \tag{4.10}$$

$$\Gamma^{\downarrow}_{\text{scat.}} \simeq \frac{\pi c^2}{2\hbar} \left[\left(\frac{\Gamma^2_{\text{D2}}}{\omega^3_{\text{D2}}}\right)\left(\frac{2}{(2\pi c(\frac{1}{\lambda} - \frac{1}{\lambda_{\text{D2}}}) - \frac{2\pi\Delta_{\text{Hyp.}}}{2})^2}\right) \right.$$
$$\left. + \left(\frac{\Gamma^2_{\text{D1}}}{\omega^3_{\text{D1}}}\right)\left(\frac{1}{(2\pi c(\frac{1}{\lambda} - \frac{1}{\lambda_{\text{D1}}}) - \frac{2\pi\Delta_{\text{Hyp.}}}{2})^2}\right) \right] I(r). \tag{4.11}$$

The scattering rate can be kept lower by using a large detuning at a given intensity [101]. The strength and direction of the simulated field can be tuned by changing the intensity profile of the laser beam. By using this technique, a uniform and strong magnetic field can be generated which does not require any rectification in contrast to some of the earlier proposals [33, 35].

4.3.2 Sawtooth Intensity Profile

To simulate magnetic field with $\phi = 1/3$ corresponding to the Landau gauge $\vec{A}(x) = (0, 2\pi\phi x, 0)$, the intensity profile of the laser field is dialed in such a way that the phase shift, resulting from the optical dipole potential, has a gradient $2\pi/3$ in the x direction of the lattice. However, a linear slope of intensity over the whole lattice would require high intensities (for higher values of x), which will in turn result in an increased photon scattering rate as it is clear from equations (4.10), (4.11). This will results in heating of atoms and decoherence in the system [91], which we want to avoid. This problem is more significant for generating a strong magnetic fields, as weak fields do not suffer from this problem as long as the walker's position remain in the proximity of the origin. However, by taking advantage of the Floquet nature of the system, this problem can be circumvented. Since the imprinted phase shift ($\Delta U_{\text{dip.}}(r)t/2\hbar$) due to the light field repeats itself every third lattice site, a saw-tooth profile of the intensity resulting in $\Delta U_{\text{dip.}}(r)t/2\hbar$ mod 2π can be used. This is shown in the first Floquet zone of fig. 4.7. This has the advantage of generating the same magnetic field as the linear slope does over the whole lattice, without going to the high intensity regime and hence the scattering of photons from atoms can be kept lower. Numerical simulations, assuming $\lambda = \lambda_{\text{D2}} = 852$ nm, show that the operator (eq. (4.9)) can be applied in a time below $10\,\mu$s, which is much shorter than the decoherence time of the system. The numerically estimated scattering probability of photons per operation is 1%. This could be strongly attenuated by devising a scheme for 2D state-dependent transport with the quantisation axis perpendicular to the lattice.

In experiments, the spatially varying intensity profile generated by an SLM passes through the objective of the imaging system before illuminating the atoms. The light field intensity profile experienced by the atoms is the convolution of the intensity profile generated by the SLM and the point spread function of the imaging system. The solid saw-tooth profile shown in the first Floquet zone of fig. 4.7 is the ideal intensity profile intended to shine onto the atoms. The atoms will experience the intensity pattern shown by the dashed curve in the first Floquet zone, which is the result of the convolution of the ideal intensity profile and a gaussian function (approximation of experimentally measured point spread function of the imaging system). One of the experimental challenges is to properly align the intensity profile of the laser beam with the lattice so that an atom at a particular site of the lattice is illuminated with the required field. Particularly, falling slopes of the intensity profile (gauge potential) should not be at the position of a lattice site, otherwise an atom at that position will experience a non-uniform magnetic field leading to the deformation of the quasienergy spectrum shown in fig. 4.2. Under certain amount of mismatch (relative shift of intensity pattern with respect to the lattice), this deformation is small and the topological structure of the quasienergy bands is preserved. However, for sufficiently large amount of mismatch the deformation is large enough to close the quasienergy gaps leading to a topological phase transition.

In fig. 4.8, we quantify the deformation of the quasienergy spectrum of the magnetic QW. We examine the gap width of the spectrum while shifting the saw-tooth intensity profile with respect to the lattice through one complete lattice constant. The results show that for generating the desired synthetic magnetic field, the mismatch should be kept at a particular value, for which the quasienergy gap width is maximum. One way to make the experiment more robust against alignment errors is to use superlattices, i.e. to use only every nth site of the optical lattice instead of every second lattice site. This can be achieved by using the state-dependent transport, where each individual spin state can be coherently transported over nth lattice sites in a controlled manner. Mathematically, this means that to use $(\hat{S}_x)^n$ instead of $\hat{S}_x$. This reduces the alignment errors as the gap width becomes quite insensitive to relatively large range of mismatch (from 0.2 to 0.8, as shown in fig. 4.8).
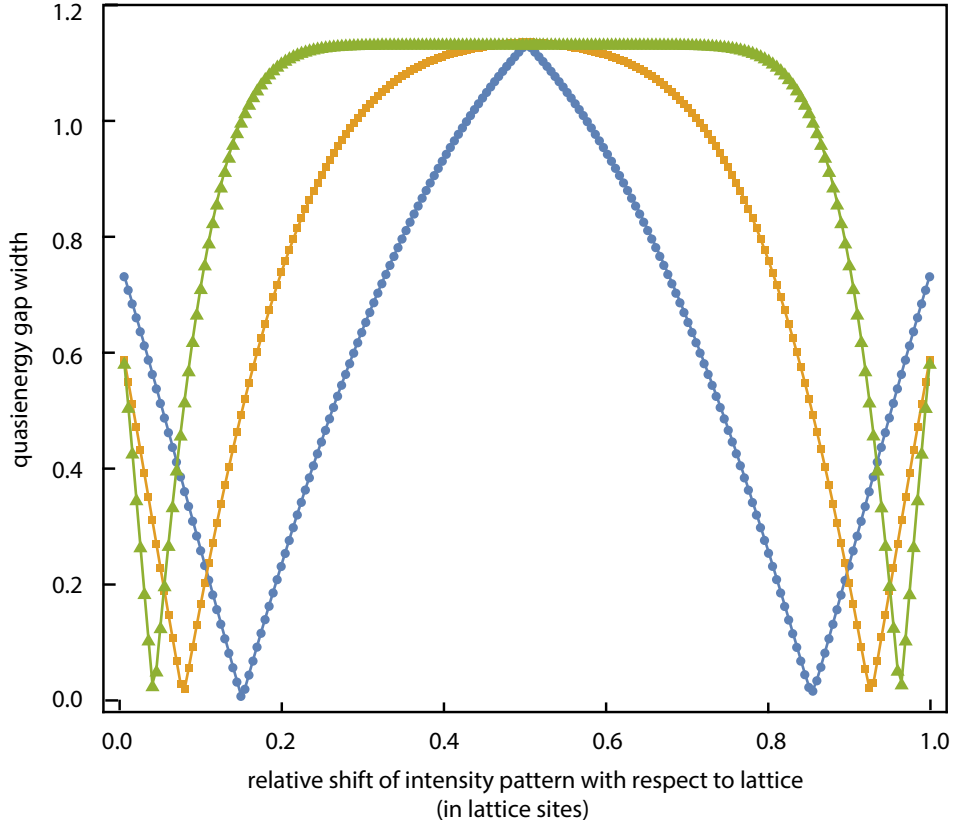
Figure 4.8: Quasienergy gap width of the bulk spectrum (gap width is same for all four gaps) depicted in fig. 4.2 vs. the relative shift between the intensity pattern of the laser beam generating the synthetic gauge potential and the lattice. The three different curves are for a simple lattice (•), a super lattice having lattice constant two times larger than the normal one (▪) and a super super lattice having lattice constant four times larger than the normal one (▲). Working with super and super super lattices is experimentally favorable as they are relatively robust against a wide range of mismatch between the atoms positions in the lattice and the required intensity of the light field.

4.3.3 Inhomogeneous Magnetic Field to Implement Topological Phase Boundaries

In order to implement the spatial boundaries, as defined in sec. 4.2 (separating two different topological domains having magnetic field B and $-B$), the intensity profile discussed in sec. 4.3.1 should be modified. In a region of the lattice where the magnetic field is B, the intensity profile remains as shown in fig. 4.7. The slope of the intensity profile and hence that of the gauge potential is reversed in a region of the lattice where the magnetic field $-B$ is required. In our numerical study, I include the effects of the imaging system affecting the intensity pattern of the light field by carrying out a 1D or a 2D convolution, for implementing a straight boundary or a closed boundary. The edge spectrum computed in the presence of a strip-shaped boundary and the evolution of the edge modes along the closed boundary, shown in fig. 4.5 (b) and (c), are simulated under the realistic conditions of the experiment (by taking into account the finite optical resolution of the imaging system) mentioned here.

Conclusion and Outlook

In this chapter, I have shown with my numerical results that QWs of neutral atoms trapped in optical lattices provide an excellent platform for realizing flat-band Floquet Chern insulators. Our scheme has a number of unique advantages for exploring the physics of the strong-field regime. It allows for generating arbitrary landscapes of synthetic vector potentials giving the flexibility of changing the direction of the simulated magnetic field at ease. This is in turn important for creating different topological domains with sharp spatial boundaries along which TP edge states can be probed. Another unique advantage of our scheme is that it does not rely on laser-assisted tunneling and hence avoid the problem of high scattering rates and heating (although it still suffers from scattering with 1% probability per step operation). In QWs experiments, a neutral atom is delocalized through state-dependent transport which does not suffer form damping of tunneling rates. This makes it possible to work with super lattice potentials. The results presented here are for a single particle in a clean environment, however, it can be extended to study interactions-induced topological states and disorder effects. Theoretically, it has already been shown that interaction in QWs of two atoms in 1D lattice leads to the formation of stable molecular states [71]. In experiments, systems of neutral atoms trapped in optical lattices are celebrated for their high degree of controllability of particle-particle interactions, which can be exploited to investigate interaction-induced effects [103]. In the presence of disorder, scattering matrix approach (introduced in chap. 5) can be employed to investigate topological properties of the system.

Probing the Hofstadter Spectrum with Scattering in Magnetic Quantum Walks

Tʜᴇ Hofstadter spectrum (fig. 2.3) represents the energy spectrum of electrons moving in a 2D periodic potential in the presence of a perpendicular magnetic field. The corresponding energy bands and gaps form a fractal structure as a function of the magnetic field strength. Such complexity is a consequence of frustration in the system, which arises due to the competition between the characteristic length scales associated with the two quantizing fields, i.e. the magnetic length scale and the period of the 2D potential. Since its first appearance in 1976 [24], the Hofstadter spectrum has attracted much attention, not only due to its fascinating fractal structure, but also due to its connections to other physical phenomena in condensed matter systems, like quantum Hall phenomena. It is additionally a proof of the role that number theory and topology play in nature, which were previously considered as pure mathematical subjects [104]. At the time of its discovery, the experimental observation of the Hofstadter spectrum seemed unreachable due to the required magnetic field strength. In conventional solid-state materials (having a lattice constant of the order of 2Å), the magnetic field strength required to reach the interesting scenario of $\phi \sim 1$ is of the order of 10^5 T, which is not possible with the current available technology. Alternative approaches such as superlattices with considerably larger lattice constants [28, 105–108] and moiré superlattices [29, 109] have made it possible to experimentally access some of the properties of the Hofstadter spectrum. In these physical realizations, one of the main challenges is to avoid disorder that limits the resolution of the experimental measurements. Efforts have also been made in other systems where concepts similar to those in solid-state physics were investigated for the experimental demonstration of the Hofstadter-type spectrum [110, 111].

Ultracold atoms in optical lattices offer an excellent platform for simulating the Hofstadter spectrum, due to their disorder-free and controllable environment, along with the possibility to artificially synthesize strong magnetic fields. In fact, the Harper Hamiltonian has been realized with neutral atoms in optical lattices by generating an artificial magnetic field [39, 40]. So far, however, the corresponding band structure has not yet been observed. In this chapter, I present a numerical study of the scattering matrix approach in magnetic QWs of neutral atoms in optical lattices to probe the Hofstadter spectrum. I start with a brief introduction to the scattering matrix formalism (section 5.1) and employ it to compute the topological invariants of the magnetic QWs (section 5.2). The bands and gaps of the spectrum are identified from the transport properties, i.e. the transmission and reflection probabilities of a walker from the scattering region (section 5.3). The introduction contains the basic concepts used in this chapter and, therefore, it is not meant to be a thorough, self-contained analysis. For a rather comprehensive study of the scattering matrix formalism, I refer to [112] and other references mentioned in the following

paragraphs.

5.1 A Brief Introduction to Scattering Matrix Formalism

The scattering matrix formalism is one of the central tools necessary to describe transport phenomena at low temperatures, frequencies, and voltages [112]. An early version of this approach was used by R. Landauer [113] to study the residual resistivity problem in metals. As opposed to the approach used for dealing with electrical conduction (in which the electrical force was considered as the causative source and the resulting motion of charged particles as a response) here the conductor was considered as a target and the incident flux of charged particles as the causative agent. Subsequently this formalism got considerable attention in the study of disordered systems, where the conductance was formulated in terms of transmission and reflection probabilities [114–119].

In topological insulators with disorder (where the translation invariance is broken) the scattering matrix formalism is used as one of the alternative descriptions to the band theory. It provides an efficient tool for the evaluation of the topological invariants without requiring translational symmetry and the complete spectrum of the Hamiltonian (see e.g. section 5.2 for the evaluation of the topological invariants of the magnetic QWs). The scattering matrix approach provides a new framework for probing topological phases by relating topological invariants of a topological insulator (superconductor) directly to its electrical (thermal) conduction, which are experimentally accessible observables [120–123].

In the following, I briefly introduce the scattering matrix in 2D, following a similar treatment as the ones given in [112, 121]. Let us consider a phase coherent scattering region subjected to disorder (the transport properties of which are required to be probed) that is connected to two reservoirs through identical ideal leads (see scheme in fig. 5.1). The leads are free of disorder and are used to define the basis for the scattering matrix of the scattering region. In the lead region, particles travel freely and can be described by plane waves along the x axis. In the case of a mesoscopic sample as a scattering region, the wave function of an electron in the lead regions at the Fermi energy is written (in the basis states) as,

$$\Psi_i^{\pm}(x,y) = \Phi_i(y)e^{\pm ik_i x}, \tag{5.1}$$

with $\Phi_i(y)$ being the transverse part of the wavefunction and k the wavenumber along the translational invariant direction (which corresponds to the x-axis here). The subscript i is a positive integer with values from 1 to N. It represents propagating modes that are also known as scattering channels. For example, an electron propagating in the lead region with a given wavenumber k and transverse wavefunction $\Phi_i(y)$ constitute a single scattering channel. The wave function is normalized to carry unit current. Particles propagating in the lead region and incident on the scattering region from both sides are expressed in the above-mentioned basis by a vector of coefficients

$$\Psi^{in} = (a_1^R, a_2^R, ..., a_N^R, b_1^L, b_2^L, ..., b_N^L)^T. \tag{5.2}$$

The coefficients (a_i, b_i : for $i = 1, 2, \ldots, N$) stand for the propagating modes in the left and right lead respectively. The superscripts R and L stand for the direction of propagation (right and left) and T for transposition. Similarly, particles which are leaving (reflected or transmitted) the scattering region on both sides are characterized by vector of coefficients

$$\Psi^{out} = (a_1^L, a_2^L, ..., a_N^L, b_1^R, b_2^R, ..., b_N^R)^T. \tag{5.3}$$

The scattering matrix S relates the incoming vector Ψ^{in} to the outgoing vector Ψ^{out} such that

Figure 5.1: Schematic illustration of a general scattering setting. The system is a phase-coherent disorder sample (scattering region, dark grey), the transport properties of which are to be probed. This is connected to two ideal leads (light grey) on its left and right sides. The modes of each lead are labeled by a and b, and their corresponding directions by R and L. The color coding shows the incoming (red, solid arrows) and outgoing (blue, dashed arrows) modes.

$$\Psi^{\text{out}} = \mathcal{S}\Psi^{\text{in}}. \tag{5.4}$$

It is clear that $\mathcal{S}$ is a $2N \times 2N$ matrix and has the block structure

$$\mathcal{S} = \begin{pmatrix} r & t' \\ t & r' \end{pmatrix}, \tag{5.5}$$

where r (r') is a $N \times N$ matrix (reflection matrix) containing the probability amplitudes for the particle incident on the scattering region from the left (right) lead being reflected back to the left (right). The matrix t (t') (transmission matrix) contains the probability amplitudes for the particle in the left (right) lead being transmitted to the right (left) after scattering. The scattering matrix $\mathcal{S}$ is unitary, i.e. $\mathcal{S}^\dagger = \mathcal{S}^{-1}$, which follows from the particle-current conservation. We consider that the incoming and outgoing modes are equal and normalized to carry unit current. This implies that the current coming to the system (scattering region) must be equal to the current leaving the system. In mathematical form, this reads

$$\begin{aligned} |\Psi^{\text{out}}|^2 &= \Psi^{\text{out}\dagger}\Psi^{\text{out}} \\ &= \Psi^{\text{in}\dagger}\mathcal{S}^\dagger\mathcal{S}\Psi^{\text{in}} \\ &= |\Psi^{\text{in}}|^2 \end{aligned} \tag{5.6}$$

where eq. (5.4) and the particle current conservation $\mathcal{S}^\dagger\mathcal{S} = \mathbb{1}$ have been used. The unitarity of the scattering matrix is important for the numerical stability of transport calculations [124]. In the absence of other symmetries (TRS, PHS, or CS), unitarity is the only constraint on the scattering matrix. The presence of other symmetries in the scattering region impose additional constraints (which can be found in [112, 121]).

Various transport properties can be determined from the transmission block of the scattering matrix. For example, the electrical conductance G of a mesoscopic sample (at zero temperature) can be determined from the sum of the transmission probabilities ($\text{tr}(t\,t^\dagger)$) with the Landauer formula [113],

$$G = G_0\,\text{tr}(t\,t^\dagger) = G_0\,\text{tr}(t't'^\dagger), \tag{5.7}$$

where G_0, the conductance quantum, is equal to Q^2/h for the electrical transport.

Transfer Matrix

Another equivalent description of the scattering region (disordered sample) can be given in terms of the so called transfer matrix formalism. The transfer matrix, in contrast to the scattering matrix, relates the coefficients of states in the left lead to those in the right lead. For a state of a particle in the left lead, the coefficients can be written in a vector form in the following way:

$$\Psi^{\text{left}} = (a_1^R, a_2^R, ..., a_N^R, a_1^L, a_2^L, ..., a_N^L)^T. \tag{5.8}$$

The coefficients with superscript R are representing the incoming particle (traveling to right) and the one with L are for the reflected one (traveling to left). For a particle in the right lead, the coefficient vector is

$$\Psi^{\text{right}} = (b_1^R, b_2^R, ..., b_N^R, b_1^L, b_2^L, ..., b_N^L)^T. \tag{5.9}$$

Here the coefficients with the superscript R are for the reflected particle and the ones with L are referring to the incoming particle. By definition, the transfer matrix $\mathcal{M}$ can be written as

$$\Psi^{\text{right}} = \mathcal{M}\Psi^{\text{left}}, \tag{5.10}$$

which is a $2N \times 2N$ matrix. The transfer matrix has a convenient property of multiplicative composition rule. According to this rule, for a number of scattering regions connected in series by ideal leads, the transfer matrix can be written as the product of transfer matrices of the individual regions. The current conservation between the two sides of the scattering region imposes a pseudo-unitarity constraint on the transfer matrix, i.e.

$$D\mathcal{M}^{-1}D = \mathcal{M}^{\dagger}, \tag{5.11}$$

with D a diagonal matrix having $D_{ii} = 1$ for $1 \le i \le N$ and $D_{ii} = -1$ for $N < i \le 2N$. Despite the aforementioned advantages, the eigenvalues of the transfer matrix can take exponentially larger and smaller values, which can make numerical calculations with the transfer matrix unstable [124].

5.2 Computing Topological Invariants of the Magnetic Quantum Walks with Scattering Matrix Approach

Topological invariants of topological insulators can be related to their transport properties using the scattering matrix approach. The type of relation depends on the presence of certain symmetries (TRS, PHS or CS) in the system. In closed systems described by single-particle Hamiltonians, these symmetries are used for the classification of topological insulators and superconductors giving ten possible symmetry classes represented by Cartan labels [86, 87]. These symmetries impose additional constraints on the scattering matrix [125]. In each spatial dimension, five out of ten symmetry classes are in topologically non-trivial phases, which are characterized by different topological invariants. In the case of QWs, the walk protocol, the corresponding effective Hamiltonian, and the scattering matrix depend on the choice of a time frame (the notion of time is discussed in Chapter 3). As a result, the discrete symmetries and topological invariants of a walk protocol are also time-frame dependent. An explicit choice of the time frame should be made to investigate the discrete symmetries and topological invariants of a walk.

By adapting concepts and methods developed for time independent systems, the scattering matrix formalism has been used in 1D QWs to compute the topological invariants of the quasienergy spectrum [69, 126]. In contrast to the Hamiltonian-based approaches for computing the topological invariants, the scattering matrix approach requires much less information and hence is numerically more efficient [125].

For gapped QWs, the unitarity of the reflection matrix (in the limit of large system size) allows the definition of topological invariants for the five topologically non-trivial symmetry classes of the symmetry classification. These are summarized in [126], along with their relationship to the reflection matrices.

The magnetic QW has CS in a shifted time frame, as we show in Appendix E. The topological invariants $\nu \in \mathbb{Z}$ of such QWs are winding numbers assigned to the bulk quasienergy gaps [75, 93]. According to the bulk–boundary correspondence principle, ν is equal the net number of edge states crossing a gap, which the scattering matrix approach identifies as the winding number of the determinant of the reflection block (r) of $\mathcal{S}$. To compute this invariant, Let us consider the walk operator given by eq. (4.2) of Chapter 4:

$$\hat{W} = \hat{F}\hat{S}_y\hat{C}\hat{S}_x\hat{C},$$

with the magnetic field operator $\hat{F} = e^{iB\,x\,\sigma_z}$ (here $B = 2\pi\phi$). $\hat{S}_x$ ($\hat{S}_y$) shifts the walker along the x-axis (y-axis) of the lattice, and the coin operator $\hat{C}$ manipulates the internal state of the walker (see Chapter 4). As an example, I fix $\phi = p/q = 1/3$, for which the quasienergy spectrum is already shown in Chapter 4. The layout of the calculation is as follows:

1. Define and attach a semi-infinite lead[1] to the semi-infinite system;

2. Define the modes in the lead for a fixed transverse wavenumber k;

3. Find the scattering states: eigenstates of the walk with incidence from one mode in the lead;

4. Find the elements of the reflection matrix from the scattering states;

5. Repeat the above steps for several values of the transverse wavenumber k, and calculate the winding of the determinant of the reflection matrix.

In the following I present a detailed description of these steps.

Attaching a Lead to the System

We open up the walk, here referred to as "system" (equally called scattering region), by attaching a metallic "lead" to it as shown in fig. 5.2 (a). The "system" consist of all sites with $x \geq 0$ where the walker evolves with the walk operator (eq. (4.2)). The lead consist of all sites with $x < 0$ and is defined by modifying the unitary time step operator: for $x < 0$, both coins, shift $\hat{S}_y$, and magnetic field operators are replaced by identity operations $\mathbb{1}$. This construction maintains translation invariance along y, so the wavenumber k_y is conserved. The whole system can be treated as a 1D chain of sites along the x axis with twisted boundary conditions along the y axis with wavenumber k_y (as depicted in fig. 5.2 (b)).

For this setting of the walk, the coin, shift, and magnetic field operators (for $x < 0$) are modified in the following way:

$$\hat{C} = \sum_{x<0} \left(|x\rangle\langle x| \otimes |\uparrow\rangle\langle\uparrow| + |x\rangle\langle x| \otimes |\downarrow\rangle\langle\downarrow| \right) + \sum_{x\geq 0} |x\rangle\langle x| \otimes e^{-i\frac{\theta\,\sigma_y}{2}}, \qquad (5.12)$$

$$\hat{S}_y = \sum_{x<0} \left(|x\rangle\langle x| \otimes |\uparrow\rangle\langle\uparrow| + |x\rangle\langle x| \otimes |\downarrow\rangle\langle\downarrow| \right) + \sum_{x\geq 0} |x\rangle\langle x| \otimes e^{-ik_y\,\sigma_z}, \qquad (5.13)$$

$$\hat{F} = \sum_{x<0} \left(|x\rangle\langle x| \otimes |\uparrow\rangle\langle\uparrow| + |x\rangle\langle x| \otimes |\downarrow\rangle\langle\downarrow| \right) + \sum_{x\geq 0} |x\rangle\langle x| \otimes e^{iB\,x\,\sigma_z}. \qquad (5.14)$$

---

[1] In scattering matrix theory of electronic conduction, an electronic waveguide (or metallic wire) is usually called a lead. This supports incoming and outgoing modes for the scattering region. In our case, we define a region of the 2D lattice, where a walker is propagating freely, as a lead.
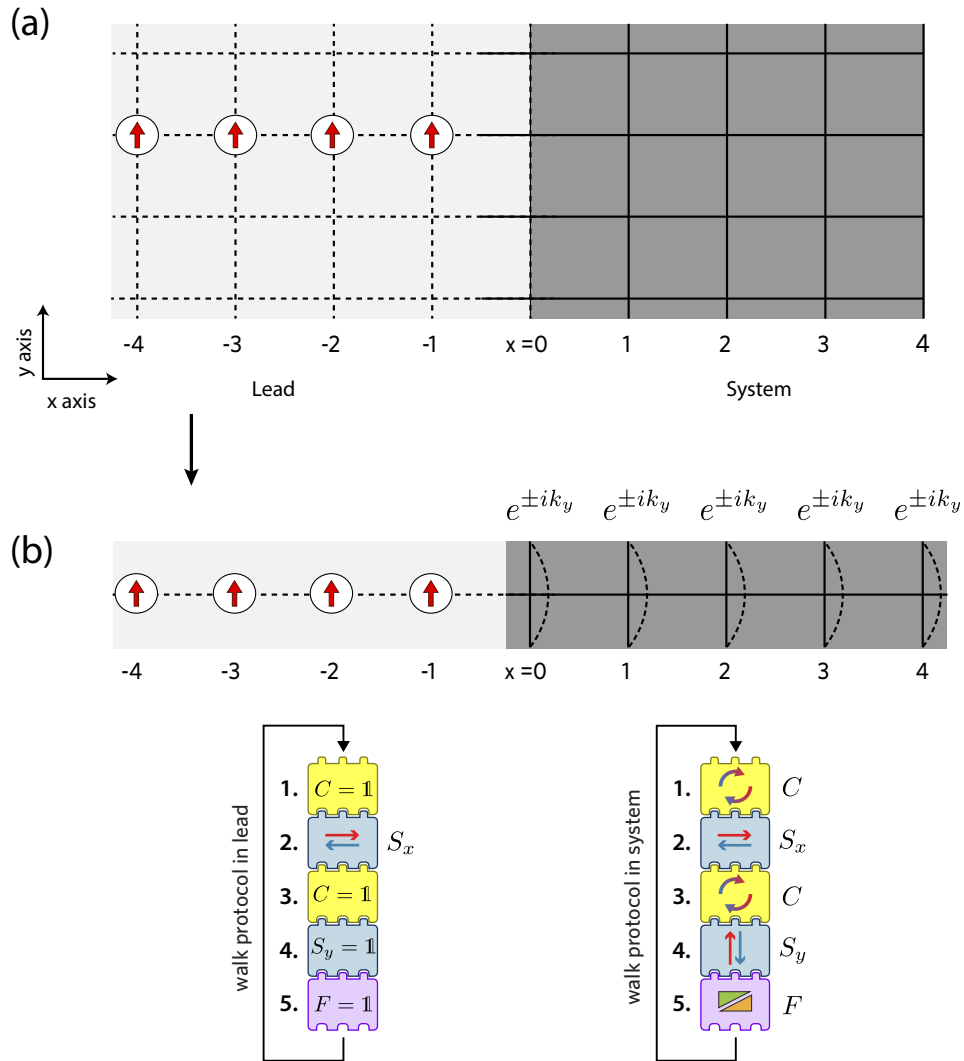
Figure 5.2: Schematic illustration of the scattering setting in QWs. (a) A "system" of magnetic QWs (dark grey lattice with solid lines) is connected to a single 2D ideal metallic "lead" (light shaded lattice with dashed lines) on its left. (b) Due to the translational invariance in the y direction, the system is reduced to a 1D chain of sites along x. In the lead there is no shift along y, while in the scattering region $\hat{S}_y$ is present which imprints a factor $e^{\pm ik_y}$ into the particle's wave function with sign "±" depending on the internal state. The connecting blocks represent the walk protocols in the lead and scattering regions. In the lead region only $\hat{S}_x$ is active, while the rest are set to identity. In the scattering region, all operators of the protocol are set to their normal operations.

Equation (5.12) shows that the coin angle is set to 0 in the lead region and θ in the system. In this definition, the spatial transition of the coin angle from 0 to θ is sharp, which is not possible in cold-atoms experiments due to the diffraction limit and other aberrations in the imaging system (the same applies for the magnetic field operator). For the model to be more realistic, we choose the error function to represent a smooth transition from the lead to the system. In this case, the coin angle and the magnetic field vary smoothly. In terms of the error function[2] ($\mathrm{erf}(x)$), eq. (5.12) and eq. (5.14) take the following form:

$$\hat{C} = \sum_{x=-\infty}^{+\infty} |x\rangle\langle x| \otimes e^{-i\frac{\theta}{2}\sigma_y \frac{1+\mathrm{erf}(Px)}{2}} \tag{5.15}$$

$$\hat{F} = \sum_{x=-\infty}^{+\infty} |x\rangle\langle x| \otimes e^{iB\,x\,\sigma_z \frac{1+\mathrm{erf}(Px)}{2}}. \tag{5.16}$$

Here P is a parameter used for tuning the smoothness of the transition.

Defining Modes in the Lead

The modes in the lead region are plane waves along x with i.e. $\varepsilon = k_x$. The incident and reflected modes in the lead are defined in the following way:

$$\|\Psi_{\mathrm{lead}}(\varepsilon)\rangle_{\mathrm{inc.}} = \sum_{x<0} e^{i\varepsilon\,x}|x,\uparrow\rangle, \tag{5.17}$$

$$\|\Psi_{\mathrm{lead}}(\varepsilon)\rangle_{\mathrm{ref.}} = \sum_{x<0} e^{-i\varepsilon\,x}|x,\downarrow\rangle. \tag{5.18}$$

The modes are normalized to carry unit current (indicated by the notation $\|\rangle$). Since the 2D problem is restricted to a 1D chain, there is a single incident (reflected) channel. For the incident mode $\|\Psi_{\mathrm{lead}}(\varepsilon)\rangle_{\mathrm{inc.}}$, the particle is considered to be in the spin-up state (in accordance to the definition of $\hat{S}_x$). The shift operator $\hat{S}_x$ evolves this state to the right in order to probe the scattering region. The reflected part of the wavefunction will travel to the left in the lead region and will be in the spin-down state.

Finding the Scattering States

To obtain the scattering matrix, it is required to find the scattering states. The scattering state ($\|\Psi_{\mathrm{scat.}}(\varepsilon, k_y)\rangle$) corresponding to the incident mode is an eigenstate of the walk operator, which can be written as

$$\|\Psi_{\mathrm{scat.}}(\varepsilon, k_y)\rangle = \sum_{n\in\mathbb{Z}} e^{i\varepsilon\,n}\hat{W}(k_y)^n|x,\uparrow\rangle. \tag{5.19}$$

---

[2] Error function is defined as

$$\mathrm{erf}(x) = \frac{1}{\sqrt{\pi}}\int_{-x}^{x} e^{-t^2}\,dt,$$

which gives

$$0 \le \mathrm{erf}(x) \le 1 \ \text{ if } \ x \ge 0$$
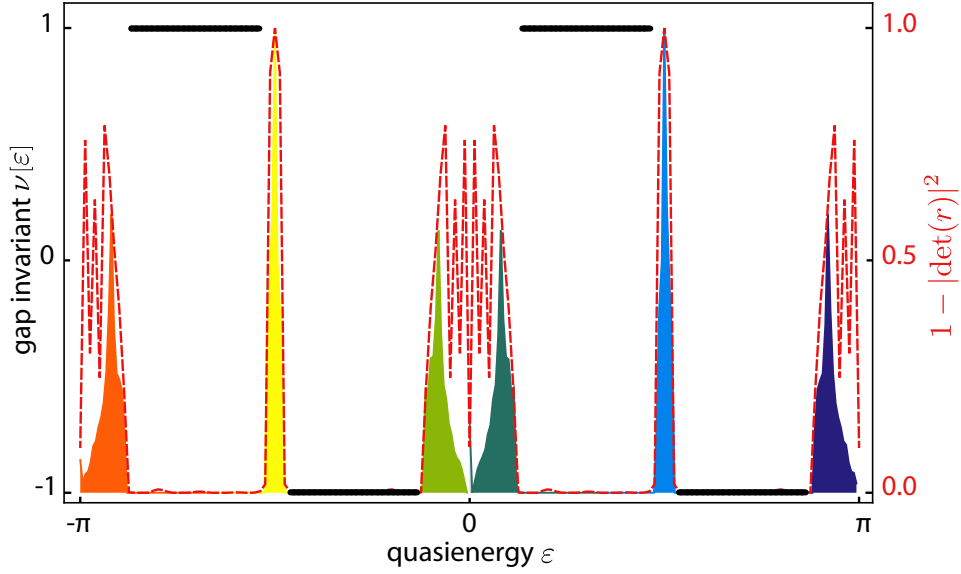$$-1 \le \mathrm{erf}(x) < 0 \ \text{ if } \ x < 0,$$

Figure 5.3: Topological invariants ν of the gaps of the magnetic QW (with $p/q = 1/3$) computed numerically with $L = 100$, $n_{\text{max.}} = 500$. The values of the invariant are indicated by the thick black lines, which changes somewhere in each bulk band. Transmission probabilities $(1 - |\det(r)|^2)$ are indicated by the red dashed line. Since the reflection (transmission) signal is also a function of the quasimomentum k_y, here I only show the signal for $k_y = -\pi/2$ which gives a very good contrast of the transmission signal for bands *vs.* gaps regions. The colored shadings represent DOS and are shown for the purpose of indicating the positions of each bulk band. The winding of the reflection matrix (topological invariant of the gap) reproduces changes somewhere in each bulk band.

This is an eigenstate of $\hat{W}$ with eigenvalue $e^{i\varepsilon}$, as can be checked by substitution. It contains the incident mode $|\Psi_{\text{lead}}(\varepsilon)\rangle_{\text{inc.}}$, since

$$\|\Psi_{\text{lead}}(\varepsilon, k_y)\rangle_{\text{inc.}} = \sum_{n<0} e^{i\varepsilon \, n} \hat{W}(k_y)^n |x, \uparrow\rangle \tag{5.20}$$

as can be seen by comparing with (5.17).

Constructing the Reflection Matrix

In general, the element r_{jl} of the reflection matrix is the coefficient of the jth scattered mode in the scattering state originating from the lth incident mode. This can be written as

$$r_{jl}(\varepsilon, k_y) = \langle j, \downarrow| \sum_{n=1}^{\infty} e^{i\varepsilon \, n} \hat{W}(k_y)^n |l, \uparrow\rangle, \tag{5.21}$$

for $j, l \in \mathbb{N}$, $1 \le j, l \le y_{\text{max.}}$. In the considered specific case (1D chain of sites along x) $y_{\text{max.}} = 1$, hence the reflection matrix has the dimension 1×1. The reflection matrix can be numerically obtained by directly evaluating eq. (5.21). As pointed out in [126], the scattering matrix is determined by initializing a particle in an incoming mode of a lead region and evolving it in time until it enters an outgoing mode. This renders most of the most of the lattice sites irrelevent for the numerical calculations, as it is not explored by the particle in a single step of the walk. Therefore, for the numerical calculations the 1D chain along the x axis can be truncated to a finite size chain. I consider the scattering to have total L sites

along x, i.e. $x = 0, 1, \ldots, L$, with an absorbing boundary condition at $x = L$. For the lead, only those sites are needed which are non-trivially involved during one time step of the walk evolution. Since the walk protocol consists of only one shift operator ($\hat{S}_x$), then a particle initially localized on a single site of the lead close to the system's boundary, i.e. $|x = -1, \uparrow\rangle$, can enter the scattering region in one time step of the walk. Similarly, a particle in the scattering region can at most explore only one site ($x = -1$) of the lead region in one time step. This one site of the lead is the only site non-trivially involved in the scattering during one step of the walk. On the remaining sites of the lead, the particle follows the trivial evolution of the lead region which takes no part in the scattering and hence are not relevant for the numerical calculations. Therefore, I consider a single site lead which is seamlessly connected to the system. The sum over n is also truncated to some $n_{\text{max.}}$. Thus the shift operator $\hat{S}_x$, for this truncated problem, takes the following form,

$$\hat{S}_x = \sum_{x=-1}^{L-1} \left(|x + 1, \uparrow\rangle\langle x, \uparrow| + |x, \downarrow\rangle\langle x + 1, \downarrow| \right), \tag{5.22}$$

which annihilates states $|x = -1, \downarrow\rangle$ and $|x = L, \uparrow\rangle$. Both L and $n_{\text{max.}}$ can be simply chosen large enough in order to have a better reflection signal.

Computing the Winding of the Determinant of the Reflection Matrix

From the reflection matrix r (which is a 1×1 matrix in the considered setting of the problem), the winding number of its determinant will be the scattering invariant:

$$\nu[\varepsilon] = \frac{1}{2\pi i} \oint_{-\pi}^{\pi} dk_y \frac{d}{dk_y} \log \det r(\varepsilon, k_y) \tag{5.23}$$

$$= \frac{1}{2\pi} \lim_{N \to \infty} \sum_{j=1}^{N} \arg \frac{\det r(\varepsilon, k_{j+1})}{\det r(\varepsilon, k_j)}.$$

The numerically obtained values of the invariants are shown in fig. 5.3, which are in agreement with the net number of edge states shown fig. 4.5 (b) of Chapter 4.

5.3 Probing the Hofstadter Spectrum with Scattering Matrix Approach

I now use the scattering setting in 2D magnetic QWs to probe the Hofstadter spectrum. The idea is to initialize a walker in the lead region (where it propagates freely), impinge it on the scattering region, and compute its reflection and transmission probabilities. A walker with quasienergy tuned to the bands of the scattering region will be transmitted with high probability. Otherwise, it will be reflected if its quasienergy is tuned to that of the gap. Hence the resultant reflection (transmission) probabilities contain signatures of the energy spectrum of the scattering region. Here, I will compute just the reflection probabilities, since they also provides the transmission probabilities.

The setting is the same as described in section 5.2, with the difference that the lead region is now extended to a finitely large number of sites. The reason is to evolve a walker, initialized in the lead region, for a large number of time steps n without projecting it into a lead state in the intermediate steps of the evolution. The number of time steps is chosen large enough so that the walker either completely reflected or transmitted. The final state of the walker is then projected to a plane wave state in the lead region with

spin component down to get the reflection probability as a function of the quasienergy. The detailed steps are shown in the following.

5.3.1 Computing the Reflection Probabilities

First Method: Using an Extended Lead

I start with a walker localized on a single site in the lead, lying close to the scattering region, i.e. $x = -1$, such that the normalized initial state of the walker can be written as

$$|\Psi_i\rangle = |x = -1, \uparrow\rangle. \tag{5.24}$$

This initial state is then evolved by applying the magnetic QW operator of eq. (4.2) (modified for the scattering setting, i.e. using the operators given in eqs. $(5.12 - 5.14)$) for a given rational value of the flux ratio (ϕ). The initial state is evolved for a large number of time steps to get the scattering state. The maximum number of time steps and size of the lead are chosen large and comparable to each other so that the reflected part of the scattering state do not reach the boundary of the opposite lead region ($x \to -\infty$). The normalized scattering state of the walk is,

$$|\Psi_{\text{scat.}}(k_y)\rangle = \hat{W}^{n=n_{\text{max.}}}(k_y) |\Psi_i\rangle. \tag{5.25}$$

This state is projected to a plane wave state (with spin down) along the x axis in the lead to get the reflection probabilities. A plane wave state in the lead is defined as

$$|\Psi_{\text{lead}}(k_x)\rangle = \sum_{x=-x_{\text{max.}}}^{-1} e^{-ik_x |x+1|} |x, \downarrow\rangle, \tag{5.26}$$

and its reflection probability is

$$R(k_x = \varepsilon, k_y) = \left| \langle \Psi_{\text{lead}}(k_x) | \Psi_{\text{scat.}}(k_y) \rangle \right|^2. \tag{5.27}$$

In the lead, the walker is propagating freely and hence its quasienergy is proportional to its quasimomentum k_x. Figure 5.4 shows the transmission probabilities ($1 - R(k_x = \varepsilon, k_y)$) along with the bulk bands for four different values of $\phi = p/q$. The bulk bands are plotted in order to give an indication of the bands' position. It is clear that the transmission probabilities, beside its dependence on quasienergy, also depend on quasimomentum k_y due to the dispersion of the bulk spectrum. For a given value of p/q, k_y is scanned through the whole BZ (in discrete steps) and the transmission signal is monitored. The selected k_y values are those for which the transmission signals show a better contrast amongst bands *vs.* gaps regions.

Second Method: Using a Single-Site Lead

The reflected part of the scattering state can be reconstructed by following an alternative numerical method. The purpose is to carry the trivial evolution (free propagation) of walker's wavefunction in the lead without using the walk operator. I consider a single site lead and start with a particle in spin-up state localized on this site ($x = -1$). After each step of the walk, the final state is projected to the initial state (but with spin-down) in the lead. This projection thus excludes the transmission part of the scattering state. Each projection is then trivially evolved in the lead (without using the walk operator) for the corresponding remaining time steps of the walk evolution (like it would have evolved by the walk
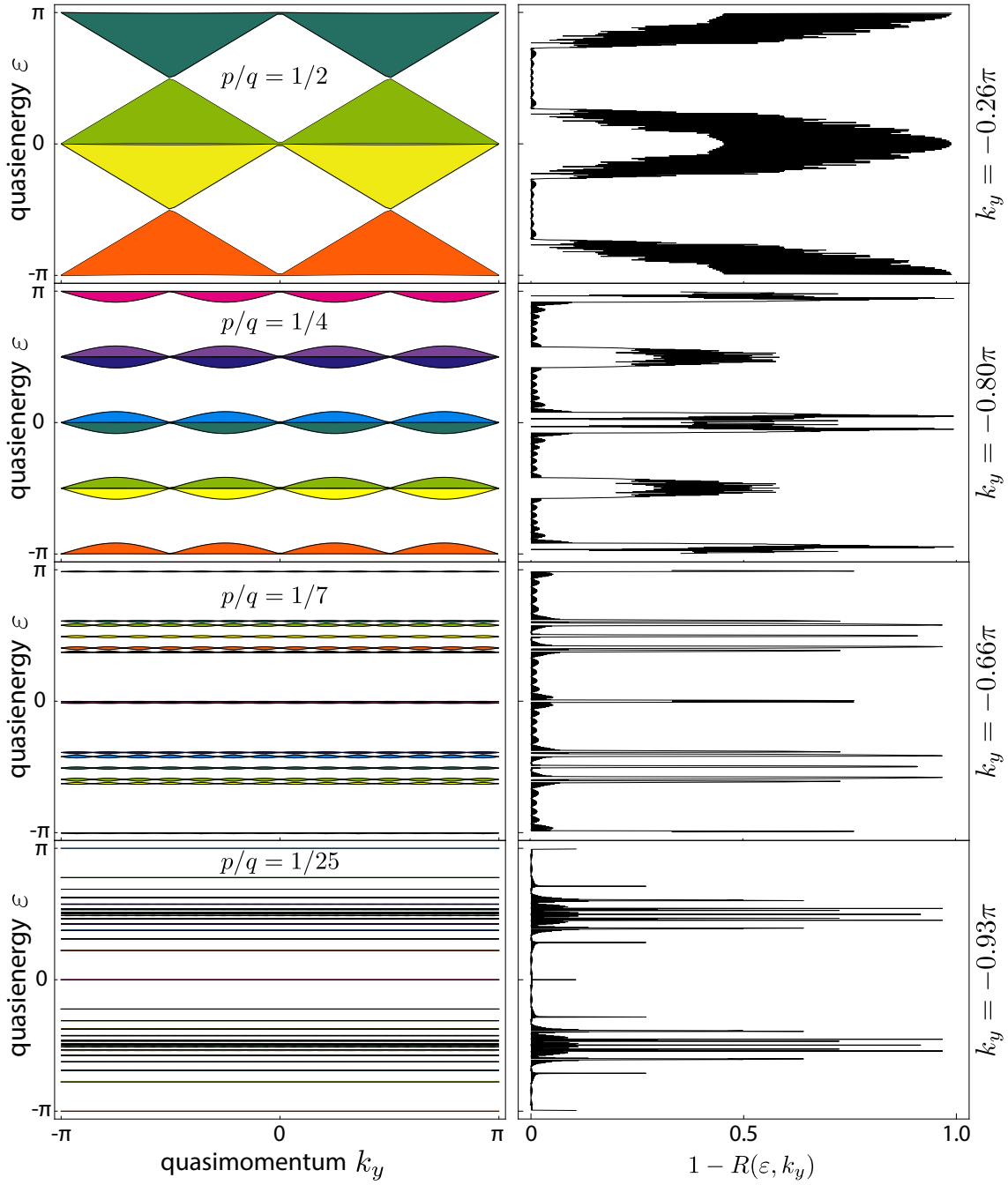
Figure 5.4: Bulk bands of the magnetic QW defined in eq. (4.2) (left panel) and the resulting transmission probabilities (right panel) computed using the scattering matrix approach. From top to bottom, the flux ratio is $\phi = p/q = 1/2, 1/4, 1/7$ and $1/25$. For odd values of q, there is a single peak in the transmission signal for each isolated single band (except at at $\varepsilon = 0$ where band gap closes). For even values of q, the bands are making groups by closing the gap at different values of ε, hence, there is a single peak in the transmission signal corresponding to each single group of bands. For higher values of q (both even and odd), the peaks in the transmission signals are not fully resolved. Due to the fact that the transmission probability is not only a function of the quasienergy (ε) but is also function of the quasimomentum (k_y), I have plotted transmission probabilities for those k_y values which give a better contrast of the transmission signal for bands *vs.* gaps regions.

operator in the case of an extended lead). All the trivially evolved states are then added to get the final reflected state.

For the numerical calculations, I consider a finite Hilbert space of the scattering region with $L = 80$ and one site of the lead region. The maximum number of time steps of the walk is $n_{\text{max.}} = 400$. The initial state of the walker is the same as given in eq. (5.24). After each step of the walk, the final state is projected to a state localized at position $x = -1$ in the lead with spin-down state, i.e. $|x = -1, \downarrow\rangle$. The projection is

$$a_n(k_y) = \langle x = -1, \downarrow| \, \hat{W}^n(k_y) \, |x = -1, \uparrow\rangle, \tag{5.28}$$

where n represents the time step after which this projection is obtained. The trivial evolution of this projection is carried out without using the walk operator. The corresponding final state is

$$|\Psi^{(n)}_{\text{ref.}}(k_y)\rangle = a_n(k_y) \, |x = -1 - (n_{\text{max.}} - n), \downarrow\rangle. \tag{5.29}$$

We made use of the fact that the velocity of the walker in the lead is one lattice site per step of the walk evolution. The superscript n represent that this final state corresponds to the projection taken at time step n. At the end of the complete time evolution (from $n = 1$ to $n = n_{\text{max.}}$), the total reflected state is obtained performing the sum in equation (5.29) over all values of n, i.e.

$$|\Psi_{\text{ref.}}(k_y)\rangle = \sum_{n=1}^{n_{\text{max.}}} |\Psi^{(n)}_{\text{ref.}}(k_y)\rangle. \tag{5.30}$$

The reflection probabilities are obtained by projecting this state to the plane-wave state (eq. (5.26) with $x_{\text{max.}} = 400$), i.e.

$$R(k_x = \varepsilon, k_y) = \left| \langle \Psi_{\text{lead}}(k_x)|\Psi_{\text{ref.}}(k_y)\rangle \right|^2. \tag{5.31}$$

5.3.2 Reconstructing the Hofstadter Spectrum from the Reflection Probabilities

I repeated the above procedure for $\phi = p/q = 0$ to 0.5 in the step size of 0.02 and computed the reflection (transmission) probabilities. We define a threshold for reflection (transmission) probabilities. For each value of p/q, a quasienergy value belongs to the Hofstadter spectrum's bands if its corresponding reflection probability is smaller than 0.8 (the threshold value). In other words, a quasienergy value belongs to the Hofstadter spectrum's bands if its corresponding transmission probability is greater than 0.2. I plot all those quasienergy values, which are in the bands regions for all values of p/q, i.e. 0 to 0.5. The bands for $0.5 < p/q \leq 1.0$ are obtained by using the fact that the spectrum and hence the reflection probabilities are same for p/q and $1 - p/q$. The reconstructed Hofstadter spectrum is shown in fig. 5.5.

Conclusion and Outlook

The numerical results show that the scattering matrix approach in magnetic QWs of neutral atoms in optical lattices can indeed be used to probe the Hofstadter spectrum. The underlying system provides a clean and controllable environment, along with the possibility of engineering strong artificial magnetic fields. Also, as demonstrated, this approach provides an efficient tool to compute topological invariants. This does neither require translational symmetry in the system nor complete information of the bulk spectrum. In this framework, topological invariants are related to transport properties, which can be measured by locally probing the insulator material. For example, in QWs experiments, the Floquet topological invariants of the bulk gaps can be probed by preparing a particle in a well-defined quasimomentum (energy) state. A particle having quasienergy tuned to a gap of the scattering region (which in this case
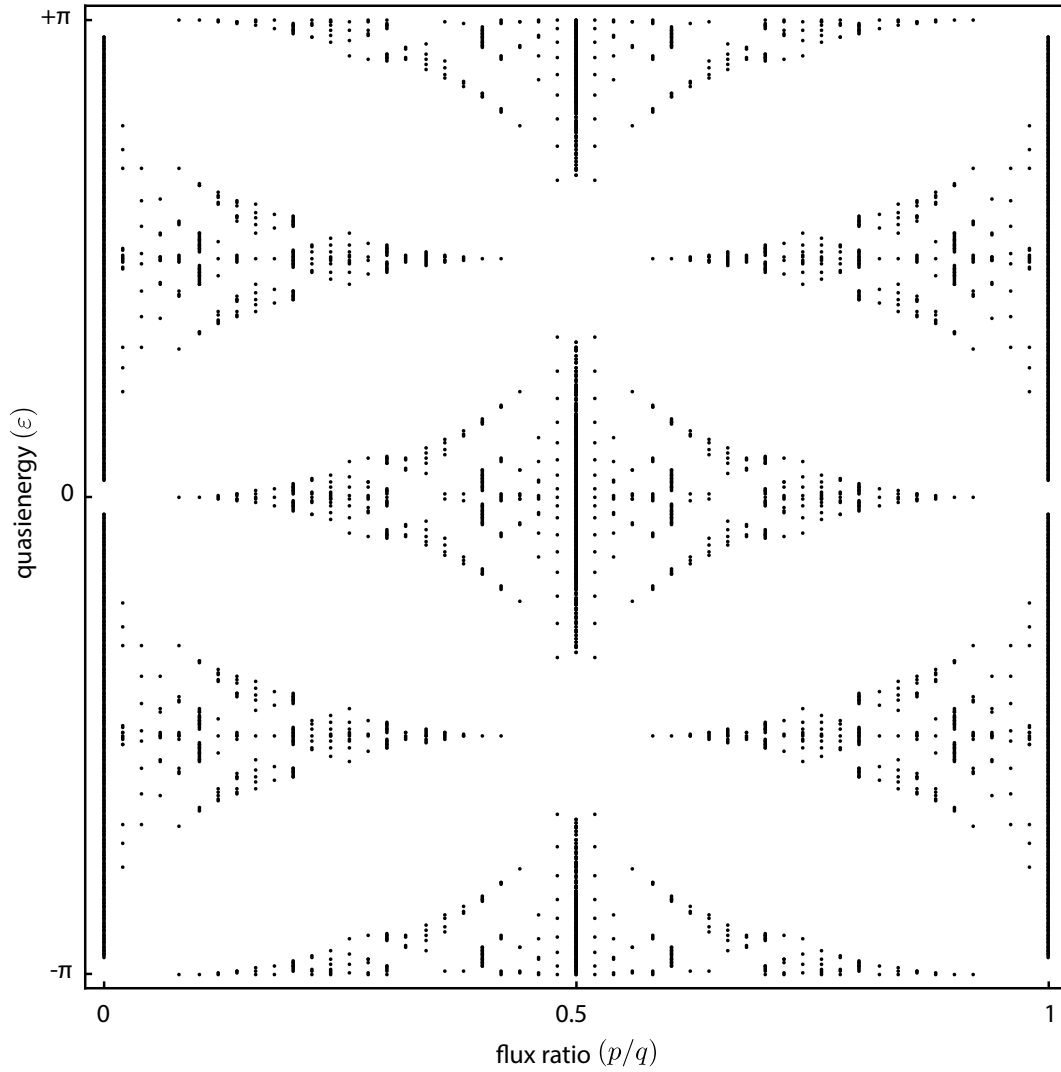
Figure 5.5: Hofstadter spectrum reconstructed from the reflection (transmission) probabilities of a walker form the scattering region. The values of the flux ratio $\phi = p/q$ ranges from 0 to 1 in the step size 0.02. For each value of p/q, black dots represent the quasienergy values for which the computed reflection probability is less the 0.8 or the transmission probability is greater than 0.2 and hence are selected as bands of the Hofstadter spectrum. The spectrum for p/q = 0 to 0.5 is computed from the reflection probabilities and for $0.5 < p/q \leq 1.0$ it is obtained by using the reflection symmetry present in the spectrum.

will be a topological insulator) will be reflected back. The interferometric measurements of the reflection amplitudes will determine the corresponding topological invariant. As the scattering matrix approach does not require translational invariance, it can additionally be used to investigate topological properties in the presence of disorder, thus demonstrating the versatility of this approach in a wide range of settings.

Summary and Outlook

I n this thesis I employed QW protocols as a tool to simulate and study the physics of a charged particle in the presence of both a 2D periodic potential and an external magnetic field. The underlying system is composed of a single neutral atom trapped in a 2D squared optical lattice. To simulate the effects of a magnetic field on neutral atoms, I proposed a realistic scheme based on QWs of a single neutral atom. This scheme has a number of unique features that allows the exploration of the physics in the strong-field regime.

I started with the time-independent tight binding model in 2D in the presence of a strong external magnetic field (Harper's equation) and investigated its topological properties (Chapter 2). I demonstrated that the topological invariants (Chern numbers) of the magnetic Bloch bands fully determine the number of edge states, which exist in the presence of a boundary. To simulate this type of physics with QWs of neutral atoms, I introduced QWs in 1D and 2D (Chapter 3). I investigated the topological properties of the effective Hamiltonians and showed that the corresponding invariants do not fully determine the edge spectrum of the QWs. This fact is highlighted with examples both in 1D and 2D, and the new set of topological invariants, that capture the complete topological structure of the walks, are introduced.

In Chapter 4, I extended the 2D QW protocol to simulate the effects of magnetic fields. In the presence of a magnetic field, the magnetic subbands are characterized by non-vanishing Chern numbers, indicating the Floquet Chern insulating nature of the system. I computed the invariants of the quasienergy gaps that uniquely determine the edge spectrum. I demonstrated the existence of TP propagating edge states and their robustness against spatial and experimental deformations. In Chapter 5, I introduced the scattering matrix formalism in QWs for computing the topological invariants of the 2D QW and for probing the Hofstadter spectrum. By computing the reflection matrix, the topological invariant of a gap is identified as the winding number of its determinant. The reflection and transmission probabilities of the walker from the scattering region give access to the quasienergy spectrum.

Although the work in this thesis is focused on the physics of a single particle which provides a platform for the understanding and classification of topological matter, it also sets the stage for studies of many-body topological states in the presence of interactions. In the following I give a brief outlook on the directions in which this work can be extended.

Modifying the Setting of the Scattering Matrix Problem in the Perspective of our 2D QW Experiment: The results of the scattering matrix approach (topological invariants of the walk and the Hofstadter spectrum) are computed with only one shift operator, i.e. along the x-axis ($\hat{S}_x$), active in the lead region (Chapter 5). However, in our experimental setup, the spin-dependent shift operators act globally and cannot be deactivated locally. In order to configure the scattering matrix approach in the

perspective of our 2D QW experiment, the immediate next step will be to carry out these computations with both shift operators, i.e. $\hat{S}_x$ and $\hat{S}_y$, active in the lead region of the scattering setting as shown in the schematic fig. 6.1.

Interaction Induced Topological Phases: Interactions amongst particles in a topological insulator can lead to novel and less explored topological states of matter, e.g. fractional quantum Hall states for partially filled Chern bands. An interest in these states developed due to their potential application in spintronics devices and topological quantum computation, as quantum information stored in topological degrees of freedom is less susceptible to local perturbations [127, 128]. Accessing interaction-induced effects with conventional condensed matter systems is a challenging task as these cannot be easily isolated from the system [129]. QWs of neutral atoms trapped in optical lattices, on the other hand, due to their high degree of controllability of particle-particle interactions, can be exploited to investigate interaction-induced effects by including onsite coherent cold collisions between atoms [103]. In a bottom-up approach to investigate many-body interacting states, it has been theoretically shown that interaction in QWs of two atoms in 1D lattice leads to the formation of stable molecular states [71]. To investigate two-body interaction effects in QWs, a walk protocol of the following form can be used,

$$\hat{W}_{\text{int.}} = \mathcal{U}_W(p,k) \cdot \mathcal{U}_c = (\hat{W}_1 \otimes \hat{W}_2) \cdot \begin{cases} \mathbb{1} & \text{when } x_1 \neq x_2 \\ \gamma & \text{when } x_1 = x_2 \end{cases},$$

with $\mathcal{U}_W(p,k)$ the free walk operator and $\mathcal{U}_c$ (representing the interaction part of the walk operator) a unitary operator acting only on the collisional subspace. The molecular bound state can be obtained by solving the Lippmann-Schwinger equation for a discrete time system.

The single-particle picture of a 2D magnetic QW presented in this thesis, shows that the system behaves as a Floquet Chern insulator with relatively flat bands separated by large gaps. This provides a favorable condition for strongly correlated states as interactions among particles in these circumstances are the dominating physical mechanism. As topological phases in interacting QWs are not explored yet, it will be interesting to study the effects of interactions on the topological features of Floquet topologically insulating states. More important will be to investigate whether novel topological states can emerge by adding interactions to topologically trivial insulating states underlying QWs. To investigate interaction-induced topological effects with QWs, in experiments based on neutral atoms in optical lattices, atoms have to be cooled down to their motional ground states. On the theory side, the Floquet-Keldysh approach and the time-evolving block decimation numerical methods can be used to investigate Floquet topological phases of interacting QWs.

Disorder Effects: The presence of topological order in a system (QWs) not only has profound implications in the non-trivial phenomena at the edges but it also has strong influence on the transport in the bulk in the presence of static spatial disorder. The common intuition is that spatial disorder always leads to localization phenomena, the well known Anderson localization [130]. For QWs in 1D with a spatially disordered coin operation, such strong localization has been predicted [68], and dynamical localization under irrational artificial electric field has been experimentally demonstrated [102]. The presence of non-trivial topology, however, can lead to a counterintuitive behavior, the so called localization-delocalization transition in both 1D and 2D QWs. Numerically, it has been shown that a walker can escape localization if the walk is tuned to a phase boundary between two distinct topological phases [69, 70].

For the magnetic QW presented in this thesis, it will be worth to explore the effects of disorder
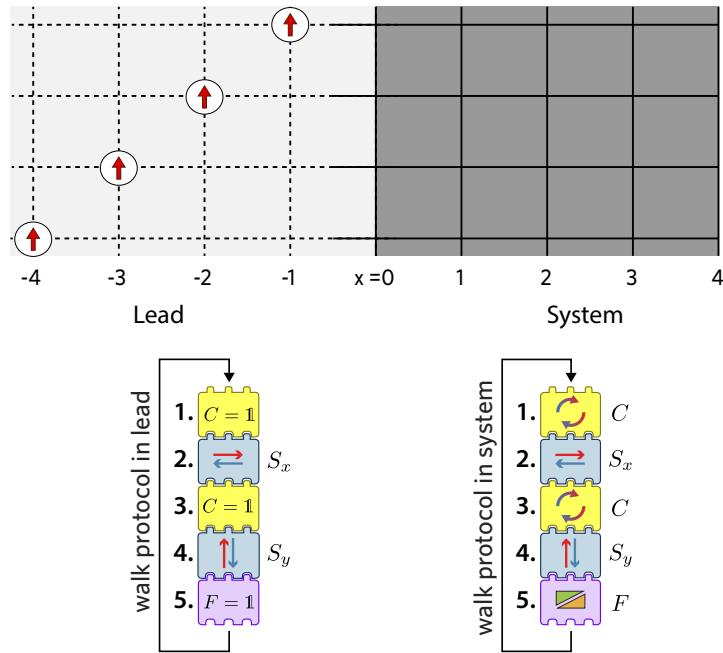
Figure 6.1: Schematic of the scattering setting for probing the topological invariants of the gaps for a 2D magnetic QW, and the Hofstadter spectrum. To take into account the fact that the spin-dependent shift operators act globally in our 2D setup, the numerical computation needs to be carried out with both shift operators, i.e. $\hat{S}_x$ and $\hat{S}_y$, active in the lead region.

on the critical transport phenomena, e.g. similar to the localization-delocalization transition between two adjacent Hall plateaux in integer QHE underlying a lattice. It will be important to investigate the robustness of edge transport against different types of disorder and the conditions leading to a topological phase transition, similar to those investigated for 2D QWs without magnetic fields [70, 93]. In the presence of disorder, the scattering matrix formalism can be employed to investigate the topological invariants of the walk. In QWs, a spatial static disorder can be introduced by adding an extra operator to the walk protocol that implements a position-dependent random phase shift to the walker (the phase shift can be spin-dependent as well). Similarly, disorder can also be introduced through a coin operator by varying the coin angle from site to site randomly.

Non-Abelian Gauge Potentials: The proposed scheme for implementing a synthetic gauge potential is for the abelian case, where the simulated magnetic field results in a phase shift of the walker. An extension to non-abelian gauge potentials will be interesting to investigate with QWs. In the case of non-abelian gauge potentials, the phase shift due to a magnetic field is replaced by a matrix with dimensions depending on the internal Hilbert space of the particle. There has been a number of proposals for generating synthetic non-abelian gauge fields for neutral atoms [30, 31]. These are used for simulating spin-orbit coupling of electrons in condensed matter systems, which is at the heart of a number of interesting phenomena, such as topological insulators.

Bibliography

[1]   M. Sajid, J. K. Asbóth, P. Arnault, D. Meschede, R. Werner and A. Alberti, "Realizing Floquet Chern insulators with discrete-time quantum walks", In preparation (2018) (cit. on p. v).

[2]   K. v. Klitzing, G. Dorda and M. Pepper, "New Method for High-Accuracy Determination of the Fine-Structure Constant Based on Quantized Hall Resistance", Phys. Rev. Lett. 45.6 (1980) 494, ISSN: 0031-9007 (cit. on pp. 1, 5).

[3]   K. von Klitzing, "The quantized Hall effect", Rev. Mod. Phys. 58.3 (1986) 519 (cit. on pp. 1, 5).

[4]   M. O. Goerbig, "Quantum Hall Effects", (2009), arXiv: 0909.1998 (cit. on pp. 1, 7, 8, 44).

[5]   D. J. Thouless, M. Kohmoto, M. P. Nightingale and M. den Nijs, "Quantized Hall Conductance in a Two-Dimensional Periodic Potential", Phys. Rev. Lett. 49.6 (1982) 405, ISSN: 0031-9007 (cit. on pp. 1, 15, 16).

[6]   M. Z. Hasan and C. L. Kane, "Colloquium: Topological insulators", Rev. Mod. Phys. 82.4 (2010) 3045, ISSN: 00346861, arXiv: 1002.3895 (cit. on p. 1).

[7]   C. Kane, "Topological Band Theory and the Z2 Invariant", *Contemp. Concepts Condens. Matter Sci.* Vol. 6, Elsevier, 2013 3, ISBN: 9780444633149, arXiv: 1002.3895 (cit. on pp. 1, 15).

[8]   Y. Hatsugai, "Chern number and edge states in the integer quantum Hall effect", Phys. Rev. Lett. 71.22 (1993) 3697 (cit. on pp. 1, 6, 18).

[9]   B. Simon, "Holonomy, the Quantum Adiabatic Theorem, and Berry's Phase", Phys. Rev. Lett. 51.24 (1983) 2167, ISSN: 0031-9007 (cit. on p. 1).

[10]   F. D. M. Haldane, "Model for a Quantum Hall Effect without Landau Levels: Condensed-Matter Realization of the "Parity Anomaly"", Phys. Rev. Lett. 61.18 (1988) 2015, ISSN: 0031-9007 (cit. on p. 1).

[11]   C.-Z. Chang, J. Zhang, X. Feng, J. Shen, Z. Zhang, M. Guo, K. Li, Y. Ou, P. Wei, L.-L. Wang, Z.-Q. Ji, Y. Feng, S. Ji, X. Chen, J. Jia, X. Dai, Z. Fang, S.-C. Zhang, K. He, Y. Wang, L. Lu, X.-C. Ma and Q.-K. Xue, "Experimental Observation of the Quantum Anomalous Hall Effect in a Magnetic Topological Insulator", Science 340.6129 (2013) 167, ISSN: 0036-8075 (cit. on pp. 1, 41).

[12]   G. Jotzu, M. Messer, R. Desbuquois, M. Lebrat, T. Uehlinger, D. Greif and T. Esslinger, "Experimental realization of the topological Haldane model with ultracold fermions", Nature 515.7526 (2014) 237, ISSN: 14764687, arXiv: 1406.7874 (cit. on pp. 1, 2, 5, 41).

[13]   M. Aidelsburger, M. Lohse, C. Schweizer, M. Atala, J. T. Barreiro, S. Nascimbène, N. R. Cooper, I. Bloch and N. Goldman, "Measuring the Chern number of Hofstadter bands with ultracold bosonic atoms", Nat. Phys. 11.2 (2015) 162, ISSN: 17452481, arXiv: 1407.4205 (cit. on pp. 1, 2, 5, 41).

[14] N. Fläschner, D. Vogel, M. Tarnowski, B. S. Rem, D. S. Lühmann, M. Heyl, J. C. Budich,
L. Mathey, K. Sengstock and C. Weitenberg,
"Observation of dynamical vortices after quenches in a system with topology",
Nat. Phys. 14.3 (2018) 265, ISSN: 17452481, arXiv: 1608.05616 (cit. on p. 1).

[15] E. J. Bergholtz and Z. Liu, "Topological Flat Band Models and Fractional Chern Insulators",
Int. J. Mod. Phys. B 27.24 (2013) 1330017, ISSN: 0217-9792, arXiv: 1308.0343
(cit. on pp. 1, 41).

[16] S. A. Parameswaran, R. Roy and S. L. Sondhi,
"Fractional quantum Hall physics in topological flat bands",
Comptes Rendus Phys. 14.9-10 (2013) 816, ISSN: 16310705, arXiv: 1302.6606
(cit. on pp. 1, 41).

[17] T. Neupert, C. Chamon, T. Iadecola, L. H. Santos and C. Mudry,
"Fractional (Chern and topological) insulators", Phys. Scr. T164.T164 (2015) 014005,
ISSN: 0031-8949, arXiv: 1410.5828 (cit. on pp. 1, 41).

[18] E. Tang, J.-W. Mei and X.-G. Wen, "High Temperature Fractional Quantum Hall States",
Phys. Rev. Lett. 106.23 (2011) 236802, ISSN: 0031-9007, arXiv: 1012.2930 (cit. on pp. 2, 41).

[19] K. Sun, Z. Gu, H. Katsura and S. Das Sarma, "Nearly Flatbands with Nontrivial Topology",
Phys. Rev. Lett. 106.23 (2011) 236803, ISSN: 00319007, arXiv: 1012.5864 (cit. on pp. 2, 3, 41).

[20] T. Neupert, L. Santos, C. Chamon and C. Mudry,
"Fractional Quantum Hall States at Zero Magnetic Field",
Phys. Rev. Lett. 106.23 (2011) 236804, ISSN: 00319007, arXiv: 1012.4723 (cit. on pp. 2, 3, 41).

[21] D. N. Sheng, Z.-C. Gu, K. Sun and L. Sheng,
"Fractional quantum Hall effect in the absence of Landau levels.", Nat. Commun. 2 (2011) 389,
ISSN: 2041-1723, arXiv: arXiv:1102.2658v1 (cit. on pp. 2, 3, 41).

[22] Y. H. Wu, J. K. Jain and K. Sun,
"Adiabatic continuity between Hofstadter and Chern insulator states",
Phys. Rev. B 86.16 (2012) 165129, ISSN: 10980121, arXiv: 1207.4439 (cit. on p. 2).

[23] T. Scaffidi and G. Möller,
"Adiabatic Continuation of Fractional Chern Insulators to Fractional Quantum Hall States",
Phys. Rev. Lett. 109.24 (2012) 246805, ISSN: 00319007, arXiv: arXiv:1207.3539v1
(cit. on p. 2).

[24] D. R. Hofstadter,
"Energy levels and wave functions of Bloch electrons in rational and irrational magnetic fields",
Phys. Rev. B 14.6 (1976) 2239 (cit. on pp. 2, 5, 13, 14, 44, 57).

[25] M. Hafezi, A. S. Sørensen, E. Demler and M. D. Lukin,
"Fractional quantum Hall effect in optical lattices", Phys. Rev. A 76.2 (2007) 023613,
ISSN: 1050-2947, arXiv: 0706.0757 (cit. on p. 2).

[26] N. R. Cooper and J. Dalibard,
"Reaching Fractional Quantum Hall States with Optical Flux Lattices",
Phys. Rev. Lett. 110.18 (2013) 1, ISSN: 00319007, arXiv: arXiv:1212.3552v1 (cit. on p. 2).

[27] N. Y. Yao, A. V. Gorshkov, C. R. Laumann, A. M. Läuchli, J. Ye and M. D. Lukin,
"Realizing Fractional Chern Insulators in Dipolar Spin Systems",
Phys. Rev. Lett. 110.18 (2013) 185302, ISSN: 00319007, arXiv: 1212.4839 (cit. on p. 2).

[28]   C. Albrecht, J. H. Smet, K. von Klitzing, D. Weiss, V. Umansky and H. Schweizer,
       "Evidence of Hofstadter's Fractal Energy Spectrum in the Quantized Hall Conductance",
       Phys. Rev. Lett. 86.1 (2001) 147 (cit. on pp. 2, 5, 57).

[29]   C. R. Dean, L. Wang, P. Maher, C. Forsythe, F. Ghahari, Y. Gao, J. Katoch, M. Ishigami,
       P. Moon, M. Koshino, T. Taniguchi, K. Watanabe, K. L. Shepard, J. Hone and P. Kim,
       "Hofstadter's butterfly and the fractal quantum Hall effect in moiré superlattices",
       Nature 497.7451 (2013) 598 (cit. on pp. 2, 5, 57).

[30]   J. Dalibard, F. Gerbier, G. Juzeliunas and P. Öhberg,
       "Colloquium: Artificial gauge potentials for neutral atoms", Rev. Mod. Phys. 83.4 (2011) 1523
       (cit. on pp. 2, 8, 73).

[31]   N. Goldman, G. Juzeliūnas, P. Öhberg and I. B. Spielman,
       "Light-induced gauge fields for ultracold atoms", Reports Prog. Phys. 77.12 (2014) 126401,
       ISSN: 0034-4885 (cit. on pp. 2, 73).

[32]   M. Aidelsburger, S. Nascimbene and N. Goldman,
       "Artificial gauge fields in materials and engineered systems", (2017), arXiv: `1710.00851`
       (cit. on p. 2).

[33]   D. Jaksch and P. Zoller, "Creation of effective magnetic fields in optical lattices: the Hofstadter
       butterfly for cold neutral atoms", New J. Phys. 5 (2003) 56, ISSN: 1367-2630 (cit. on pp. 2, 53).

[34]   E. J. Mueller,
       "Artificial electromagnetism for neutral atoms: Escher staircase and Laughlin liquids",
       Phys. Rev. A 70.4 (2004) 041603, ISSN: 1050-2947 (cit. on p. 2).

[35]   F. Gerbier and J. Dalibard, "Gauge fields for ultracold atoms in optical superlattices",
       New J. Phys. 12.3 (2010) 033007, ISSN: 1367-2630, arXiv: `0910.4606` (cit. on pp. 2, 53).

[36]   A. R. Kolovsky, "Creating artificial magnetic fields for cold atoms by photon-assisted tunneling",
       EPL (Europhysics Lett. 93.2 (2011) 20003, ISSN: 0295-5075, arXiv: `1006.5270` (cit. on p. 2).

[37]   M. G. Tarallo, A. Alberti, N. Poli, M. L. Chiofalo, F. Y. Wang and G. M. Tino,
       "Delocalization-enhanced Bloch oscillations and driven resonant tunneling in optical lattices for
       precision force measurements", Phys. Rev. A 86.3 (2012) 033615, ISSN: 10502947,
       arXiv: `1207.2123` (cit. on p. 2).

[38]   C. E. Creffield, G. Pieplow, F. Sols and N. Goldman, "Realization of uniform synthetic magnetic
       fields by periodically shaking an optical square lattice", New J. Phys. 18.9 (2016) 093013,
       ISSN: 1367-2630, arXiv: `1605.09604` (cit. on p. 2).

[39]   M. Aidelsburger, M. Atala, M. Lohse, J. T. Barreiro, B. Paredes and I. Bloch,
       "Realization of the Hofstadter Hamiltonian with Ultracold Atoms in Optical Lattices",
       Phys. Rev. Lett. 111.18 (2013) (cit. on pp. 2, 5, 41, 57).

[40]   H. Miyake, G. A. Siviloglou, C. J. Kennedy, W. C. Burton and W. Ketterle,
       "Realizing the Harper Hamiltonian with Laser-Assisted Tunneling in Optical Lattices",
       Phys. Rev. Lett. 111.18 (2013), ISSN: 00319007, arXiv: `1308.1431` (cit. on pp. 2, 5, 57).

[41]   S. Lellouch, M. Bukov, E. Demler and N. Goldman,
       Parametric instability rates in periodically driven band systems, 2017, arXiv: `1610.02972`
       (cit. on p. 2).

[42] M. Reitter, J. Näger, K. Wintersperger, C. Sträter, I. Bloch, A. Eckardt and U. Schneider,
      "Interaction Dependent Heating and Atom Loss in a Periodically Driven Optical Lattice",
      Phys. Rev. Lett. 119.20 (2017) 200402, ISSN: 0031-9007, arXiv: 1706.04819 (cit. on pp. 2, 41).

[43] W. Yi, A. J. Daley, G. Pupillo and P. Zoller,
      "State-dependent, addressable subwavelength lattices with cold atoms",
      New J. Phys. 10.7 (2008) 073015, ISSN: 13672630, arXiv: 0801.0600 (cit. on p. 2).

[44] S. Nascimbene, N. Goldman, N. R. Cooper and J. Dalibard,
      "Dynamic Optical Lattices of Subwavelength Spacing for Ultracold Atoms",
      Phys. Rev. Lett. 115.14 (2015) 140401, ISSN: 10797114, arXiv: 1506.00558 (cit. on p. 2).

[45] P. G. Harper, "Single Band Motion of Conduction Electrons in a Uniform Magnetic Field",
      Proc. Phys. Soc. Sect. A 68.10 (1955) 874, ISSN: 0370-1298 (cit. on pp. 2, 13).

[46] J. Dalibard, "Introduction to the physics of artificial gauge fields", (2015), arXiv: 1504.05520
      (cit. on pp. 5, 7, 8).

[47] D. B. A. Aharonov, "On the significance of electromagnetic potentials in the quantum theory",
      Phys. Rev. 115.3 (1959) 485 (cit. on pp. 5, 7).

[48] T. Haugset, J. A. Ruud and F. Ravndal, "Gauge invariance of Landau levels",
      Phys. Scr. 47.6 (1993) 715, ISSN: 14024896 (cit. on p. 7).

[49] J. M. Luttinger, "The effect of a magnetic field on electrons in a periodic potential",
      Phys. Rev. 84.4 (1951) 814, ISSN: 0031899X (cit. on p. 8).

[50] R. Peierls, "Zur Theorie des Diamagnetismus von Leitungselektronen",
      Z. Phys. 80.11-12 (1933) 763, ISSN: 14346001 (cit. on p. 8).

[51] E. Brown, "Bloch Electrons in a Uniform Magnetic Field", Phys. Rev. 133.4A (1964) A1038,
      ISSN: 0031-899X (cit. on p. 9).

[52] J. Zak, "Magnetic translation group", Phys. Rev. 134.6A (1964), ISSN: 0031899X (cit. on p. 9).

[53] J. Zak, "Magnetic Translation Group. II. Irreducible Representations",
      Phys. Rev. 134.6A (1964) A1607, ISSN: 0031-899X (cit. on p. 9).

[54] T. L. H. B. A. Bernevig, *Topological insulators and topological superconductors*,
      Princeton University Press, 2013, ISBN: 9780691151755 (cit. on pp. 10, 85).

[55] M. Aidelsburger, *Artificial Gauge Fields with Ultracold Atoms in Optical Lattices*,
      Springer Theses, Springer International Publishing, 2016, ISBN: 978-3-319-25827-0
      (cit. on pp. 10, 12, 85, 93).

[56] X. G. Wen and A. Zee,
      "Winding number, family index theorem, and electron hopping in a magnetic field",
      Nucl. Physics, Sect. B 316.3 (1989) 641, ISSN: 05503213 (cit. on pp. 14, 93).

[57] M. NAKAHARA, *Geometry, Topology, and Physics*,
      Institute of Physics Publishing, Bristol and Philadelphia, 2003 573, ISBN: 0750306068
      (cit. on p. 15).

[58] P. Streda, "Quantised Hall effect in a two-dimensional periodic potential",
      J. Phys. C Solid State Phys. 15.36 (1982) L1299, ISSN: 0022-3719 (cit. on p. 16).

[59] T. Fukui, Y. Hatsugai and H. Suzuki, "Chern Numbers in Discretized Brillouin Zone: Efficient
      Method of Computing Spin Hall Conductances", J. Phys. Soc. Jpn. 74 (2005) 1674
      (cit. on pp. 18, 44, 89, 91).

[60] B. I. Halperin, "Quantized Hall conductance, current-carrying edge states, and the existence of extended states in a two-dimensional disordered potential", Phys. Rev. B 25.4 (1982) 2185, ISSN: 0163-1829 (cit. on p. 18).

[61] Y. Hatsugai, "Edge states in the integer quantum Hall effect and the Riemann surface of the Bloch function", Phys. Rev. B 48.16 (1993) 11851 (cit. on p. 18).

[62] Y. Hatsugai, "Topological aspects of the quantum Hall effect", J. Phys. Condens. Matter 9.12 (1997) 2507, ISSN: 09538984 (cit. on p. 18).

[63] Y. Aharonov, L. Davidovich and N. Zagury, "Quantum random walks", Phys. Rev. A 48.2 (1993) 1687 (cit. on p. 21).

[64] J. Kempe, "Quantum random walks: An introductory overview", Contemp. Phys. 44.4 (2003) 307, ISSN: 0010-7514 (cit. on pp. 21, 24).

[65] I. M. Georgescu, S. Ashhab and F. Nori, "Quantum simulation", Rev. Mod. Phys. 86.1 (2014) 153, ISSN: 15390756, arXiv: 1308.6253 (cit. on p. 21).

[66] A. M. Childs, "Universal Computation by Quantum Walk", Phys. Rev. Lett. 102.18 (2009) 1, ISSN: 00319007, arXiv: 0806.1972 (cit. on p. 21).

[67] N. B. Lovett, S. Cooper, M. Everitt, M. Trevers and V. Kendon, "Universal quantum computation using the discrete-time quantum walk", Phys. Rev. A 81.4 (2010) 042330, ISSN: 1050-2947, arXiv: 0910.1024 (cit. on p. 21).

[68] A. Ahlbrecht, V. B. Scholz and A. H. Werner, "Disordered quantum walks in one lattice dimension", J. Math. Phys. 52.10 (2011) 102201, ISSN: 0022-2488, arXiv: 1101.2298 (cit. on pp. 21, 72).

[69] T. Rakovszky and J. K. Asboth, "Localization, delocalization, and topological phase transitions in the one-dimensional split-step quantum walk", Phys. Rev. A 92.5 (2015) 052311, ISSN: 1050-2947, arXiv: 1505.04513 (cit. on pp. 21, 60, 72).

[70] J. M. Edge and J. K. Asboth, "Localization, delocalization, and topological transitions in disordered two-dimensional quantum walks", Phys. Rev. B 91.10 (2015) 104202, ISSN: 1098-0121, arXiv: 1411.7691 (cit. on pp. 21, 72, 73).

[71] A. Ahlbrecht, A. Alberti, D. Meschede, V. B. Scholz, A. H. Werner and R. F. Werner, "Molecular binding in interacting quantum walks", New J. Phys. 14.7 (2012) 073050, ISSN: 1367-2630, arXiv: 1105.1051 (cit. on pp. 21, 56, 72).

[72] T. Kitagawa, M. S. Rudner, E. Berg and E. Demler, "Exploring topological phases with quantum walks", Phys. Rev. A 82.3 (2010) 033429, ISSN: 10502947, arXiv: 1003.1729 (cit. on pp. 21, 30).

[73] J. K. Asbóth, "Symmetries, topological phases, and bound states in the one-dimensional quantum walk", Phys. Rev. B 86.19 (2012) 195414, ISSN: 1098-0121, arXiv: 1208.2143 (cit. on pp. 21, 47).

[74] J. K. Asbóth and H. Obuse, "Bulk-boundary correspondence for chiral symmetric quantum walks", Phys. Rev. B 88.12 (2013) 1, ISSN: 10980121, arXiv: 1303.1199 (cit. on pp. 21, 30, 32).

[75] M. S. Rudner, N. H. Lindner, E. Berg and M. Levin, "Anomalous Edge States and the Bulk-Edge Correspondence for Periodically Driven Two-Dimensional Systems", Phys. Rev. X 3.3 (2013) 031005, ISSN: 2160-3308 (cit. on pp. 21, 27, 38, 44, 45, 61).

[76] J. K. Asbóth, B. Tarasinski and P. Delplace, "Chiral symmetry and bulk-boundary correspondence in periodically driven one-dimensional systems", Phys. Rev. B 90.12 (2014) 1, ISSN: 1550235X, arXiv: 1405.1709 (cit. on p. 21).

[77] C. M. Chandrashekar, "Discrete-Time Quantum Walk - Dynamics and Applications", PhD thesis, 2010 199, arXiv: 1001.5326 (cit. on p. 22).

[78] P. Arnault, "Discrete-time quantum walks and gauge theories", PhD thesis, 2017, arXiv: 1710.11123 (cit. on p. 22).

[79] A. Nayak and A. Vishwanath, "Quantum Walk on the Line", tech. rep., 2000, arXiv: quant-ph/0010117 [quant-ph] (cit. on p. 22).

[80] A. Ambainis, E. Bach, A. Nayak, A. Vishwanath and J. Watrous, "One-dimensional quantum walks", Proc. thirty-third Annu. ACM Symp. Theory Comput. - STOC '01 (2001) 37 (cit. on pp. 23, 24, 42).

[81] C. D. Franco, M. M. Gettrick and T. Busch, "Mimicking the Probability Distribution of a Two-Dimensional Grover Walk with a Single-Qubit Coin", Phys. Rev. Lett. 106 (2011) 80502 (cit. on pp. 23, 42).

[82] N. Shenvi, J. Kempe and K. B. Whaley, "Quantum random-walk search algorithm", Phys. Rev. A 67.5 (2003) 52307 (cit. on p. 25).

[83] A. Alberti, W. Alt, R. Werner and D. Meschede, "Decoherence models for discrete-time quantum walks and their application to neutral atom experiments", New J. Phys. 16.12 (2014) 123052, ISSN: 13672630, arXiv: 1409.6145 (cit. on p. 26).

[84] T. Kitagawa, "Topological phenomena in quantum walks: Elementary introduction to the physics of topological phases", Quantum Inf. Process. 11.5 (2012) 1107, ISSN: 15700755, arXiv: 1112.1882 (cit. on pp. 26, 27, 36, 38, 44, 47, 49).

[85] M. Grifoni and P. Hänggi, "Driven quantum tunneling", Phys. Rep. 304.5-6 (1998) 229, ISSN: 03701573 (cit. on p. 27).

[86] S. Ryu, A. P. Schnyder, A. Furusaki and A. W. W. Ludwig, "Topological insulators and superconductors: tenfold way and dimensional hierarchy", New. J. Phys. 12 (2010), ISSN: 13672630, arXiv: 0912.2157 (cit. on pp. 28, 38, 60).

[87] A. Altland and M. R. Zirnbauer, "Nonstandard symmetry classes in mesoscopic normal-superconducting hybrid structures", Phys. Rev. B 55.2 (1997) 1142, ISSN: 0163-1829 (cit. on pp. 28, 60).

[88] H. Obuse, J. K. Asbóth, Y. Nishimura and N. Kawakami, "Unveiling hidden topological phases of a one-dimensional Hadamard quantum walk", Phys. Rev. B 92.4 (2015) 1, ISSN: 1550235X, arXiv: 1505.03264 (cit. on pp. 30, 35).

[89] C. Cedzich, F. A. Grünbaum, C. Stahl, L. Velázquez, A. H. Werner and R. F. Werner, "Bulk-edge correspondence of one-dimensional quantum walks", J. Phys. A Math. Theor. 49.21 (2016), ISSN: 17518121, arXiv: 1502.02592 (cit. on p. 30).

[90] S. Mugel, A. Celi, P. Massignan, J. K. Asbóth, M. Lewenstein and C. Lobo, "Topological bound states of a quantum walk with cold atoms", Phys. Rev. A 023631.2 (2016) 1, ISSN: 2469-9926, arXiv: 1604.06082 (cit. on p. 30).

[91] T. Groh, S. Brakhane, W. Alt, D. Meschede, J. K. Asbóth and A. Alberti, "Robustness of topologically protected edge states in quantum walk experiments with neutral atoms", Phys. Rev. A 94.1 (2016) 13620 (cit. on pp. 30, 32, 33, 35, 40, 47, 48, 51, 54).

[92] Stefan Brakhane, "The Quantum Walk Microscope", PhD Thesis (2016) (cit. on pp. 36, 51).

[93] J. K. Asboth and J. M. Edge, "Edge-state-enhanced transport in a two-dimensional quantum walk", Phys. Rev. A 91.2 (2015) 022324, ISSN: 1050-2947 (cit. on pp. 38, 39, 44, 61, 73).

[94] J. K. Asbóth and A. Alberti, "Spectral Flow and Global Topology of the Hofstadter Butterfly", Phys. Rev. Lett. 118.21 (2017) 1, ISSN: 10797114, arXiv: 1611.07052 (cit. on p. 45).

[95] Y. Liu, R. P. Tiwari, M. Brada, C. Bruder, F. V. Kusmartsev and E. J. Mele, "Snake states and their symmetries in graphene", Phys. Rev. B 92.23 (2015) 1, ISSN: 1550235X, arXiv: 1510.08361 (cit. on p. 47).

[96] P. D. Ye, D. Weiss, R. R. Gerhardts, M. Seeger, K. Von Klitzing, K. Eberl and H. Nickel, "Electrons in a periodic magnetic field induced by a regular array of micromagnets", Phys. Rev. Lett. 74.15 (1995) 3013, ISSN: 00319007 (cit. on p. 47).

[97] P. Rickhaus, P. Makk, M.-H. Liu, E. Tóvári, M. Weiss, R. Maurand, K. Richter and C. Schönenberger, "Snake trajectories in ultraclean graphene p–n junctions", Nat. Commun. 6 (2015) 6470, ISSN: 2041-1723, arXiv: 1502.1935 (cit. on p. 47).

[98] C. Robens, J. Zopes, W. Alt, S. Brakhane, D. Meschede and A. Alberti, "Low-Entropy States of Neutral Atoms in Polarization-Synthesized Optical Lattices", Phys. Rev. Lett. 118.6 (2017) 065302, ISSN: 10797114, arXiv: 1608.02410 (cit. on p. 49).

[99] C. Robens, S. Brakhane, W. Alt, D. Meschede, J. Zopes and A. Alberti, "Fast, High-Precision Optical Polarization Synthesizer for Ultracold-Atom Experiments", Phys. Rev. Appl. 9.3 (2018) 034016, ISSN: 2331-7019, arXiv: 1611.07952 (cit. on p. 49).

[100] N. Belmechri, L. Förster, W. Alt, A. Widera, D. Meschede and A. Alberti, "Microwave control of atomic motional states in a spin-dependent optical lattice", J. Phys. B At. Mol. Opt. Phys. 46.10 (2013) 104006, ISSN: 09534075, arXiv: 1302.6208 (cit. on p. 49).

[101] R. Grimm, M. Weidemüller and Y. B. Ovchinnikov, "Optical Dipole Traps for Neutral Atoms", *Adv. At. Mol. Opt. Phys.* Vol. 42, C, Academic Press, 2000 95, ISBN: 0120038420 (cit. on pp. 52, 53).

[102] M. Genske, W. Alt, A. Steffen, A. H. Werner, R. F. Werner, D. Meschede and A. Alberti, "Electric Quantum Walks with Individual Atoms", Phys. Rev. Lett. 110.19 (2013) 190601, ISSN: 0031-9007, arXiv: 1302.2094 (cit. on pp. 53, 72).

[103] O. Mandel, M. Greiner, A. Widera, T. Rom, T. W. Hänsch and I. Bloch, "Controlled collisions for multi-particle entanglement of optically trapped atoms", Nature 425.6961 (2003) 937, ISSN: 0028-0836 (cit. on pp. 56, 72).

[104] I. I. Satija, *Butterfly in the Quantum World The story of the most fascinating quantum fractal*, IOP Publishing, 2016, ISBN: 978-1-6817-4117-8 (cit. on p. 57).

[105] R. R. Gerhardts, D. Weiss and K. v. Klitzing, "Novel Magnetoresistance Oscillations in a Periodically Modulated Two-Dimensional Electron Gas", Phys. Rev. Lett. 62.10 (1989) 1173, ISSN: 0031-9007 (cit. on p. 57).

[106]   T. Schlösser, K. Ensslin, J. P. Kotthaus and M. Holland, "Landau subbands generated by a lateral electrostatic superlattice - chasing the Hofstadter butterfly",
Semicond. Sci. Technol. 11 (1996) 1582, ISSN: 0268-1242 (cit. on p. 57).

[107]   T. Schlösser, K. Ensslin, J. P. Kotthaus and M. Holland, "Internal structure of a Landau band induced by a lateral superlattice: a glimpse of Hofstadter's butterfly",
Europhys. Lett. 33.9 (1996) 683, ISSN: 0295-5075 (cit. on p. 57).

[108]   K. Ensslin and T. Schlösser, "Quantum transport in lateral superlattices",
Phys. Scr. T66.T66 (1996) 135, ISSN: 0031-8949 (cit. on p. 57).

[109]   L. A. Ponomarenko, R. V. Gorbachev, G. L. Yu, D. C. Elias, R. Jalil, A. A. Patel, A. Mishchenko, A. S. Mayorov, C. R. Woods, J. R. Wallbank, M. Mucha-Kruczynski, B. A. Piot, M. Potemski, I. V. Grigorieva, K. S. Novoselov, F. Guinea, V. I. Fal'ko and A. K. Geim,
"Cloning of Dirac fermions in graphene superlattices", Nature 497.7451 (2013) 594,
ISSN: 0028-0836, arXiv: 1212.5012 (cit. on p. 57).

[110]   U. Kuhl and H. J. Stöckmann, "Microwave Realization of the Hofstadter Butterfly",
Phys. Rev. Lett. 80.1 (1998) 3232, ISSN: 0031-9007 (cit. on p. 57).

[111]   O. Richoux and V. Pagneux,
"Acoustic characterization of Hofstadter butterfly with resonant scatterers",
Europhys. Lett. 59.July (2009) 34, ISSN: 0295-5075, arXiv: arXiv:0907.2517v1 (cit. on p. 57).

[112]   C. W. J. Beenakker, "Random-matrix theory of quantum transport",
Rev. Mod. Phys. 69.3 (1997) 731, ISSN: 0034-6861 (cit. on pp. 57–59).

[113]   R. Landauer,
"Spatial Variation of Currents and Fields Due to Localized Scatterers in Metallic Conduction",
IBM J. Res. Dev. 1.3 (1957) 223, ISSN: 0018-8646 (cit. on pp. 58, 59).

[114]   R. Landauer, "Electrical resistance of disordered one-dimensional lattices",
Philos. Mag. 21.172 (1970) 863, ISSN: 0031-8086 (cit. on p. 58).

[115]   D. S. Fisher and P. A. Lee, "Relation between conductivity and transmission matrix",
Phys. Rev. B 23.12 (1981) 6851, ISSN: 01631829 (cit. on p. 58).

[116]   M. Buttiker, Y. Imry and R. Landauer,
"Josephson behavior in small normal one-dimensional rings", Phys. Lett. A 96.7 (1983) 365,
ISSN: 03759601 (cit. on p. 58).

[117]   M. Buttiker, "Voltage fluctuations in small conductors", Phys. Rev. B 35.8 (1987) 4123,
ISSN: 01631829 (cit. on p. 58).

[118]   R. Landauer, "Electrical transport in open and closed systems",
Zeitschrift für Phys. B Condens. Matter 68.2-3 (1987) 217, ISSN: 07223277 (cit. on p. 58).

[119]   M. Buttiker, "Coherent and sequential tunneling in series barriers",
IBM J. Res. Dev. 32.1 (1988) 63, ISSN: 0018-8646 (cit. on p. 58).

[120]   I. C. Fulga, F. Hassler, A. R. Akhmerov and C. W. J. Beenakker,
"Scattering formula for the topological quantum number of a disordered multimode wire",
Phys. Rev. B 83.15 (2011) 155429, ISSN: 1098-0121, arXiv: 1101.1749 (cit. on p. 58).

[121]   I. C. Fulga, "Scattering theory of topological phase transitions",
PhD thesis: Leiden University, 2013, ISBN: 9789085931676 (cit. on pp. 58, 59).

[122] A. R. Akhmerov, J. P. Dahlhaus, F. Hassler, M. Wimmer and C. W. J. Beenakker, "Quantized Conductance at the Majorana Phase Transition in a Disordered Superconducting Wire", Phys. Rev. Lett. 106.5 (2011) 057001, ISSN: 0031-9007 (cit. on p. 58).

[123] M. Wimmer, A. R. Akhmerov, J. P. Dahlhaus and C. W. Beenakker, "Quantum point contact as a probe of a topological superconductor", New J. Phys. 13 (2011), ISSN: 13672630, arXiv: 1101.5795 (cit. on p. 58).

[124] D. Dresen, "Quantum Transport of Non-Interacting Electrons in 2D Systems of Arbitrary Geometries", PhD thesis: RWTH Aachen University, 2014 (cit. on pp. 59, 60).

[125] I. C. Fulga, F. Hassler and A. R. Akhmerov, "Scattering theory of topological insulators and superconductors", Phys. Rev. B 85 (2012) 165409 (cit. on p. 60).

[126] B. Tarasinski, J. K. Asbóth and J. P. Dahlhaus, "Scattering theory of topological phases in discrete-time quantum walks", Phys. Rev. A 89.4 (2014) 042327, arXiv: 1401.2673 (cit. on pp. 60, 61, 64).

[127] A. Kitaev, "Fault-tolerant quantum computation by anyons", Ann. Phys. (N. Y). 303.1 (2003) 2, ISSN: 00034916 (cit. on p. 72).

[128] S. D. Sarma, M. Freedman and C. Nayak, "Topological quantum computation", Phys. Today 59.7 (2006) 32, ISSN: 0031-9228 (cit. on p. 72).

[129] K. Slevin and T. Ohtsuki, "Critical exponent for the quantum Hall transition", Phys. Rev. B 80.4 (2009) 041304, ISSN: 1098-0121, arXiv: 0905.1163 (cit. on p. 72).

[130] P. W. Anderson, "Absence of Diffusion in Certain Random Lattices", Phys. Rev. 109.5 (1958) 1492, ISSN: 0031-899X, arXiv: 0807.2531 (cit. on p. 72).

[131] J. K. Asbóth, L. Oroszlány and A. Pályi, "A Short Course on Topological Insulators: Band-structure topology and edge states in one and two dimensions", Lecture Notes in Physics 919 (2015), ISSN: 0075-8450, arXiv: 1509.02295 (cit. on p. 89).

Derivation of the Phases of the Magnetic Translation Operators

The phases $\{\mathcal{X}_{j,l}^x, \mathcal{X}_{j,l}^y\}$ of the magnetic translation operators $\{\hat{T}_x, \hat{T}_y\}$ are derived in [54, 55]. However, for completeness of the Chapter 2 I add the derivation here, which is closely followed from [54, 55]. The phases $\{\mathcal{X}_{j,l}^x, \mathcal{X}_{j,l}^y\}$ can be obtained from the requirement that the two MTOs should commute with the Hamiltonian eq. (2.17). Since this Hamiltonian consists of shift operators $\{\hat{S}_x, \hat{S}_y\}$, so the requirement is that the $\{\mathcal{X}_{j,l}^x, \mathcal{X}_{j,l}^y\}$ should commute with the shift operators. This gives us four conditions on the phases of the MTOs, which can be derived using the following steps.

Consider the commutation $[\hat{S}_x, \hat{T}_x]$ and apply this on a single-particle state at a lattice site with coordinates (j, l),

$$
\begin{aligned}
\hat{S}_x \hat{T}_x |j, l\rangle &= \hat{S}_x \left(\sum_{j',l'} e^{i\mathcal{X}_{j',l'}^x} \hat{c}_{j'+1,l'}^\dagger \hat{c}_{j',l'} \right) \hat{c}_{j,l}^\dagger |0\rangle \\
&= \hat{S}_x \, e^{i\mathcal{X}_{j,l}^x} \hat{c}_{j+1,l}^\dagger |0\rangle, \text{ for } j' = j \text{ and } l' = l \\
&= \left(\sum_{j'',l''} e^{i\Theta_{j'',l''}^x} \hat{c}_{j''+1,l''}^\dagger \hat{c}_{j',l''} \right) e^{i\,\mathcal{X}_{j,l}^x} \hat{c}_{j+1,l}^\dagger |0\rangle \\
&= e^{i\left(\Theta_{j+1,l}^x + \mathcal{X}_{j,l}^x\right)} \hat{c}_{j+2,l}^\dagger |0\rangle, \text{ for } j'' = j+1 \text{ and } l'' = l \\
&= e^{i\left(\Theta_{j+1,l}^x + \mathcal{X}_{j,l}^x\right)} |j+2, l\rangle.
\end{aligned}
\tag{A.1}
$$

Similarly

$$
\hat{T}_x \hat{S}_x |j, l\rangle = e^{i\left(\Theta_{j,l}^x + \mathcal{X}_{j+1,l}^x\right)} |j+2, l\rangle.
\tag{A.2}
$$

This gives

$$
[\hat{S}_x, \hat{T}_x]|j, l\rangle = \left(e^{i\left(\Theta_{j+1,l}^x + \mathcal{X}_{j,l}^x\right)} - e^{i\left(\Theta_{j,l}^x + \mathcal{X}_{j+1,l}^x\right)} \right) |j+2, l\rangle.
\tag{A.3}
$$

For $[\hat{S}_x, \hat{T}_x] = 0$, we get the condition,

$$e^{i\left(\Theta^x_{j,l} + X^x_{j+1,l}\right)}\left[e^{i\left(\Theta^x_{j+1,l} + X^x_{j,l} - \Theta^x_{j,l} - X^x_{j+1,l}\right)} - 1\right] = 0$$

$$\Rightarrow \Delta_x \Theta^x_{j,l} = \Delta_x X^x_{j,l}. \tag{A.4}$$

Using the same procedure, we get the following conditions:
For $[\hat{S}_y, \hat{T}_y] = 0$,

$$= e^{i\left(\Theta^y_{j,l} + X^y_{j,l+1}\right)}\left[e^{i\left(\Theta^y_{m,l+1} + X^y_{j,l} - \Theta^y_{j,l} - X^y_{j,l+1}\right)} - 1\right] = 0$$

$$\Rightarrow \Delta_y \Theta^y_{j,l} = \Delta_y X^y_{j,l}. \tag{A.5}$$

For $[\hat{S}_x, \hat{T}_y] = 0$,

$$= e^{i\left(\Theta^x_{j,l} + X^y_{j+1,l}\right)}\left[e^{i\left(\Theta^x_{j,l+1} + X^y_{j,l} - \Theta^x_{j,l} - X^y_{j+1,l}\right)} - 1\right] = 0$$

$$\Rightarrow \Delta_x X^y_{j,l} = \Delta_y \Theta^x_{j,l} = \Delta_x \Theta^y_{j,l} - 2\pi\phi_{j,l}. \tag{A.6}$$

For $[\hat{S}_y, \hat{T}_x] = 0$,

$$= e^{i\left(\Theta^y_{j,l} + X^x_{j,l+1}\right)}\left[e^{i\left(\Theta^y_{j+1,l} + X^x_{j,l} - \Theta^y_{j,l} - X^x_{j,l+1}\right)} - 1\right] = 0$$

$$\Rightarrow \Delta_y X^x_{j,l} = \Delta_x \Theta^y_{j,l} = \Delta_y \Theta^x_{j,l} + 2\pi\phi_{j,l}. \tag{A.7}$$

In the last two conditions, we have made use of the discrete lattice derivatives eq. (2.14). The values of $\{X^x_{j,l}, X^y_{j,l}\}$, for which the MTOs commute with the Hamiltonian eq. (2.17), are obtained by solving the above conditions. For this, the flux ratio can be written as,

$$\phi_{j,l} = (j + 1)\phi_{j,l} - j\phi_{j,l}$$
$$= \Delta_x(j\phi_{j,l}). \tag{A.8}$$

Putting this in eq. (A.6), we get the $X^y_{j,l}$. Similarly, we can write the flux ratio as,

$$\phi_{j,l} = (l + 1)\phi_{j,l} - l\phi_{j,l}$$
$$= \Delta_y(l\phi_{j,l}). \tag{A.9}$$

By putting thise into eq. (A.7), we get $X^x_{j,l}$. The resulting solutions are given in eq. (2.20).

Fourier Transformation of the Harper Equation

On the spatially regrouped lattice (introduce in sec. 2.2), we use the following Fourier transformation,

$$\hat{c}_{jq+j',l} = \frac{q}{2\pi} \frac{1}{2\pi} \int_{-\pi/q,-\pi}^{+\pi/q,+\pi} dk_x \, dk_y \, \hat{c}_{k_x,ky,j'} \, e^{i(jq+j')k_x} \, e^{ik_y l}, \tag{B.1}$$

with the inverse transformation

$$\hat{c}_{k_x,ky,j'} = \sum_{j,j',l} e^{-i(jq+j')k_x} \, e^{-ik_y l} \hat{c}_{jq+j',l}. \tag{B.2}$$

By putting the transformation eq. (B.1) in the Hamiltonian eq. (2.30), the first two terms can be written as

$$\sum_{j,j',l} \hat{c}^{\dagger}_{jq+j'+1,l} \hat{c}_{jq+j',l} \;\;\rightarrow\;\; \frac{q}{(2\pi)^2} \int_{-\pi/q,-\pi}^{+\pi/q,+\pi} dk_x \, dk_y \otimes \left(\sum_{j'} e^{-ik_x} \, \hat{c}^{\dagger}_{k_x,ky,j'+1} \, \hat{c}_{k_x,ky,j'} \right),$$

$$\sum_{j,j',l} e^{i2\pi\phi(jq+j')} \, \hat{c}^{\dagger}_{jq+j',l+1} \hat{c}_{jq+j',l} \;\;\rightarrow\;\; \frac{q}{(2\pi)^2} \int_{-\pi/q,-\pi}^{+\pi/q,+\pi} dk_x \, dk_y \otimes \left(\sum_{j'} e^{i(2\pi\phi j'-k_y)} \, \hat{c}^{\dagger}_{k_x,ky,j'} \, \hat{c}_{k_x,ky,j'} \right). \tag{B.3}$$

The Hermitian conjugate of these two terms are,

$$\sum_{j,j',l} \hat{c}^{\dagger}_{jq+j'-1,l} \hat{c}_{jq+j',l} \;\;\rightarrow\;\; \frac{q}{(2\pi)^2} \int_{-\pi/q,-\pi}^{+\pi/q,+\pi} dk_x \, dk_y \otimes \left(\sum_{j'} e^{ik_x} \, \hat{c}^{\dagger}_{k_x,ky,j'-1} \, \hat{c}_{k_x,ky,j'} \right),$$

$$\sum_{j,j',l} e^{-i2\pi\phi(jq+j')} \, \hat{c}^{\dagger}_{jq+j',l-1} \hat{c}_{jq+j',l} \;\;\rightarrow\;\; \frac{q}{(2\pi)^2} \int_{-\pi/q,-\pi}^{+\pi/q,+\pi} dk_x \, dk_y \otimes \left(\sum_{j'} e^{-i(2\pi\phi j'-k_y)} \, \hat{c}^{\dagger}_{k_x,ky,j'} \, \hat{c}_{k_x,ky,j'} \right). \tag{B.4}$$

Adding these four terms, we obtain the Hamiltonian eq. (2.31).

APPENDIX **C**

Computing the Chern Numbers of the Magnetic Bloch Bands

Chern numbers are generally defined for quantum states parametrized by two periodic parameters. The magnetic Bloch states, introduced in sec. 2.1.1, are parametrized by quasimomentum k_x and k_y. Hence, we can compute Chern numbers for the corresponding energy bands. Due to the periodicity of the magnetic Bloch states in both k_x and k_y direction, the topology of the BZ is similar to a torus and the Chern numbers do have a physical significance [131]. In continuum, the Chern number of a jth isolated band corresponding to a normalized magnetic Bloch state $|u_j(k)\rangle$ is defined as

$$C_j = -\frac{1}{2\pi} \int_{\text{MBZ}} dk_x dk_y \Big(\frac{\partial A_y^{(j)}}{\partial k_x} - \frac{\partial A_x^{(j)}}{\partial k_y}\Big), \tag{C.1}$$

where A^j is known as the Berry connection of the jth band and the integrand is known as the Berry curvature. Explicitly, the Berry connection of the jth band is defined as

$$A_\mu^{(j)}(k) = i \langle u_j(k)| \frac{\partial}{\partial k_\mu} |u_j(k)\rangle, \quad \text{for } \mu = (x, y). \tag{C.2}$$

The normalized magnetic Bloch states $|u_j(k)\rangle$, with j representing the band index, are obtained by solving the Schrödinger equation 2.32. For numerical computation of the Chern number of a band, one can use the discrete version of the formulas (C.1), (C.2). These, in general, deal with gauge-dependent quantities and must be taken care of (by fixing the gauge of the wavefunctions). This procedure for computing Chern numbers is relatively difficult. I use an alternative method presented by Fukui et al. [59], which does not need gauge fixation of the wavefunctions and Chern numbers can be computed with any arbitrary gauge. I used this method for computing the Chern numbers of the magnetic Bloch bands shown in fig. 2.5.

For simplicity, let us consider a single band that is isolated from other bands by energy gaps with corresponding eigenfunction $u(k)$. The idea is to discretize the MBZ by considering a squared grid and compute $u(k)$ on the restricted data points. Consider a 2D MBZ with $-\pi/q_1 \le k_x < \pi/q_1$ and $-\pi/q_2 \le k_y < \pi/q_2$ with q_1 and q_2 are positive non-zero integers. Divide the MBZ into small square

Figure C.1: Schematic of the discretized MBZ which is 3-times smaller along the k_x direction for $q_1 = 1/3$ and $q_2 = 1$. This asymmetry of the MBZ is due to our choice of the Landau gauge. We have considered $N_0 = 3$ which gives $N_1 = q_2 N_0 = 3$ (number of plaquettes along k_x) and $N_2 = q_1 N_0 = 9$ (number of plaquettes along k_y) direction. The links variables for the first plaquette (shaded) of the lattice is shown from which the corresponding lattice field strength $\tilde{F}_{12}(-\pi/3, -\pi)$ can be obtained using eq. (C.4). The Chern number of a band is obtained by adding the lattice field strength of all the plaquettes.

plaquettes as shown in fig. C.1. The coordinates of each point k_i in the discretized BZ are

$$k_i = (k_x, k_y), \quad i = 1, 2, \ldots, N_1 N_2$$

$$k_x = -\frac{\pi}{q_1} + \frac{2\pi i_1}{q_1 N_1}, \quad i_1 = (0, 1, \ldots, N_1 - 1)$$

$$k_y = -\frac{\pi}{q_2} + \frac{2\pi i_2}{q_2 N_2}, \quad i_2 = (0, 1, \ldots, N_2 - 1). \tag{C.3}$$

By choosing $N_1 = q_2 N_0$ and $N_2 = q_1 N_0$, each plaquette is a square with edge length $\frac{2\pi}{q_1 q_2 N_0}$ in both directions. The Hamiltonian is diagonalized at these points of the BZ to obtain $u(k_i)$. From these discrete states, a lattice field strength (a quantity analogous to Berry curvature or Berry flux) is defined for each plaquette in the following way:

$$\tilde{F}_{12}(k_i) \equiv \ln U_1(k_i) U_2(k_i + \hat{e}_1) U_1(k_i + \hat{e}_2)^{-1} U_2(k_i)^{-1}, \tag{C.4}$$

with $\hat{e}_1 = \frac{2\pi}{q_1 q_2 N_0}(1, 0)$ and $\hat{e}_2 = \frac{2\pi}{q_1 q_2 N_0}(0, 1)$ are vectors in quasimomentum space in the k_x and the k_y

direction. The $U(1)$ link variables $U_{1,2}$ for the eigenfunctions $u(k_i)$ is defined as

$$U_{1,2}(k_i) = \frac{\langle u(k_i)|u(k_i + \hat{e}_{1,2})\rangle}{|\langle u(k_i)|u(k_i + \hat{e}_{1,2})\rangle|}. \tag{C.5}$$

From the definition of the lattice field strength eq. (C.4), it is clear that it is a gauge independent quantity and can take values within the principle branch of logarithm, i.e. $-\pi < \frac{1}{i}\tilde{F}_{12} \leq \pi$. The Chern number of the band is then obtained by adding the lattice field strength of all the plaquettes, i.e.

$$C = \frac{1}{2\pi i} \sum_i \tilde{F}_{12}(k_i). \tag{C.6}$$

The Chern number computed through this procedure does not require gauge specification and has been shown to reproduce correct values even for coarsely discretized BZ [59].

This method can be extended to the non-abelian Berry connection for computing the Chern number of the bands which are touching each other. For the magnet Bloch bands (fig. 2.5(b)), the two innermost bands are touching and hence I use the extension of the above method to compute their Chern number. In general, for j touching bands separated by gaps from other bands, the modified non-abelian Berry connection is a $j \times j$ matrix associated with the multiplet $(u_1(k_i), u_2(k_i), \ldots, u_j(k_i))$, and has the following form

$$\tilde{A}_{1,2}(k_i) = \begin{pmatrix} \langle u_1(k_i)|u_1(k_i + \hat{e}_{1,2})\rangle & \langle u_1(k_i)|u_2(k_i + \hat{e}_{1,2})\rangle & \cdots & \langle u_1(k_i)|u_j(k_i + \hat{e}_{1,2})\rangle \\ \langle u_2(k_i)|u_1(k_i + \hat{e}_{1,2})\rangle & \langle u_2(k_i)|u_2(k_i + \hat{e}_{1,2})\rangle & \cdots & \langle u_2(k_i)|u_j(k_i + \hat{e}_{1,2})\rangle \\ \vdots & \vdots & \ddots & \vdots \\ \langle u_{j-1}(k_i)|u_1(k_i + \hat{e}_{1,2})\rangle & \langle u_{j-1}(k_i)|u_2(k_i + \hat{e}_{1,2})\rangle & \cdots & \langle u_{j-1}(k_i)|u_j(k_i + \hat{e}_{1,2})\rangle \\ \langle u_j(k_i)|u_1(k_i + \hat{e}_{1,2})\rangle & \langle u_j(k_i)|u_2(k_i + \hat{e}_{1,2})\rangle & \cdots & \langle u_j(k_i)|u_j(k_i + \hat{e}_{1,2})\rangle \end{pmatrix}. \tag{C.7}$$

The corresponding link variable is then obtained by taking the determinant of $\tilde{A}_{1,2}(k_i)$, i.e.

$$\tilde{U}_{1,2}(k_i) = \frac{\det \tilde{A}_{1,2}(k_i)}{|\det \tilde{A}_{1,2}(k_i)|}. \tag{C.8}$$

The corresponding field strength and the Chern number of the bands is obtained using the definitions given in equations (C.4)-(C.6). For the example shown in fig. 2.5(b), the modified non-abelian Berry connection is a 2×2 matrix (for the two touching bands) and the Chern number is computed using the above procedure. The resultant value of the Chern number is an integer similar to that in the abelian case (fig. 2.5).

Particle–Hole Symmetry of the Harper Hamiltonian

I briefly discuss the PHS of the Harper Hamiltonian, as a result of which the Chern number of a magnetic Bloch band with energy E is equal to the one with energy $-E$. This symmetric distribution of the Chern numbers is exemplified in Chapter 2. For details on other symmetry properties of the Harper Hamiltonian, we refer the readers to the paper by X. G. Wen and A. Zee [56].

Due to the presence of PHS, the energy values of the Harper Hamiltonian come in pairs, i.e. for each state $\psi_{j,l}$ with an energy E there exist a state $\psi'_{j,l} = (-1)^{j+l}\psi_{j,l}$ with an energy $-E$. The two states are then called particle-hole symmetric partners. I show the existence of this symmetry by closely following [55]. By putting the ansatz for the wavefunction

$$\psi_{j,l} = e^{-ijk_x}\, e^{-ilk_y} a_j\, |j\rangle \tag{D.1}$$

in the Schrödinger equation

$$\hat{H}\psi_{j,l} = E\psi_{j,l}, \tag{D.2}$$

with the Hamiltonian $\hat{H}$ given in eq. (2.27). This gives,

$$E\psi_{j,l} = -\mathcal{J}(\psi_{j+1,l} + \psi_{j-1,l} + e^{i2\pi\phi j}\psi_{j,l+1} + e^{-i2\pi\phi j}\psi_{j,l-1}). \tag{D.3}$$

Now putting $\psi'_{j,l} = (-1)^{j+l}\psi_{j,l}$ in the Schrödinger equation D.2, we have

$$-E\psi'_{j,l} = -\mathcal{J}(\psi'_{j+1,l} + \psi'_{j-1,l} + e^{i2\pi\phi j}\psi'_{j,l+1} + e^{-i2\pi\phi j}\psi'_{j,l-1}). \tag{D.4}$$

This shows that the wave function $\psi'_{j,l}$ is also a solution of the Schrödinger equation but with energy $-E$. This confirms the fact that for each eigenstate $\psi_{j,l}$ with an energy E of the Harper Hamiltonian, there exists a state $\psi'_{j,l}$ with an energy $-E$. By making use of the generalized Bloch periodicity of the wavefunction eq. (D.1), i.e. $\psi_{j+q,l} = e^{-iqk_x}\psi_{j,l}$ and $\psi_{j,l+1} = e^{-ik_y}\psi_{j,l}$, eq. (D.3) reduced to the eigenvalue equation

$$E_{k_x,k_y}\, a_j = -\mathcal{J}(e^{-ik_x}\, a_{j-1} + e^{ik_x}\, a_{j+1} + 2\cos(2\pi\phi j - k_y)\, a_j), \tag{D.5}$$

which is same as eq. (2.34). Similarly eq. (D.4) reduced to the eigenvalue equation

$$-E_{k_x,k_y}\, a'_j = -\mathcal{J}(e^{-ik_x}\, a'_{j-1} + e^{ik_x}\, a'_{j+1} + 2\cos(2\pi\phi j - k_y)\, a'_j), \tag{D.6}$$

which is again same as eq. (2.34) but with $E \rightarrow -E$. This can also be written as

$$E_{k_x,k_y} \, a'_j = -\mathcal{J}(e^{-i(k_x+\pi)} \, a'_{j-1} + e^{i(k_x+\pi)} \, a'_{j+1} + 2\cos(2\pi\phi j - (k_y + \pi)) \, a'_j), \tag{D.7}$$

which by comparing with eq. (D.5) shows the fact that an eigenstate associated with a magnetic Bloch band of positive energy is related to the one with negative energy by the relation

$$a_j(k_x, k_y) = a'_j(k_x + \pi, k_y + \pi). \tag{D.8}$$

PHS transforms a state with an energy E to a state with an energy $-E$ and in addition results in a shift in the quasimomentum space, i.e. $(k_x, k_y) \rightarrow (k_x + \pi, k_y + \pi)$. As a result, the energy dispersion of a band with positive energy $E^+_{k_x,k_y}$ is related to the dispersion of a band with negative energy $E^-_{k_x,k_y}$

$$E^+_{k_x,k_y} = -E^-_{k_x+\pi,k_y+\pi}. \tag{D.9}$$

Due to the relationship between two particle-hole symmetric partners states (eq. (D.8)), the Chern numbers of the corresponding two magnetic Bloch bands have that same integer values.

APPENDIX **E**

Chiral Symmetry of the Magnetic Quantum Walk Protocol

There are conical band touching points for the 2D QWs (see fig. 4.2 (left)). In the case without magnetic field, there are four such band touching points, at

$$K_{\pm,\mp} = \left(k_x = \pm\frac{\pi}{2}, k_y = \mp\frac{\pi}{2}\right), \quad \varepsilon = 0; \tag{E.1}$$

$$K_{\pm,\pm} = \left(k_x = \pm\frac{\pi}{2}, k_y = \pm\frac{\pi}{2}\right), \quad \varepsilon = \pi. \tag{E.2}$$

We now show that these band touching points are topologically protected Weyl points, due to CS – similar to the Dirac points of graphene.

Chiral Symmetry in Periodically Driven Systems

CS is a unitary TRS. In a periodically driven system with time step operator $\hat{W}$, a CS is represented by $\hat{\Gamma}$, if

$$\hat{\Gamma}\hat{W}\hat{\Gamma} = \hat{W}^\dagger; \quad \hat{\Gamma}^\dagger = \hat{\Gamma}^{-1} = \hat{\Gamma}. \tag{E.3}$$

A consequence of the CS of the timestep operator is the CS of its effective Hamiltonian $\hat{H}_{\text{eff.}}$, defined by the relation $\hat{W} = e^{-i\hat{H}_{\text{eff.}}}$. If the timestep operator $\hat{W}$ is chiral symmetric, we have

$$\hat{\Gamma}\hat{H}_{\text{eff.}}\hat{\Gamma} = -\hat{H}_{\text{eff.}}. \tag{E.4}$$

In the chiral basis, i.e. in the basis where $\hat{\Gamma}$ is diagonal, i.e. $\hat{\Gamma} = 1 \oplus (-1)$, the bulk effective Hamiltonian is off-diagonal,

$$\hat{\Gamma} = \begin{pmatrix} 1 & 0 \\ 0 & -1 \end{pmatrix}; \quad \hat{H}_{\text{eff}}(k) = \begin{pmatrix} 0 & h(k) \\ h(k)^\dagger & 0 \end{pmatrix}. \tag{E.5}$$

If the Hamiltonian has a bulk gap around zero energy, and it lives in odd dimensions, this brings with itself a bulk topological invariant, a winding number. In the 1D case, this can be written as,

$$\nu[h] = \frac{1}{2\pi i} \int_{-\pi}^{\pi} dk \frac{d}{dk} \ln \det h(k), \tag{E.6}$$

where we defined the real-valued functional ν, the winding number of a periodic matrix-valued function.

Chiral Symmetric Timeframe

The 2D QW we consider is chiral symmetric. To show that, I write the time step operator in a chiral symmetric timeframe. As a first step, I break down the shift operators and the magnetic field operator to two separate steps, operating on the spin-up part of the wavefunction first, and the spin-down second. For the shift operators, this reads,

$$\hat{S}_d = \hat{S}_{d,\downarrow}\hat{S}_{d,\uparrow}; \tag{E.7}$$

$$\hat{S}_{d,\uparrow} = \sum_{\boldsymbol{x}} |\boldsymbol{x} + \mathbf{e}_d\rangle \langle \boldsymbol{x}| \otimes |\uparrow\rangle \langle\uparrow| + |\boldsymbol{x}\rangle \langle \boldsymbol{x}| \otimes |\downarrow\rangle \langle\downarrow|; \tag{E.8}$$

$$\hat{S}_{d,\downarrow} = \hat{\sigma}_x(\hat{S}_{d,\uparrow})^{\dagger}\hat{\sigma}_x. \tag{E.9}$$

For the magnetic field operator, this is done by,

$$\hat{F} = \hat{F}_{\downarrow}\hat{F}_{\uparrow}; \tag{E.10}$$

$$\hat{F}_{\uparrow} = \sum_{\boldsymbol{x}} e^{iB\boldsymbol{x}} |\boldsymbol{x}\rangle \langle \boldsymbol{x}| \otimes |\uparrow\rangle \langle\uparrow| + |\boldsymbol{x}\rangle \langle \boldsymbol{x}| \otimes |\downarrow\rangle \langle\downarrow|; \tag{E.11}$$

$$\hat{F}_{\downarrow} = \hat{\sigma}_x\hat{F}_{\uparrow}^{\dagger}\hat{\sigma}_x. \tag{E.12}$$

I have Used the notation $\boldsymbol{x} = (x,y) \in \mathbb{Z}^2$, $d \in \{x,y\}$ and $\mathbf{e}_d$ is d-direction unit lattice vector. It is the spin-flip operator $\hat{\sigma}_x$ that will represent CS of the 2D QW. To show this, we need to write the timestep operator in a chiral symmetric timeframe.

$$\hat{W}' = \hat{F}_{\uparrow}\hat{S}_{y,\uparrow}\hat{C}\hat{S}_{x,\uparrow}\hat{S}_{x,\downarrow}\hat{C}\hat{S}_{y,\downarrow}\hat{F}_{\downarrow} \tag{E.13}$$

In case there is no magnetic field, the bulk timestep operator reads,

$$\hat{W}'(k_x, k_y) = \frac{1}{2}\begin{pmatrix} e^{-ik_x-ik_y} - e^{ik_x-ik_y} & -e^{-ik_x} - e^{ik_x} \\ e^{-ik_x} + e^{ik_x} & -e^{-ik_x+ik_y} + e^{ik_x+ik_y} \end{pmatrix}. \tag{E.14}$$

Expanding this to first order around the gap closing points, using $\mathsf{q} = k - K$, we find:

$$K_{\pm,\pm} : \hat{W}'(\mathsf{q}_x, \mathsf{q}_y) \approx -1 + i(\pm\mathsf{q}_x\hat{\sigma}_y + \mathsf{q}_y\hat{\sigma}_z) \tag{E.15}$$

$$K_{\pm,\mp} : \hat{W}'(\mathsf{q}_x, \mathsf{q}_y) \approx 1 + i(\pm\mathsf{q}_x\hat{\sigma}_y - \mathsf{q}_y\hat{\sigma}_z). \tag{E.16}$$

Topological Charges of the Nodes

The nodes are topologically protected. To put this in formulas, we can evaluate the winding number around each node. To rewrite the effective Hamiltonian in the chiral basis, we need to do a unitary transformation which takes $\hat{\sigma}_x \rightarrow \hat{\sigma}_z$. A suitable transformation uses $(1 + i\hat{\sigma}_y)/\sqrt{2}$, and takes $\hat{\sigma}_x \rightarrow \hat{\sigma}_z$, $\hat{\sigma}_y \rightarrow \hat{\sigma}_y$ and $\hat{\sigma}_z \rightarrow -\hat{\sigma}_x$. Thus, in the chiral basis, the effective Hamiltonian, linearized around the

nodes, reads

$$K_{\pm,\pm} : \hat{H}_{\text{eff.}}(\mathsf{q}_x, \mathsf{q}_y) \approx \begin{pmatrix} -\pi & -\mathsf{q}_y \mp i\mathsf{q}_x \\ -\mathsf{q}_y \pm i\mathsf{q}_x & -\pi \end{pmatrix}; \tag{E.17}$$

$$K_{\pm,\mp} : \hat{H}_{\text{eff.}}(\mathsf{q}_x, \mathsf{q}_y) \approx \begin{pmatrix} 0 & -\mathsf{q}_y \pm i\mathsf{q}_x \\ -\mathsf{q}_y \mp i\mathsf{q}_x & 0 \end{pmatrix}. \tag{E.18}$$

We can evaluate the winding number using a circle of infinitesimal radius q around the nodes. We just need to rewrite the top right off-diagonal element h of the Hamiltonian around the nodes,

$$\mathsf{q}_x = \mathsf{q}\cos(\varphi); \quad \mathsf{q}_y = \mathsf{q}\sin(\varphi); \tag{E.19}$$

$$K_{\pm,\pm} : h = \mp i\mathsf{q}e^{\mp i\varphi}; \implies \nu = \mp 1, \tag{E.20}$$

$$K_{\pm,\mp} : h = \pm i\mathsf{q}e^{\pm i\varphi}; \implies \nu = \pm 1. \tag{E.21}$$

Thus all of these nodes carry a topological charge, a winding number of the Hamiltonian around the node. The charges of the nodes at the same quasienergy are apposite.

Half-Timestep Operator

A sufficient but not necessary requirement for CS is

$$\hat{W} = \hat{\Gamma}\hat{\mathcal{F}}^\dagger\hat{\Gamma}\hat{\mathcal{F}}. \tag{E.22}$$

If that holds, we have two chiral symmetric timeframes, and not one but two topological invariants. This is a special feature of periodically driven systems, and is connected to the fact that there are two chiral symmetric quasienergies, i.e. $\varepsilon = 0$ and $\varepsilon = \pi$. The corresponding topological invariants can be obtained directly from the blocks of the operator $\hat{\mathcal{F}}(k)$ in the chiral basis,

$$\hat{\Gamma} = \begin{pmatrix} 1 & 0 \\ 0 & -1 \end{pmatrix}; \quad \hat{\mathcal{F}}(k) = \begin{pmatrix} a(k) & b(k) \\ c(k) & d(k) \end{pmatrix}; \tag{E.23}$$

$$\nu_0 = \nu[b]; \quad \nu_\pi = \nu[d]. \tag{E.24}$$

The spin-flip operator $\hat{\sigma}_x$ represents the CS of the walk here. To show this, we need to write the time step operator in a chiral symmetric time frame,

$$\hat{W}' = \hat{\sigma}_x\hat{\mathcal{F}}^\dagger\hat{\sigma}_x\hat{\mathcal{F}}; \tag{E.25}$$

$$\hat{\mathcal{F}} = \hat{S}_{x,\downarrow}\hat{C}\hat{S}_{y,\downarrow}\hat{F}_\downarrow. \tag{E.26}$$

In the bulk, the matrix of the half-timestep operator $\hat{\mathcal{F}}$, when there is no magnetic field, is

$$\begin{aligned}\hat{\mathcal{F}}(k_x, k_y) &= \frac{1}{\sqrt{2}} \begin{pmatrix} 1 & 0 \\ 0 & e^{ik_x} \end{pmatrix} \begin{pmatrix} 1 & -1 \\ 1 & 1 \end{pmatrix} \begin{pmatrix} 1 & 0 \\ 0 & e^{ik_y} \end{pmatrix} \\ &= \frac{1}{\sqrt{2}} \begin{pmatrix} 1 & -e^{ik_y} \\ e^{ik_x} & e^{ik_x+ik_y} \end{pmatrix}. \end{aligned} \tag{E.27}$$

This is written in the spinor basis, where $|\uparrow\rangle = (1,0)^T$ and $|\downarrow\rangle = (0,1)^T$, i.e. the eigenbasis of $\hat{\sigma}_z$. We need to unitary transform it into a basis where the CS operator $\hat{\sigma}_x$ is diagonal. This basis transformation is

obtained by $(1 + i\hat{\sigma}_y)/\sqrt{2}$, and we obtain

$$
\hat{\mathcal{F}}(k_x, k_y) = \begin{pmatrix} a(k) & b(k) \\ c(k) & d(k) \end{pmatrix}
$$
$$
= \frac{1}{2\sqrt{2}} \begin{pmatrix} 1 & 1 \\ -1 & 1 \end{pmatrix} \begin{pmatrix} 1 & -e^{ik_y} \\ e^{ik_x} & e^{ik_x+ik_y} \end{pmatrix} \begin{pmatrix} 1 & -1 \\ 1 & 1 \end{pmatrix}; \tag{E.28}
$$

with

$$
a(k) = \left(1 + e^{ik_x} - e^{ik_y} + e^{ik_x+ik_y}\right)/(2\sqrt{2}); \tag{E.29}
$$

$$
b(k) = \left(-1 - e^{ik_x} - e^{ik_y} + e^{ik_x+ik_y}\right)/(2\sqrt{2}); \tag{E.30}
$$

$$
c(k) = \left(-1 + e^{ik_x} + e^{ik_y} + e^{ik_x+ik_y}\right)/(2\sqrt{2}); \tag{E.31}
$$

$$
d(k) = \left(1 - e^{ik_x} + e^{ik_y} + e^{ik_x+ik_y}\right)/(2\sqrt{2}). \tag{E.32}
$$

Weak Topological Invariants

This is a bulk 2D Hamiltonian, with CS. Along the lines of constant k_y or k_x we can define winding numbers, the weak topological invariants. For example, at a fixed k_y, we can define the winding number controlling the 0-quasienergy behaviour as

$$
\nu_{0,x}(k_y) = \nu[b]\big|_{k_y} = \frac{1}{2\pi i} \int_{-\pi}^{\pi} dk_x \frac{d}{dk_x} \ln b(k_x, k_y). \tag{E.33}
$$

We can find the topological invariants using a graphic solution. For example, to obtain $\nu_{0,x}(k_y)$, I plot the curve of $b(k_x, k_y)$ on the complex plain, at a fixed k_y, as a function of k_x. This is a circle of radius $\left|1 - e^{ik_y}\right|$ around the point $-1 - e^{ik_y}$. The winding number will thus be 1 if the radius of the circle is larger than the distance of its center from the origin, and 0 otherwise. Thus, the winding number is 1 if $\left|1 - e^{ik_y}\right| > \left|-1 - e^{ik_y}\right|$, equivalently, if $\left|\sin(k_y/2)\right| > \left|\cos(k_y/2)\right|$, which gives

$$
\nu_{0,x}(k_y) = 1 \quad \text{if } |k_y| > \pi/2, \quad \text{and 0 otherwise.} \tag{E.34}
$$

In a similar way, I obtain the other winding numbers:

$$
\nu_{\pi,x}(k_y) = 1 \quad \text{if } |k_y| > \pi/2, \quad \text{and 0 otherwise.} \tag{E.35}
$$

$$
\nu_{0,y}(k_x) = 1 \quad \text{if } |k_x| > \pi/2, \quad \text{and 0 otherwise.} \tag{E.36}
$$

$$
\nu_{\pi,y}(k_x) = 0 \quad \text{if } |k_x| > \pi/2, \quad \text{and 1 otherwise.} \tag{E.37}
$$

Thus at the gap closing points the winding numbers indeed change.

In the presence of a magnetic field, the elements of the half time step operators $\hat{\mathcal{F}}(k_x, k_y)$ are square matrices whose dimensionality depend on the the strength of the magnetic field. I have numerically confirmed, for the case $\phi = 1/3$, that CS symmetry exists and the weak topological invariants can be obtained by putting the determinants of the matrix $b(k)$ and $d(k)$ instead of $b(k)$ and $d(k)$ in eq. (E.33).

Computing Topological Invariants of the Magnetic Quantum Walks from the Spectral Flow

In this appendix, we show how to calculate the topological invariant v as the spectral flow induced by an extra magnetic field. For the purpose of the calculation, I modify the unitary walk operator with an extra pseudo-magnetic field. Importantly, the vector potential corresponding to this extra magnetic field does not vary inside the unit cells. The corresponding unitary operator $F_{\text{extra}}[\beta]$ is defined by

$$F_{\text{extra}}[\beta] = e^{-i\sigma_z\beta\lfloor x/q \rfloor}, \tag{F.1}$$

where $\lfloor x/q \rfloor$ is the greatest integer smaller than or equal to x/q. We take $\beta = m/M$, with m and M relative prime integers. In fact, only $\beta = 0$ and $\beta = 1/M$ are needed. Thus, the unit cell of the system has to be enlarged: it has size 1 along y, but width Mq along x. The full magnetic field operator reads

$$F_1[\beta = m/M, B] = e^{i\sigma_z\{\beta\lfloor x/q \rfloor + B(x \bmod q)\}}. \tag{F.2}$$

Finally, I push the quasienergy gap of interest (for which I want to compute the topological invariant) in to the BZ boundary, by multiplying the unitary walk operator by a factor $e^{i\varepsilon}$. Thus, the modified QW operator reads,

$$W_1[\beta, B, \varepsilon] = e^{i\varepsilon}F_1[\beta, B]e^{-i\sigma_z k_y}e^{-i\sigma_y\pi/4}S_x e^{-i\sigma_y\pi/4}, \tag{F.3}$$

with twisted boundary conditions along x with phase k_x. The eigenvalues of this operator are denoted by $e^{-i\varepsilon_j[\beta, B, \varepsilon]}$, with $j = 1 \ldots, 2Mq$. The formula for the topological invariant of the gap reads,

$$v_\varepsilon[B] = \frac{1}{2\pi}\left(\sum_{j=1}^{2Mq}\varepsilon_j[1/M, B, \varepsilon] - \sum_{j=1}^{2Mq}\varepsilon_j[0, B, \varepsilon]\right). \tag{F.4}$$

The numerically obtained values of the invariants are shown in fig. F.1. The DOS (normalized to the total number of states) is also shown, which indicates the positions of the bulk gaps. The invariants of the gaps are calculated for a single value of k_x and k_y; however, we have checked that their values do not depend on quasimomentum. The computed values agree with the number of edge states shown in fig. 4.5 (b).

Figure F.1: Spectral flow *ν* calculated using an extra magnetic field. *M* = 10, with DOS overlaid (colored shading) to give an impression of where the bulk bands are. In the band gaps, the spectral flow reproduces the topological invariants (thick black lines).

Acknowledgements

Eidesstattliche Erklärung

Diese Dissertation wurde im Sinne der Promotionsordnung vom 17.06.2011 am Institut für Angewandte Physik der Universität Bonn unter der Leitung von Prof. Dr. Dieter Meschede angefertig. Hiermit versichere ich, dass ich die vorgelegte Arbeit selbständig verfasst und keine anderen als die angegebenen Quellen und Hilfsmittel benutzt sowie die Zitate kenntlich gemacht habe.

_____
Ort, Datum

_____
Muhammad Sajid